5-24-2009

Engineering the Optical Properties of Gold Nanostructures for Biomedical Applications

Leslie Au
Washington University in St. Louis

Recommended Citation

Au, Leslie, "Engineering the Optical Properties of Gold Nanostructures for Biomedical Applications" (2009). *All Theses and Dissertations (ETDs)*. 881.
https://openscholarship.wustl.edu/etd/881

WASHINGTON UNIVERSITY

School of Engineering
Department of Biomedical Engineering

Dissertation Examination Committee:
Younan Xia, Chair
Carolyn Anderson
Donald Elbert
Richard Loomis
Jin-Yu Shao
Lihong Wang

ENGINEERING THE OPTICAL PROPERTIES OF GOLD NANOSTRUCTURES FOR BIOMEDICAL APPLICATIONS

By

Leslie Pui San Au

A dissertation presented to the
Graduate School of Arts and Sciences
of Washington University in
partial fulfillment of the
requirements for the degree
of Doctor of Philosophy

August 2009

Saint Louis, Missouri

ABSTRACT OF THE DISSERTATION

Engineering the Optical Properties of Gold Nanostructures for Biomedical Applications

by

Leslie P. Au

Doctor of Philosophy in Biomedical Engineering

Washington University in St. Louis, 2009

Professor Younan Xia, Chairperson

This research investigated the synthesis and optical properties of Au nanostructures with an aim to use them as imaging agents and photothermal transducers for the diagnosis and treatment of cancer. I have produced Au nanocages with hollow interiors and porous walls using the galvanic replacement reaction between Ag nanocubes and $AuCl_4^-$. I have engineered these Au nanocages to have localized surface plasmon resonance (LSPR) peaks in the near-infrared region with strong absorption. These optical properties allow for the imaging of biological tissues at deeper penetration and the photoablation of cancer. By replacing $AuCl_4^-$ with $AuCl_2^-$, Au nanoframes were developed. With a series of discrete dipole approximation calculations (DDA), I illustrated how the edge length and ridge thickness of the nanoframe can affect the LSPR peak. I validated the calculated predictions by experimental measurements.

I functionalized the surface of the Au nanocages with antibodies *via* Au-thiolate chemistry to target cancerous cells. The photoluminescence from Au nanocages provided a simple and convenient way to evaluate their *in vitro* targeting capability using two-

photon microscopy. This mode of imaging can be used to quickly screen the interaction between Au nanocages and cells, as well as evaluate the distribution of Au nanocages in tissue for *ex vivo* and *in vivo* studies. I also quantified the photothermal effect of the Au nanocages targeted to cancer cells using flow cytometry coupled with propidium iodide staining.

In addition to Au nanocages and nanoframes, I have synthesized Au microplates using a biological macromolecule, bovine serum albumin (BSA), as the reducing agent. I exposed the reductive hydroxyl groups in the protein by unfolding the structure at an elevated temperature, under an acidic condition, and in the presence of ions.

ACKNOWLEDGEMENTS

I would like to express my most sincere gratitude and appreciation to my advisor Professor Younan Xia for his guidance and patience. His enthusiasm and perseverance is truly inspirational, for which much of my accomplishments and achievements could not have been completed without. I would like to thank Dr. Jingyi Chen, who taught me my first galvanic replacement reaction. She provided insightful conversations and kept me on track. I would also like to thank Dr. Dong Qin for her encouragement and advice.

This dissertation was highly interdisciplinary and truly a group effort. I am greatly thankful to the following people: Dr. Desheng Zheng, a postdoc of Professor Xingde Li, who operated the laser for the photothermal studies on Chinese New Year and many other late nights and early mornings; Dr. Yeechi Chen, a former graduate student of Professor David S. Ginger, who recorded the spectra of single nanoframes; Fei Zhou, a graduate student of Professor Zhi-Yuan Li, who calculated the absorption and scattering spectra of nanoframes; Peter Colletti, a graduate student of Professor Young-Shin Jun, who took AFM images of the microplates; Pedro Camargo for his research collaboration and his friendship throughout these past four years; Qiang Zhang, Annie Schwartz, and Michael Gidding (team QALM) for three solid months of scaling up the production of Au nanocages; Dr. Xianmao Lu and Dr. Sara Skrabalak for being wonderful mentors. Dr. Eric Formo for his friendship and stimulating conversations; and Claire Cobley for her willing help when I relocated to St. Louis.

I would also like to thank all the past and present members of the Xia group: Dr. Eric Lee, Andy Siekkinen, Matt Rycenga, Akira Ohnuma, Maureen McKiernan, Weiyang Li, Xiaoran Li, Yunqian Dai, Yanyun Ma, Majiong Jiang, Dr. Benjamin Wiley, Dr. Eun Chul Cho, Dr. Jie Zeng, Dr. Yiyun Cheng, Dr. Yujie Xiong, Dr. Byungkwon Lim, Dr. Joseph McLellan, Dr. Jesse McCann, and Dr. Alex Briseno.

I am also grateful for the financial support from a NIH Director's Pioneer Award (DP1 OD000798 to Y.X.) and the Center of Nanotechnology at the University of Washington for an IGERT fellowship funded by the NSF and NCI.

DEDICATION

To my parents,

Harry Koon Mun and Christine Ho Yan Au,

my grandfather,

Yong Tang Li,

and

my brothers and sister,

Randy, Raymond, and Laurie Au,

for their love and support.

TABLE OF CONTENTS

Page

LIST OF FIGURES

LIST OF TABLES

Table Number Page

LIST OF ABBREVIATIONS

BSA	Bovine Serum Albumin
DDA	Discrete Dipole Approximation
ED	Electron Diffraction
EDX	Energy Dispersion X-ray
EG	Ethylene Glycol
EGFR	Epidermal Growth Factor Receptor
FBS	Fetal Bovine Serum
fcc	face-centered cubic
FFT	Fast Fourier Transform
GA	Glycolaldehyde
HER2	Human Epidermal Growth Factor Receptor-2
HRTEM	High-Resolution Transmission Electron Microscopy
ICP-MS	Inductively Coupled Plasma Mass Spectrometry
LSPR	Localized Surface Plasmon Resonance
NIR	Near-Infrared
NHS	N-Hydroysuccinimide or Succinimidyl Ester
OCT	Optical Coherence Tomography
OPSS-PEG-NHS	Orthopyridyl disulfide-poly(ethylene glycol)-succinimidyl ester
OPSS-PEG-SC	Orthopyridyl disulfide-poly(ethylene glycol)-succinimidyl carbonate

OPSS-PEG-SVA	Orthopyridyl disulfide-poly(ethylene glycol)-succinimidyl valerate
PAT	Photoacoustic Tomography
PI	Propidium Iodide
PBS	Phosphate Buffered Saline
PEG	Poly(ethylene glycol)
PL	Photoluminescence
ppb	Part-per-billion
ppm	Part-per-million
PVP	Poly(vinyl pyrrolidone)
RME	Receptor-Mediated Endocytosis
SERS	Surface-Enhanced Raman Scattering
SHE	Standard Hydrogen Electrode
SEM	Scanning Electron Microscopy
SK-BR-3	Breast Carcinoma Cell Line
TEM	Transmission Electron Microscopy
TBS	Tris-Buffered Saline
UV-Vis	Ultraviolet-Visible
XRD	X-Ray Diffraction

Chapter 1

Introduction

1.1 Gold Nanostructures

The beauty of gold lies not only in its yellow metallic luster, but also in its usefulness derived from a diversity of properties. It is the most malleable and ductile of all metal; a single gram can be pounded into one square meter. This noble metal does not tarnish in air or water, making it attractive for a number of applications. For instance, gold has been hammered into thin sheets and drawn into wires for decorative ornaments and jewelry since ancient times. It has also been used in dentistry for fillings and crowns because of its bio-inert nature and ease to mold into different shapes. Gold is an excellent conductor of heat and electricity and is used in the electronic, computer and aerospace industry. With all of these favorable properties, it is no wonder this precious metal was used as a medium of monetary exchange.[1]

When the dimension of Au structures reaches the nanoscale, typically with at least one dimension between 1 nm to 100 nm, they exhibit unique and fascinating properties that are complementary or superior to their bulk counterparts.[2] For instance, gold is no longer non-reactive when in the form of particles smaller than 8 nm in diameter; rather, they become a highly active model catalyst which can be used in the automotive industry.[3] Moreover, Au nanoparticles have been used in colorful glassware for thousands of years. The oldest known example is the Lycurgus cup that dates back to the late fourth century. Silver and gold nanoparticles with diameter ~70 nm are embedded in the glass wall of the cup, which reflects green light and transmits ruby red light. This observation of colors is built upon the unique scattering and absorption properties of nanoparticles which will be discussed in the next section.

1.2 Surface Plasmonic Properties of Gold Nanostructures

Gold nanostructures have gained significant attention because of their unique and tunable localized surface plasmon resonance (LSPR) properties.[4-6] This optical phenomenon occurs when the conduction electrons in the metal nanostructure collectively oscillate with the electrical field of light (Figure 1.1).[7] LSPR is responsible for the brilliant colors of metal colloids, such as those first prepared by Michael Faraday in 1856 from the chemical reduction of gold chloride with phosphorus in water.[8] At the resonant frequency, the incident photons can either be scattered in all directions or absorbed and subsequently converted into phonons (i.e., vibrations of the lattice). Therefore, the LSPR peak of a metal nanostructure typically includes both scattering and absorption components.

Interestingly, the resonant frequency and the cross-sections of both scattering and absorption components are dependent on the size, shape, and chemical composition of the nanostructure.[9-13] This observation allows one to tune the LSPR features of metal nanostructures, making such materials potentially useful. For example, Au colloids with their LSPR peaks in the visible region have been demonstrated for colorimetric sensing in the selective detection of heavy metal ions and various biomolecules.[14,15]

The LSPR spectra of nanostructures can be predicted by solving Maxwell's equation. In 1908, Gustav Mie solved Maxwell's equation for solid spherical particles with dimensions less than the wavelength of light.[16] The formulas derived by Mie can be used to compute the LSPR spectra (including both scattering and absorption) of a spherical particle of any size. It was calculated that Au nanospheres 40 nm in diameter would have an extinction peak centered at 520 nm, whereas smaller Au nanospheres would be slightly blue-shifted and larger Au spheres would be slightly red-shifted (e.g., Au colloids 140 nm in diameter would have an LSPR peak around 650 nm). These calculations have been validated experimentally, demonstrating the utility of Mie's formula for predicting the LSPR spectra of spherical particles. Such computations, however, also indicate that different types of nanostructure must be fabricated in order to produce Au nanostructures with their LSPR peaks tuned to the near-infrared.

To this end, researchers have explored the following Au nanostructures: i) aggregates of spherical nanoparticles;[17,18] ii) nanorods;[19-24] and iii) composite or hollow nanostructures.[25-31] The third option is particularly interesting as different surfaces and/or hollow interiors provide a platform for multi-functionalization and encapsulation. In 1989, Neeves and Birnboim calculated the LSPR spectra for composite spherical particles (i.e., those consisting of a metal shell and dielectric core such as silica or air) and found that they would give rise to LSPR modes extending into the near-infrared region.[32,33] It has, however, been difficult to verify these predictions experimentally.

Halas and coworkers were among the first to prepare such materials and validated the calculations of Neeves and Birnboim.[34,35] Halas' approach to generate Au nanoshells of variable thickness was to deposit gold onto silica or polymer beads via a direct deposition/chemical reduction method.[36] While this approach has been used as a general synthetic route to dielectric/metallic core-shell particles, the preparation of such composite structures is nontrivial, since most metals do not sufficiently wet the surface of an oxide or polymeric material.[37] In addition, it is very difficult to obtain a smooth surface coating, together with accurate control over the shell thickness on the scale of a few nanometers. Alternatively, the Xia group has recently demonstrated the capability and feasibility to prepare Au nanostructures with hollow interiors via a galvanic replacement reaction with Ag nanostructures as a sacrificial template.[38-41] Using this approach, hollow and porous Au nanostructures can be routinely synthesized from Ag nanostructures of any morphology.

1.3 Biomedical Applications of Gold Nanostructures

Gold nanostructures are ideal for biomedical applications due to their bio-inert nature and strong interaction with the thiolate group, allowing for the attachment of a variety of surface functional groups to enhance circulation in the blood and thus target the malignant cells in a solid tumor.[42] Furthermore, the optical properties of these nanostructures can be readily tailored by controlling their size, shape, composition, and/or interior (hollow *vs.* solid),[42-45] so that their LSPR peaks can be tuned into the near-infrared region (700 to 1200 nm), where soft tissue, blood, and water has minimum absorption (Figure 1.2).[46] A wealth of research has been conducted in the development of Au nanostructures for biomedical research, particularly for the diagnosis and treatment of cancer.

Cancer is the second leading cause of death in the United States, trailing only behind heart disease.[47] Despite the recent advances in the treatment of cancer, far too many cases are diagnosed only after tumors have metastasized. Consequently, patients with cancer are confronted with a grim prognosis and often need to undergo toxic and uncomfortable whole-body chemotherapy and/or other radiation treatments. Early detection and better treatments of cancer can significantly reduce the number of deaths caused by cancer. Table 1.1 shows the average five-year survival rates are higher for several types of cancers when detected and treated at the earlier stages.[48] Nanofunctional materials are in a unique position to transform the diagnosis, imaging, and treatment of cancer.[49] The nanoscale is on the appropriate length scale to enter cells and to interact with similar-sized biomolecules such as proteins and receptor sites. Gold nanostructures have already been implemented in several applications. For instance, nanoshells, nanorods, and nanocages have been used as optical contrast agents for optical coherence tomography (OCT) and photoacoustic tomography (PAT), as well as photothermal agents for the treatment of cancerous cells *in vitro* and *in vivo*.[27-31,50-55] Gold nanostructures provide a promising platform for the cancer diagnosis and treatment; however, there are still a number of challenges that need to be overcome to reach clinical utility.

1.4 Scope of This Work

This dissertation presents the synthesis and optical properties of Au nanostructures for biomedical applications. My work aims to engineer Au nanostructures with LSPR peaks in the near-infrared region and strong absorption properties for use as imaging agents and photothermal transducers for the diagnosis and treatment of cancerous cells.

Chapter 2 discusses the use of the galvanic replacement reaction in generating hollow nanostructures of gold. It compares the galvanic replacement reactions between Ag nanocubes and two Au precursors with different oxidation numbers: $AuCl_2^-$ and $AuCl_4^-$. While both precursors give nanostructures with hollow interiors, the reactions go through different morphological, compositional, and spectral evolutions with the progressive addition of each Au precursor. This observation is probably due to the different reaction stoichiometry: each $AuCl_4^-$ reacts with three Ag to generate one Au and two vacancies in the nanostructure template, while $AuCl_2^-$ reacts with Ag at a 1:1 ratio and thus leaving no vacancies. The galvanic replacement reaction with $AuCl_4^-$ produces Au nanocages while the reaction with $AuCl_2^-$ generates Au nanoframes. The LSPR properties of these hollow nanostructures are explored by a combination of discrete dipole approximation calculation (DDA) and single-nanoparticle spectroscopy. The size, thickness, and porosity of the nanostructures determined the LSPR peak position as well as their scattering and absorption cross-section properties.

Chapter 3 focuses on the use of Au nanocages for two-photon photoluminescence imaging of U87MGwtEGFR glioblastoma cells. Gold nanocages with LSPR peaks in the near-infrared region exhibited a broad photoluminescence band extending from 400 to 700 nm when excited with a Ti:sapphire laser. This phenomenon enables me to exploit Au nanocages as a new class of optical imaging agents for two-photon microscopy. I demonstrate the use of two-photon microscopy as a simple and convenient tool to examine the uptake of antibody-conjugated and PEGylated Au nanocages by U87MGwtEGFR cells. I have also correlated the results from two-photon microscopy with the data obtained using inductively coupled plasma mass spectrometry. My results indicate that the antibody-conjugated Au nanocages were bounded to the surface of cells and then internalized into the cells *via* receptor-mediated endocytosis. The cellular uptake process was dependent on a number of parameters, including the incubation time, the incubation temperature, the number of antibodies immobilized on each nanocage, and the dimension of the Au nanocages.

Chapter 4 quantifies the photothermal effect of Au nanocages targeted to SK-BR-3 breast cancer cells. Gold nanocages with an average edge length of 65±7 nm and a strong absorption peak at 800 nm are conjugated with monoclonal antibodies (anti-HER2) to target SK-BR-3 through the epidermal growth factor receptor (in this case, HER2), which is overexpressed on the surfaces of the cells. Both the number of immuno Au nanocages immobilized per cell and the photothermal therapeutic effect are quantified using flow cytometry. The targeted cells are irradiated with a pulsed near-infrared laser, and by varying the power density, the duration of laser exposure, and the time of response after irradiation, I are able to optimize the treatment conditions to achieve effective destruction of the cancer cells. I found that cells targeted with the antibody-conjugated Au nanocages responded immediately to laser irradiation and that the cellular damage was irreversible at power densities greater than 1.6 W/cm^2. The percentage of dead cells increase with increasing exposure time up to 5 min and then becomes steady. By quantifying the photothermal effect of immuno Au nanocages, critical information with regards to both the optimal dosage of nanocages and parameters of the laser irradiation has been garnered and will be applied to future *in vivo* studies.

Chapter 5 covers the synthesis of Au microplates in aqueous solutions by reducing $HAuCl_4$ with the hydroxyl groups in the serine and threonine units of bovine serum albumin (BSA). I induce structural changes to the protein using temperature, pH, and ionic strength to expose these hydroxyl groups. I investigate the effects of these three parameters on the structure of BSA and the synthesis of Au structures. The optimal experimental condition to produce Au microplates was at elevated temperatures (55 ^oC), in acidic conditions ($pH \approx 3$), and in the presence of NaCl (0.14 M).

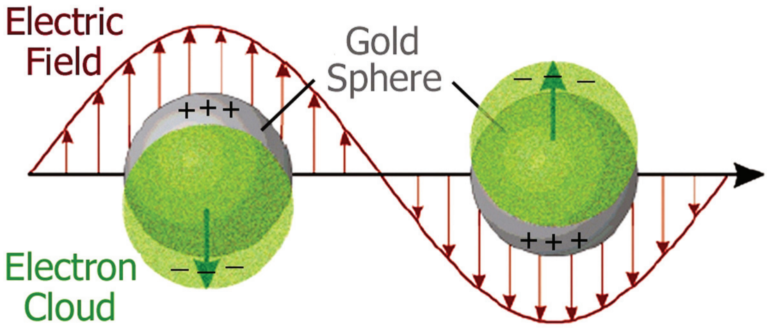

Figure 1.1 Schematic illustration of the collective oscillation of free electrons that are localized in a spherical Au colloid in the electric field of incident light (reproduced from ref. [7]).

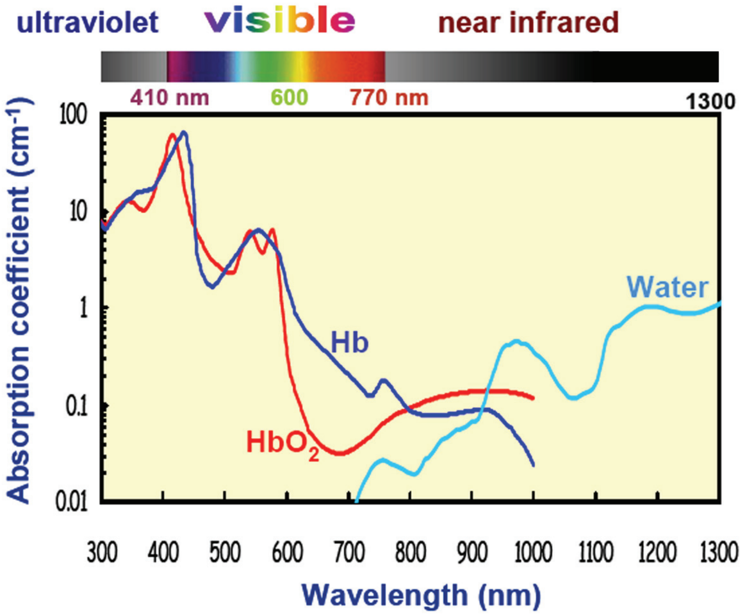

Figure 1.2 Absorption spectra of deoxy-hemoglobin (Hb), oxyhemoglobin (HbO_2), and water. The concentrations of Hb and HbO_2 are adjusted to 50 mM (reproduced from ref. [46]).

Table 1.1 Average Five-Year Survival Rates from Stage of First Diagnosis for Several Cancer Types (reproduced from ref. [49]).

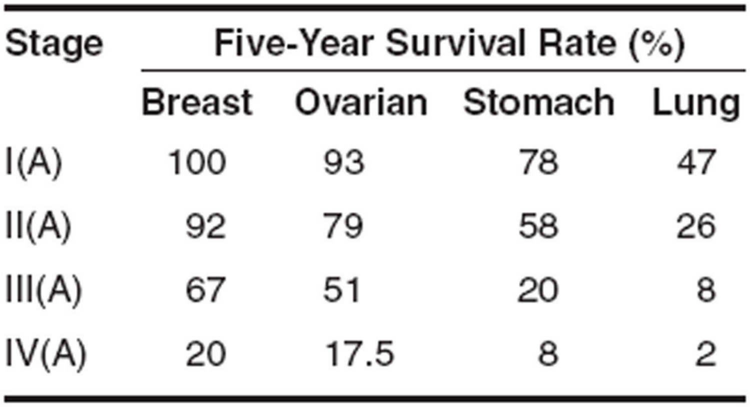

Stage	Five-Year Survival Rate (%)			
	Breast	Ovarian	Stomach	Lung
I(A)	100	93	78	47
II(A)	92	79	58	26
III(A)	67	51	20	8
IV(A)	20	17.5	8	2

1.4 Notes to Chapter 1

[1] http://geology.com/minerals/gold/uses-of-gold.shtml.

[2] Ventra, M. D.; Evoy, S.; Heflin, J. R. Introduction to Nanoscale Science and Technology; Kluwer Academic Publishers: Boston, 2004.

[3] Campbell, C. T. *Science* **2004**, *306*, 234.

[4] El-Sayed, M. A. *Acc. Chem. Res.* **2001**, *34*, 257.

[5] Kreibig, U.; Vollmer, M. Optical Properties of Metal Clusters; Springer: New York, 1995.

[6] Templeton, A. C.; Wuefling, W. P.; Murray, R. W. *Acc. Chem. Res.* **2000**, *33*, 27.

[7] Xia, Y.; Halas, N. J. *MRS Bull.* **2005**, *30*, 338.

[8] Faraday, M. *Philos. Trans. R. Soc. London* **1857**, *147*, 145.

[9] Kreibig, U. G., L. *Surf. Sci.* **1987**, *156*, 678.

[10] Novak, J. P.; Feldheim, D. L. *J. Am. Chem. Soc.* **2000**, *122*, 3979.

[11] Sarkar, D.; Halas, N. J. *Phys. Rev. E* **1997**, *56*, 1102.

[12] Sun, Y.; Xia, Y. *Anal. Chem.* **2002**, *74*, 5297.

[13] Yu, Y. Y.; Chang, S. S.; Lee, C. L.; Wang, C. R. C. *J. Phys. Chem. B* **1997**, *101*, 6661.

[14] Elghanian, R. S., J.J.; Mucic, R.C.; Letsinger, R.L.; Mirkin, C.A. *Science* **1997**, *277*, 1078l.

[15] Liu, J.; Lu, Y. *J. Am. Chem. Soc.* **2003**, *125*, 6642.

[16] Mie, G. *Ann. Phys.* **1908**, *25*, 377.

[17] Blatchford, C. G.; Campbell, J. R.; Creigton, J. A. *Surf. Sci.* **1992**, *120*, 435.

[18] Quinten, M.; Kreibig, U. *Surf. Sci.* **1986**, *172*, 557.

[19] Chang, S.; Chao-Wen, S.; Cheng-Dah, C.; Wei-Cheng, L.; Wang, C.R. C. *Langmuir* **1999**, *15*, 701.

[20] Foss, C. A. H., G.L.; Stockert, J.A.; Martin, C.R. *J. Phys. Chem. B* **1994**, *98*, 2963.

[21] Link, S.; El-Sayed M. A. *J. Phys. Chem. B* **1999**, *103*, 8410.

[22] Murphy, C. J.; Jana, N.R. *Adv. Mater.* **2002**, *14*, 80.

[23] Van der Zande, B.; Bohmer, M.R.; Fokkink, L. G. J.; Schonenberger, C. *J. Phys. Chem. B* **1997**, *101*, 852.

[24] Kim, S. W.; Kim, M.; Lee, W. Y.; Hyeon, T. *J. Am. Chem. Soc.* **2002**, *124*, 7642.

[25] LizMarsan, L. M.; Grersig, M.; Mulvaney, P. *Langmuir* **1996**, *12*, 4329.

[26] Oldenburg, S. J.; Jackson, J. B.; Westcott, S. L.; Halas, N. J. *Appl. Phys. Lett.* **1999**, *75*, 2897.

[27] Cang, H.; Sun, T.; Li, Z.-Y.; Chen, J.; Wiley, B. J.; Xia, Y.; Li, X. *Opt. Lett.* **2005**, *30*, 3048.

[28] Chen, J.; Wang, D.; Xi, J.; Au, L.; Siekkinen, A.; Warsen, A.; Li, Z.-Y.; Zhang, H.; Xia, Y.; Li, X. *Nano Lett.* **2007**, *7*, 1318.

[29] Chen, J. Y.; Li, Z.-Y.; Au, L.; Hartland, G. V.; Li, X. D.; Marquez, M.; Xia, Y. *Chem. Soc. Rev.* **2006**, *35*, 1084.

[30] Loo, C.; Lin, A.; Hirsch, L.; Lee, M. H.; Barton, J.; Halas, N.; West, J.; Drezek, R. *Technol. Cancer Res. Treat.* **2004**, *3*, 33.

[31] West, J. L.; Halas, N. J. *Annu. Rev. Biomed. Eng.* **2003**, *5*, 285.

[32] Aden, A. L. K., M. *J. Appl. Phys.* **1951**, *22*, 1242.

[33] Neeves, A. E.; Birnboim, M. H. *J. Opt. Soc. Am. B* **1989**, *6*, 787.

[34] Averitt, R. D.; Sarkar, D.; Halas, N. J. *Phys. Rev. Lett.* **1997**, *78*, 4217.

[35] Oldenberg, S. J.; Averitt, R. D.; Westcott, S. L.; Halas, N. J. *Chem. Phys. Lett.* **1998**, *28*, 243.

[36] Averitt, R. D.; Westcott, S. L.; Halas, N. J. *J. Opt. Soc. Am. B* **1999**, *16*, 1824.

[37] Charnay, C.; Lee, A.; Man, S. Q.; Moran, C. E.; Radloff, C.; Bradley, R. K.; Halas, N. J. *J. Phys. Chem. B* **2003**, *107*, 7327.

[38] Sun, Y.; Mayer, B.; Xia, Y. *Nano Lett.* **2002**, *2*, 481.

[39] Sun, Y.; Mayers, B.; Herricks, T.; Xia, Y. *Nano Lett.* **2003**, *3*, 955.

[40] Sun, Y.; Mayers, B.; Xia, Y. *Adv. Mater.* **2003**, *15*, 641.

[41] Sun, Y.; Xia, Y. *Science* **2002**, *298*, 2176.

[42] El-Sayed, M. A. *Acc. Chem. Res.* **2001**, *34*, 257.

[43] Noguez, C. *J. Phys. Chem. C* **2007**, *111*, 3806.

[44] Wiley, B.; Sun, Y.; Xia, Y. *Acc. Chem. Res.* **2007**, *40*, 1067.

[45] Xia, Y.; Yang, P.; Sun, Y.; Wu, Y.; Mayers, B.; Gates, B.; Yin, Y.; Kim, F.; Yan, H. *Adv. Mater.* **2003**, *15*, 353.

[46] http://ase.tufts.edu/biomedical/research/Fantini/researchAreas/NearInfraredSpectroscopy.pdf.

[47] http://www.cdc.gov/nchs/fastats/lcod.htm.

[48] Grodzinski, P.; Silver, M.; Molnar, L. K. *Expert Rev. Mol. Diagn.* **2006**, *6*, 307.

[49] Nagahara, L. A.; Ferrari, M.; Grodzinshi, P. *MRS Bull.* **2009**, *34*, 406.

[50] Liao, H. W. N., C.L.; Hafner, J.H. *Nanomed.* **2006**, *1*, 201.

[51] Sokolov, K.; Follen, M.; Aaron, J.; Pavlova, I.; Malpica, A.; Lotan, R.; Richards-Kortum, R. *Cancer Res.* **2003**, *63*, 1999.

[52] Song, K. H.; Kim, C.; Cobley, C. M.; Xia, Y.; Wang, L. V. *Nano Lett.* **2009**, *9*, 183.

[53] Yang, X.; Skrabalak, S. E.; Li, Z.-Y.; Xia, Y.; Wang, L. V. *Nano Lett.* **2007**, *7*, 3798.

[54] Chen, J.; Saeki, F.; Wiley, B. J.; Cang, H.; Cobb, M. J.; Li, Z.-Y.; Au, L.; Zhang, H.; Kimmey, M. B.; Li, X.; Xia, Y. *Nano Lett.* **2005**, *5*, 473.

[55] Chen, J.; Wiley, B. J.; Li, Z.-Y.; Campbell, D.; Saeki, F.; Cang, H.; Au, L.; Lee, J.; Li, X.; Xia, Y. *Adv. Mater.* **2005**, *17*, 2255.

Chapter 2

Hollow Nanostructures of Gold

2.1 Introduction

Hollow nanostructures of noble metals (e.g. Au, Pt, and Pd) have gained attention in recent years for a variety of applications including catalysis,[1] optical sensing,[2] drug delivery,[3] biomedical imaging[4-6] and photothermal therapy[7-10] due to their tunable optical properties and large surface areas. Among various synthetic approaches, the galvanic replacement reaction represents the most versatile route to bimetallic hollow nanostructures.[1,11-16] Bimetallic hollow nanostructures consisting of Ag and Au, Pt or Pd have been synthesized by reacting Ag nanostructures (or templates) with a salt precursor containing a less reactive metal such as Au, Pt or Pd.

In this chapter, I explore the replacement reaction between Ag nanocubes and $AuCl_4^-$ or $AuCl_2^-$ as a robust method for generating hollowing nanostructures in the form of nanoboxes, nanocages, and nanoframes. There are three main sections in this chapter. In the first section, I briefly describe the synthesis of Au nanocages via the galvanic replacement reaction using $AuCl_4^-$. This discussion is followed by an account of their optical properties. In the second section, I study the effect of changing the stoichiometry of the galvanic replacement reaction by using a Au precursor with a different oxidation state, $AuCl_2^-$. I report a detailed account of the morphological and optical differences of the products obtained using the replacement reaction involving Ag nanocubes and $AuCl_2^-$ or $AuCl_4^-$. In the third section, I discuss the synthesis of Au nanoframes via the galvanic replacement reaction using $AuCl_2^-$, followed by a discussion of their optical properties.

2.2 Gold Nanocages

Gold nanocages are single-crystalline, hollow structures with porous walls. They are commonly prepared using the galvanic replacement reaction between Ag nanocubes and $AuCl_4^-$. To prepare Au nanocages, I have to first prepare the sacrificial templates -- uniform Ag nanocubes.

2.2.1 Synthesis of Gold Nanocages

The Ag nanocubes are most commonly synthesized using the polyol method, which involves heating ethylene glycol, $AgNO_3$, and poly(vinyl pyrrolidone) (PVP).[17] These three components function as the reducing agent/solvent, metal precursor, and capping agent, respectively. In a typical reaction, ethylene glycol is heated to 150-160 °C in air to generate glycolaldehyde (Eq. 2.1).[18]

$$2HOCH_2CH_2OH + O_2 \rightarrow 2HOCH_2CHO + H_2O \qquad (2.1)$$

Glycolaldehyde then reduces the Ag^+ ions to Ag atoms which subsequently agglomerate to form nuclei and seeds. As more Ag atoms are produced, the seeds grow into different nanostructures depending on their crystallinity. The role of PVP is to direct the addition of atoms to the {111} facets, due to its stronger binding affinity toward the {100} facets.

For example, Ag pentagonal nanorods in the presence of PVP will extend to form nanowires since PVP will bind to the {100} side faces, facilitating the addition of Ag atoms onto the {111} facets at the ends of the wire.[19] Similarly, in the case of the single-crystal Ag cubooctahedrons, PVP will block the addition of atoms onto the {100} side facets, allowing Ag atoms to add onto the {111} corner facets and promoting their growth into Ag nanocubes with sharp corners.

In order to synthesize nanocubes in high yields, it is crucial to control the crystallinity of the initial seeds. In one method developed in our group, we selectively remove twinned seeds by oxidative etching with O_2 and Cl^-, leaving behind only single-crystal seeds, which grow into Ag nanocubes.[20] Ag nanocubes of different sizes can be routinely produced through this etching method, Figure 2.1. Most recently, I have demonstrated a much faster method that eliminate the formation of twinned seeds by increasing the reduction rate of Ag^+.[21,22] This process was achieved by introducing a trace amount (on the ppm level) of Na_2S or NaHS to the reaction, producing Ag_2S nanocrystallites that can catalyze the reduction of additional Ag^+. This method has significantly reduced the overall reaction time from 10-24 hours to less than 20 minutes and is now the most commonly used protocol for producing Ag nanocubes in large quantities.

The galvanic replacement reaction provides a simple and versatile method for generating hollow nanostructures with tunable plasmonic properties, such as the Au nanocages shown in Figure 2.2A.[19,22-26] When an aqueous suspension of Ag nanocubes with sharp corners is titrated with an aqueous solution of $AuCl_4^-$, the galvanic replacement reaction between these two species occurs immediately, leading to the formation of Au-based nanoboxes and eventually porous nanocages.[25] This reaction follows a template-engaged hollowing out mechanism.[13,25,27,28] Briefly, $AuCl_4^-$ oxidizes the sacrificial Ag template to AgCl, which is highly soluble at the boiling temperature used for the reaction (Eq. 2.2).[29]

$$3Ag(s) + AuCl_4^-(aq) \rightarrow 3\,Ag^+(aq) + Au(s) + 4Cl^-(aq) \qquad (2.2)$$

The driving force for this reaction originates from the difference in standard reduction potential for the $AuCl_4^-/Au$ pair (0.99 V vs. the standard hydrogen electrode, SHE) and the AgCl/Ag pair (0.22 V). The electrons generated in the oxidation process migrate to the surface of the Ag cubes and reduce $AuCl_4^-$ to Au atoms. Gold atoms are able to epitaxially nucleate and grow on the surface of the Ag template since Au and Ag share the same face-centered cubic (*fcc*) structure with closely matching lattice constants (4.0786 and 4.0862Å, respectively). The morphological details of this reaction will be further discussed in Section 2.3.

2.2.2 Optical Properties of Gold Nanocages

One of the great advantages of the synthesis based on galvanic replacement reaction is its ability to precisely tune the LSPR peak of Au nanocages to a specific wavelength. In this way, the synthesis can be optimized for maximum absorption at the wavelength needed for a specific laser or application. For biological applications, the region of interest is in the near-infrared (800-900 nm), where soft tissue and blood are optically transparent. Figure 2.2B shows that by simply adjusting the amount of $AuCl_4^-$

added, the peak can be shifted controllably from ~450 nm for the 50-nm Ag nanocube template to ~900 nm when fully transformed into porous Au nanocages. It is easy to monitor the peak position during the reaction with UV-visible (UV-vis) spectroscopy, allowing for precise tuning.

It has been shown that the size, wall thickness, and porosity of the hollow nanostructures all have a strong effect on the absorption and scattering cross-sections.[30-35] To better engineer Au nanocages for biomedical applications, I calculated the theoretical spectra for a number of different types of cages. Gustav Mie solved Maxwell's equations to generate an exact formula for optical extinction; however, this method is only limited to geometries with spherical symmetry and is consequently not suitable for studying Au nanocages.[36] Instead, I use the discrete dipole approximation (DDA), which has been demonstrated to be reliable for calculating the optical properties of nanostructures with arbitrary geometries.[32,37,38] The DDA method approximates a nanostructure as a cubic array of polarizable units that interact both with the incident field and each other. The resulting polarization at each point can be used to calculate the overall optical cross-section of the particle at any wavelength, generating simulated spectra.

Figure 2.3, A and B, compares the calculated extinction (C_{ext}), absorption (C_{abs}), and scattering (C_{sca}) coefficients (note that $C_{ext}=C_{abs}+C_{sca}$) for Au nanoboxes 60 and 40 nm in edge length, respectively, with the wall thickness being 5 nm.[6] Nanoboxes have hollow interiors and nonporous walls, whereas nanocages have walls with holes. The refractive index of bulk Au was used, and the nanobox was assumed to be surrounded by and completely filled with water. As expected from studies of solid Au particles, absorption dominates the extinction spectra at small sizes (<40 nm), while scattering dominates at larger sizes (>60 nm). These nanoboxes have absorption cross-sections at least five orders of magnitude larger than organic chromophores.

Figure 2.3, C and D, shows the influence of reduction in wall thickness and introduction of pores at corners, respectively. Figure 2.3C shows that the extinction peak was red-shifted from 710 nm to 820 nm when the wall thickness of the nanobox was reduced from 5 nm to 3 nm. Interestingly, the magnitudes of both scattering and absorption cross-sections only changed slightly. Figure 2.3D shows the calculated spectra of a nanobox similar to that used for Figure 2.3B, except that all eight corners were replaced with holes to form a nanocage. The peak remained roughly at the same position, though a small reduction in the magnitude of the extinction cross-section was observed. Further calculations have shown that the extinction coefficient of a 40-nm Au nanocage linearly decreased with the number of holes.

The calculated spectra match well with what I have observed experimentally with the solution-phase spectra of nanoboxes; the slight broadening of the peak seen in the experimental data can be attributed to the minor differences in the uniformity of the nanostructures (i.e., size, levels of truncation, and wall thickness). These insights into the effect of size, wall thickness, and porosity should allow us to more effectively tune the optical properties of nanocages.

2.3 A Comparative Study of Galvanic Replacement Reactions Involving

Ag Nanocubes and $AuCl_2^-$ or $AuCl_4^-$

According to the stoichiometry between Ag and $AuCl_4^-$ (Eq. 2.2), only one Au atom is formed for every three Ag atoms that are removed. If the $AuCl_4^-$ is replaced with a precursor such as $AuCl_2^-$, the stoichiometry will be changed due to the difference in oxidation number for gold. For the Au(I) precursor, one Au atom will be formed for every Ag atom being oxidized. This change to the amount of Ag consumed relative to the amount of Au generated during the reaction could impact the alloying and dealloying processes. It is also possible that additional flexibility regarding the morphology, wall thickness, and LSPR position of resultant hollow nanostructures could be achieved by using precursors with different oxidation numbers for gold. Herein I report a detailed study of the galvanic replacement reaction between Ag nanocubes and $AuCl_2^-$ in a close comparison with the reaction involving $AuCl_4^-$. Because the standard reduction potential of the $AuCl_2^-$/Au pair (1.11 V *vs.* SHE) is higher than that of the AgCl/Ag, Ag nanocubes can be oxidized by $AuCl_2^-$ (Eq. 2.3).[39] In addition, $AuCl_2^-$ reacts with Ag to form the same products as the reaction between $AuCl_4^-$ and Ag, thus providing a meaningful comparison for the galvanic replacement reactions involving Au(I) and Au(III) precursors.

$$Ag(s) + AuCl_2^-(aq) \rightarrow Au(s) + AgCl(s) + Cl^-(aq) \qquad (2.3)$$

The Ag nanocubes used as the sacrificial template were synthesized using a sulfide-mediated polyol process, described earlier in the chapter, and had a mean edge length of 52 ± 4 nm.[21,22] The galvanic replacement reaction using with $AuCl_2^-$ was similar to the reaction using $AuCl_4^-$, except that due to the low solubility of AuCl in water, a saturated aqueous solution of NaCl was used to dissolve the AuCl through complexation to form water soluble $NaAuCl_2$ species. Note that the presence of excess NaCl in the reaction solution will also make the AgCl soluble by forming a $AgCl_2^-$ complex. I only used freshly prepared $AuCl_2^-$ solutions to avoid its disproportionation, (Eq. 2.4):

$$3Au(I) \rightarrow 2Au(0) + Au(III) \tag{2.4}$$

2.3.1 Morphological Comparison

Figure 2.4 shows scanning electron microscopy (SEM) and transmission electron microscopy (TEM) images of the nanostructures obtained at different stages of the reactions between Ag nanocubes and an aqueous $AuCl_2^-$ solution (Figure 2.4, A-D). For comparison, SEM and TEM images of the products obtained with the use of $AuCl_4^-$ solution at the same concentration are also included (Figure 2.4, E-H). For each stage, the volume of $AuCl_4^-$ solution added to the Ag nanocube suspension was kept at 1/3 of the volume of $AuCl_2^-$, so that ideally the same amount of Ag would be dissolved from the template. At the initial stage of the reaction with $AuCl_2^-$, the Ag nanocubes went through a pitting process in which a pinhole in one of the six {100} faces was observed (Figure 2.4A). As the reaction proceeded, the pinhole disappeared and a void developed which then enlarged within each nanocube template (Figure 2.4, B and C). In the later stages of the reaction, the template was transformed into a cubic void, yielding nanoboxes with a wall thickness of 10.5 ± 1 nm (Figure 2.4D). The outer and inner edge lengths of the nanoboxes were 64 ± 4 nm and 43 ± 4 nm, respectively. The hollow structures were free of large pores or pinholes in the walls, and the corners were slightly truncated.

For the control experiments involving Ag nanocubes and $AuCl_4^-$, the reaction followed the same mechanism that has been discussed in detail in our previous publications.[25] At the early stage, a thin layer of gold formed on the outside of the nanocube and a small pit was observed on one of the six {100} faces (Figure 2.4E). As more $AuCl_4^-$ solution was added, the interior of the template continuously dissolved to yield a nanobox through a combination of galvanic replacement and alloying between Ag and Au (Figure 2.4, F and G). In the later stages, nanocages, with hollow interior and porous walls, were obtained through dealloying of the walls of the nanoboxes (Figure 2.4H). The outer edge length of the nanocages was 60 ± 4 nm, together with a wall thickness of 8 ± 1 nm. On a quick comparison, it is apparent that some morphological differences have resulted from the use of precursors with different oxidation numbers for gold.

Figure 2.5 schematically summarizes the replacement reaction pathways when Ag nanocubes are reacted with $AuCl_2^-$ (Figure 2.5A) and $AuCl_4^-$ (Figure 2.5B), respectively. During the initial stage of both reactions, a thin layer of Au is formed on the surface of the nanocube template. Assuming that the deposited layer of Au can prevent the underneath Ag from being oxidized, a pinhole can serve as the active site for Ag dissolution from the interior of the template. With $AuCl_2^-$, the pinhole disappears with the addition of only a small amount of precursor, marking the second stage of the reaction. In contrast, with $AuCl_4^-$, the pinhole remains open until much more precursor is added in the third stage of the reaction. The early disappearance of the pinhole for the reaction with $AuCl_2^-$ can be attributed to the 1:1 molar ratio between Au generated and Ag consumed; i.e., more Au(0) is deposited per Ag atom being oxidized than the case when $AuCl_4^-$ is used. Consequently, dissolution of the Ag template for the reaction with $AuCl_2^-$ requires a greater volume of precursor solution (stage 4 versus stage 3 in Figure 2.5) than when $AuCl_4^-$ is used because there is no pinhole for the reaction species to diffuse in and out for the former system. Instead, the Ag atoms must diffuse through the Au layer in order to be oxidized and dissolved from the template. Concurrent with the replacement reaction, alloying between Au and Ag occurs because the diffusion rates of Au and Ag are relatively high at 100 ^{o}C[40] and the Au/Ag alloy is more stable than pure Au or Ag.[41]

The hollow nanostructures obtained from the reactions with $AuCl_2^-$ and $AuCl_4^-$ exhibit similar void sizes after the fourth stage, although for both cases the void sizes are smaller than the original Ag template. The difference between the dimensions of the void and the initial Ag template can be attributed to the interdiffusion between Ag and Au; i.e., Ag diffuses away from the core and toward the surface of the template as Au diffuses into the Ag layer. This interdiffusion causes a ~20% reduction for the void size as compared to the dimensions of the Ag nanocube. A similar size change has been reported in nanostructure systems involving the Kirkendall effect.[16,42,43] In these systems, vacancies are formed due to a difference in diffusion rate for the two components. Although interdiffusion between Au and Ag occurs in my system as well, the formation of a hollow interior can be primarily attributed to the template-engaged replacement reaction where Ag leaves the template due to oxidation. As proposed in the void growth process via

Kirkendall-diffusion, small voids are formed near the interface, which then grow in size over time via coalescence.[16,42,43] I have not observed this behavior in the Au/Ag galvanic replacement reaction system. Rather, the void is initiated at the pinhole site and then enlarged to occupy the entire template.

2.3.2 Optical Differences

In addition to the morphological changes, the galvanic replacement reaction between Ag nanocubes and $AuCl_2^-$ went through a series of color changes from yellow to orange, red, purple, and finally blue, in a sequence similar to the reaction with $AuCl_4^-$. The UV-vis spectra taken from these solutions, however, reveal a somewhat different shift in peak position (Figure 2.6). For the reaction between Ag nanocubes and $AuCl_2^-$, the extinction peak shifted from 435 nm to 655 nm as more $AuCl_2^-$ was added (Figure 2.6A). When the same stoichiometric volume of $AuCl_4^-$ (3 times the amount of $AuCl_2^-$) was added to Ag nanocubes, the extinction peak continuously shifted to 780 nm for the reaction with $AuCl_4^-$ (Figure 2.6B). Also, the peaks of the UV-vis spectra recorded from the reaction with $AuCl_2^-$ were broader than that of $AuCl_4^-$. Based on the TEM images shown in Figure 2.4, A-D, this peak broadening is probably related to a wider range of void sizes in the resultant hollow nanostructures. Because of the early disappearance of the pinhole for the reaction with $AuCl_2^-$, the removal of Ag relies more on Ag diffusion to the surface, thus causing a broader distribution for both void size and wall thickness. As shown previously by DDA method, any variation in wall thickness may result in broadening for the LSPR peak. Figure 2.6C plots the peak position versus the amount of

Au precursor added to the reaction solution. For the early stages of both $AuCl_2^-$ and $AuCl_4^-$, the peak position red-shifted considerably upon addition of the Au precursor. The pitting process strongly influences wall thickness, resulting in a dramatic change in the LSPR peak position. As more solution was added, the plot tapered in the later stages. This trend supports previous DDA calculations that thickness has a dramatic effect on peak position and that the number of holes in the wall has little effect on the peak position.[6,11] It is also worth pointing out that the overall slope for $AuCl_4^-$ is steeper than that of $AuCl_2^-$ signifying that $AuCl_4^-$ red-shifted the extinction peak more effectively (with less precursor solution) than $AuCl_2^-$. Consequently, $AuCl_4^-$ provides a more economical way to red-shift the LSPR peak position. Overall, $AuCl_4^-$ is better than $AuCl_2^-$ at tuning the LSPR scope because it provides a wider range of peak positions due to its ability to dealloy and form thinner walls. On the other hand, $AuCl_2^-$ is a better choice for the preparation of Au-based nanoboxes without pores in the walls because there is a relatively larger range compared to $AuCl_4^-$ where the amount of precursor can form nanoboxes.

2.3.3 Effects of Dealloying

I also studied the late stages of the galvanic replacement reaction with $AuCl_2^-$. As reported in previous publications,[13,25,27,28] during the later stages of the galvanic replacement reaction with $AuCl_4^-$, a dealloying process takes place, allowing Ag to be removed from the Au/Ag alloyed walls. The resultant lattice vacancies formed during the extraction of Ag atoms cause negative curvatures and thus an increase in interfacial area and surface energy for the solid walls.[44] This stress can be released by shape reconstruction, probably via an internal Oswald ripening process,[45] resulting in each corner of the nanobox being truncated to form a new face enclosed by the {111} crystallographic planes to lower the surface energy. A different reconstruction was observed for the later stages of the replacement reaction when $AuCl_2^-$ was used as a precursor. As more $AuCl_2^-$ solution was added to the suspension of nanoboxes with slightly truncated corners (Figure 2.7A), the center of the faces became porous and nanoframes with edge length 61 ± 3 nm and thickness about 17 ± 2 nm were obtained (Figure 2.7B). The formation of nanoframes contrasts with that of nanocages synthesized from the reaction with $AuCl_4^-$, and this difference in morphology is again related to the amount of Au(0) being deposited per each Ag(0) dissolved. In the case of $AuCl_4^-$, only one Au(0) atom is formed per every three Ag(0) atom. As a result, the nanocages formed during the dealloying process have extremely thin ridges, which quickly fall apart into discrete nanoparticles. On the other hand, $AuCl_2^-$ generates one Au(0) atom per Ag(0) atom, thus making the ridges of nanocages thicker and more robust to survive the dealloying process. Only when an extreme amount of $AuCl_2^-$ solution was added (22 mL), regions of the nanoframes became globular and fragmented from the structures to form solid Au nanoparticles (Figure 2.7C). The UV-vis spectra of these products show that the addition of $AuCl_2^-$ blue-shifted the LSPR peak from 680 to 550 nm. Energy-dispersive X-ray (EDX) data showed that Ag was still present in the last sample, suggesting that the $AuCl_2^-$ was unable to reach the Ag trapped inside the particle, thus complete dealloying could not occur even with an excess of $AuCl_2^-$. In the case of

$AuCl_4^-$, as more solution was added (5 mL), the dealloying process continued until essentially all the Ag in the alloyed walls was removed. In fact, the walls of the Au nanocages became so porous and fragile that the cages started to shatter into small pieces (Figure 2.8). EDX measurements indicate that these fragments were made entirely of gold.

Table 2.1 summarizes the EDX data taken from the hollow nanostructures obtained at different stages of the reaction. Generally, the percentage of Au increased as more $AuCl_2^-$ or $AuCl_4^-$ solution was added into the reaction. At the early stages, the increase of Au content in the products obtained from the reactions with $AuCl_2^-$ was higher than $AuCl_4^-$. This result is expected as more Au should be generated from the reaction with $AuCl_2^-$ than with $AuCl_4^-$ (at a 3:1 ratio) when the amount of Ag oxidized is held constant. However, at the late reaction stages, this trend is reversed. For instance, when 10 mL of $AuCl_2^-$ solution was added, the product was composed of 59% Au and 41% Ag, whereas for the product obtained from the reaction with 3.3 mL of $AuCl_4^-$, there was 72% Au and 28% Ag. These results confirm that more Ag can be removed via dealloying of the Au/Ag alloyed walls by $AuCl_4^-$ than by $AuCl_2^-$.

2.4 Gold Nanoframes

Previously, cubic Au nanoframes were synthesized by our group in a two-step process, in which a wet etchant such as $Fe(NO_3)_3$ or NH_4OH was used for the selective removal of Ag from the Au-Ag alloy nanostructures after thin layers of Au have been deposited onto the surfaces of Ag nanocubes.[46] This procedure tended to greatly reduce the wall thickness and causes pores to form on the side faces. At a certain point of the reaction, the pores on each side face could coalesce into a single large hole, leading to the formation of a cubic nanoframe, a structure that was not previously achieved with $AuCl_4^-$ alone. However, if this specific point was passed during the synthesis, the Au nanoframe would break into small pieces because the ridges became too thin and fragile. The Au nanoframes formed via this route were so sensitive to the reaction details that the reported yield never exceeded 5-10%. Conversely, when $AuCl_2^-$ is employed as a precursor to Au instead of $AuCl_4^-$, nanoboxes with thicker walls can be generated due to the stoichiometric difference.[47] I postulated this method would improve the yields of nanoframes by increasing the thickness (and thus robustness) of ridges that support the nanoframes. Here I present the facile, one-step synthesis of Au nanoframes with a typical yield of >90%.

2.4.1 Synthesis of Gold Nanoframes

The synthesis of Au nanoframes was based upon the galvanic replacement reaction between Ag nanocubes and $AuCl_2^-$. The Ag nanocubes with an average edge length of 52±4 nm were synthesized by a sulfide-mediated polyol process[21,22] as described earlier in this chapter. The Ag nanocubes then served as a sacrificial template for the formation of Au nanoframes. Figure 2.9 shows SEM and TEM (inset) images of samples obtained at different stages of the galvanic replacement reaction and Figure 2.10 shows a schematic that summarizes this process. In the initial stage, Au deposited on the surface of the Ag cube and a pinhole formed on one of the six side faces, allowing for the exchange of atoms during the pitting process (Figure 2.9A, and step A in Figure 2.10). Shortly after, the pinhole closed, generating a partially hollow structure (Figure 2.9B, and step B in Figure 2.10). The interior of the nanostructure continued to be hollowed out as Ag atoms diffused to the surface of the structure and Au diffused into the structure, leading to the formation of a seamless Au nanobox with slightly truncated corners (Figure 2.9C, and step C in Figure 2.10). This shape reconstruction marked the start of dealloying, where the vacancies from the extraction of Ag atoms caused negative curvatures, resulting in an increase in interfacial area and surface energy for the solid walls.[44] This stress was relieved via an internal Ostwald ripening process and new {111} facets were formed.[45] Since the relative surface energies of different facets are in the order of $\gamma_{111} < \gamma_{100} < \gamma_{110}$ for a *fcc* metal,[48,49] truncated boxes with a larger portion of {111} facets should be more stable than those with sharp corners. The formation of a truncated rather than a perfect cubic shape had also been observed in many other systems.[50,51] Concurrent to the replacement reaction (i.e., Figure 2.9A-C, and steps A-C in Figure 2.10), the rates of diffusion for Ag and Au were accelerated by the relatively high reaction temperature at 100 ^{o}C[40] and subsequently forming a Au-Ag alloy that is more stable than pure Au or Ag alone.[41] When more $AuCl_2^-$ was added, the removal of Ag and deposition of Au occurred at all sites, and pores appeared at corners and side faces (Figure 2.9D, and step D in Figure 2.10). As dealloying continued, the pores on the side faces enlarged while the pores at the corners reduced in size (Figure 2.9E, and step E in Figure 2.10), suggesting that the atoms migrated to the more stable {111} facet. Eventually, the pores at the corners were sealed while the pores on all side faces were enlarged to the maximum size, resulting in the formation of a cubic nanoframe (Figure 2.9F, and step F in Figure 2.10). This point is the critical for harvesting Au nanoframes with a yield approaching 100%. When more $AuCl_2^-$ was added, the ridges would become thinner due to dealloying of Ag atoms from the structure (Figure 2.9G, and step G in Figure 2.10). At a certain point, the ridges became too thin to support the open structure that the nanoframes fragmented and finally evolved into Au nanoparticles (Figure 2.9H, and step H in Figure 2.10).

The SEM image in Figure 2.11A shows Au nanoframes with an average edge length of 63±4 nm and ridge thickness of 19±2 nm that were synthesized under the same condition as for Figure 2.9F. The elemental composition of these nanoframes was determined to be 89% Au and 11% Ag by EDX analysis. To better resolve the three-dimensional structure of the nanoframes, the sample was tilted by 45^o as shown in Figure 2.11B. Figure 2.11C shows a TEM image of the nanoframes, from which one can easily resolve the hollow structures and determine the thickness of the ridges. Figure 2.11D shows a high-resolution TEM image of a corner of the nanoframe taken along the [001] zone axis. This image indicated that the atoms were arranged in a highly ordered lattice with a spacing of 2.04 Å, which can be indexed to the {200} planes of *fcc* Au. The fast Fourier transform (FFT) pattern revealed that the nanoframe was single crystalline in structure. The spots circled and squared can be indexed to the {220} and {200} reflections, respectively.

2.4.2 Optical Properties of Gold Nanoframes

Figure 2.12A summarizes the UV-vis spectra of the structures shown in Figure 2.9, A-F. As more $AuCl_2^-$ was added, a significant red-shift was observed. The UV-vis spectrum of the Au nanoframes (Figure 2.11) had an LSPR peak around 790 nm. The broadness of the peak may be ascribed to the variations in edge length, ridge thickness, and corner sharpness. Potential applications such as imaging, SERS, chemical and biological sensing are dependent upon LSPR properties; therefore, it is important to understand the relationship between these variations and LSPR properties to effectively tune the resonance peak. As it has been established for Au or Ag nanostructures of other shapes, the LSPR property of a nanoframe should depend on several factors including the edge length, ridge thickness, corner sharpness, elemental composition, laser orientation and environment.[6,21,38,52-55] To determine how these factors, specifically the size and shape, influence the LSPR peak, the scattering spectra of individual nanoframes were calculated using the DDA method. After reviewing many spectra, I found a trend between the peak position and the edge length to ridge thickness ratio, *R*. Figure 2.12B shows the spectra calculated for nanoframes with an edge length of 57.0, 59.4, 61.7, 64.1, 66.5, and 68.9 nm, while keeping a composition of 89% Au and 11% Ag. The nanoframes were assumed to have sharp corners as shown in the inset. As the *R* value increased, the peak position red-shifted while the peak intensity slightly increased. Figure 2.12C shows the DDA calculated extinction, absorption and scattering spectra for the nanoframe with R=3.37 and geometry as shown in the inset.

To confirm the theoretical calculations, nanoframes were deposited on indium tin oxide (ITO)-coated glass substrates and the scattering spectra of single nanoframes were collected using an inverted microscope with a transmitted dark-field condenser as previously described.[56-58] The scattering spectra are plotted in Figure 2.12D along with their corresponding SEM images in the inset. I observed that the spectra red-shifted as the *R* value increased, validating the trend found by DDA calculation. This result was expected as a decrease in ridge thickness or increase in edge length would increase the charge separation, thus reducing the restoring force for electron oscillation and resulting in red-shifting for the resonance peak. As previously reported for hollow nanospheres, thinner shells have stronger coupling between charges inside and outside of the shell, causing greater charge separation and further red-shift in peak position.[38] Similar to the calculated spectra, the peak intensity was higher for larger *R* values, and this trend was expected as larger particles scatter more light.

It is worth pointing out that the resonance peaks for the calculated spectra did not completely match the experimental spectra, which can be ascribed to the complexity of the structure. In the ideal situation, a nanoframe has uniform pore size, ridge thickness, edge length in addition to sharp corners as seen in the inset of Figure 2.12B. From the electron microscopy images in Figures 2.11 and 2.12D, it is clear that within one nanoframe there are variations in these features which would result in some shifts for the resonance peak. Additionally, it has been previously shown that the substrate can shift the LSPR peak.[54] Since the DDA calculations of the nanoframes were performed for particles suspended in water, I expect some shifts due to the substrate effect.

The Au nanoframes can also serve as substrates for SERS based detection. Due to their tunable LSPR peaks into the near-infrared region, they are ideal candidates for detection of molecules *in vivo*, as the light source in this region can penetrate deeply into soft tissue. As a demonstration of their SERS application, the Au nanoframes were functionalized with 4-methylbenzenethiol (4-MBT, a common probe molecule for SERS) and their SERS spectrum was recorded in a solution phase setup. Figure 2.13 shows the SERS spectrum for the Au nanoframes functionalized with 4-MBT (spectrum A) along with the ordinary Raman spectrum of 4-MBT (spectrum B), both obtained with excitation at 785 nm. As illustrated in Figure 2.13, the utilization of the Au nanoframes lead to a significant enhancement on the intensity of the 4-MBT signals compared to the spectrum of neat 4-MBT, indicating that they are good substrates for SERS. However, an accurate estimation of the enhancement factor is limited by the complex morphology of the Au nanoframes, which makes it difficult to precisely determine their surface area and, consequently, the number of 4-MBT molecules contributing to the detected SERS signals.

2.5 Summary

Gold nanocages can be routinely prepared via the galvanic replacement reaction between Ag nanocubes and $AuCl_4^-$. By controlling the size of Ag nanocubes, Au nanocages of different sizes can be produced routinely in high yields. The optical properties of these nanocages can also be tailored, allowing for the peak absorption to be precisely tuned well into the near-infrared region by simply titrating $AuCl_4^-$ into a solution of Ag nanocubes. DDA calculations suggest that the observed red-shift of the LSPR peak with increasing $AuCl_4^-$ is mainly due to a reduction in wall thickness. The

DDA calculation clearly indicate that these Au nanocages strongly absorb and scatter light in the near-infrared region, with their absorption cross-sections more than five orders of magnitude larger than those of conventional dyes. Gold nanocages provide a promising platform for the imaging and photothermal treatment of cancer due to their unique optical properties, bio-inertness, and facile surface chemistry. I discuss these biomedical applications in Chapters 3 and 4.

Furthermore, I have demonstrated that a change of stoichiometry between Au deposition and Ag oxidation in galvanic replacement reaction can lead to differences in the morphology, composition, and optical properties of the resultant hollow nanostructures. When Ag nanocubes were reacted with either $AuCl_4^-$ or $AuCl_2^-$, nanoboxes with a hollow interior and a Au/Ag alloy shell were formed at the early stages of reaction. Thicker walls, however, were observed for the nanoboxes obtained from the reaction with $AuCl_2^-$ compared to $AuCl_4^-$. In later stages of replacement, $AuCl_4^-$ dealloyed Ag from the walls of the Au/Ag alloy nanoboxes and formed porous nanocages. Interestingly, Au nanoframes with a yield >90% were synthesized in the reaction with $AuCl_2^-$. The thicker and more robust structure could survive during the dealloying stage to form Au nanoframes. I have also characterized the effect of the dimensional parameters of Au nanoframes on the positions of their LSPR peak. Due to their highly open structure, the nanoframes are potentially useful for SERS detection of analytes such as virus and bacteria with relatively large dimensions.

2.6 Experimental Section

Synthesis of Ag nanocubes. The Ag nanocubes were prepared using the sulfide-mediated polyol process.[21,22] In a typical synthesis, 6 mL EG (J. T. Baker, 9300-03) was preheated to 155 ^{o}C for 1 h under magnetic stirring. EG solutions containing 3 mM Na_2S (Aldrich, 208043), 0.18 M PVP (as calculated in terms of the repeating unit, M_w~55,000, Aldrich, 856568) and 0.28 M $AgNO_3$ (Aldrich, 209139) were prepared. 80 μL of the Na_2S solution was injected into the hot EG, followed by 1.5 mL of the PVP solution and then 0.5 mL of the $AgNO_3$ solution. The reaction underwent color changes from yellow to reddish brown to opaque green-gray with plating on the vial walls. The reaction was completed within 20 min. The reaction solution was diluted with acetone, and the product was isolated by centrifugation. The product was washed twice with deionized water and then collected by centrifugation at 13,000 rpm for 5 min and re-dispersed by brief sonication in 4 mL of deionized water.

Synthesis of Au Nanocages. The Au nanocages were prepared using the galvanic replacement reaction between Ag nanocubes and $AuCl_4^-$. In a typical synthesis, 50 μL of Ag ~3.5 nM nanocubes was dispersed in 5 mL of deionized water containing 1 mg mL^{-1} PVP in a 50 mL flask under magnetic stirring and then heated to boil for 10 min. In the meantime, a 0.2 mM $AuCl_4^-$ (Aldrich, 520918) was prepared. A specific amount (as indicated in the text) of the $AuCl_4^-$ was added to the flask via a syringe pump (Stoelting, KDS-200) at a rate of 45 mL h^{-1} under magnetic stirring. The solution was heated for another 10 min until the color of the reaction was stable. Once cooled to room temperature, the sample was washed with NaCl-saturated solution to remove AgCl and then with water several times to remove PVP and NaCl. The product was then collected by centrifugation at 10,000 rpm and redispersed in water. The product was subsequently imaged by SEM and TEM.

Synthesis of Au nanoframes. The Au nanoframes were prepared using the galvanic replacement reaction between Ag nanocubes and $AuCl_2^-$. In a typical synthesis, 50 μL of Ag ~3.5 nM nanocubes was dispersed in 5 mL of deionized water containing 1 mg mL^{-1} PVP in a 50 mL flask under magnetic stirring and then heated to boil for 10 min. In the meantime, a NaCl-saturated aqueous solution of 0.2 mM AuCl (Aldrich, 481130) was prepared. AuCl was washed three times with chloroform to remove Au(III) and thoroughly dried in the vacuum prior to usage. A specific amount (as indicated in the text) of the NaCl-saturated AuCl was added to the flask via a syringe pump (Stoelting, KDS-200) at a rate of 45 mL h^{-1} under magnetic stirring. The solution was heated for another 10 min until the color of the reaction was stable. Once cooled to room temperature, the sample was washed with NaCl-saturated solution to remove AgCl and then with water several times to remove PVP and NaCl. The product was then collected by centrifugation at 10,000 rpm and redispersed in water. The product was subsequently imaged by SEM and TEM.

Electron Microscopy and Spectroscopy Characterization. SEM or TEM samples were prepared by placing a drop of the final product on a silicon wafer or carbon-coated copper grid, respectively, and drying under ambient conditions. SEM images and EDX data were taken using a Sirion XL field-emission microscope operated at an acceleration voltage of 10 kV. TEM imaging was performed using a Phillips CM100 microscope operated at 100 kV. The UV-vis spectra were obtained using a Varian Cary 50 UV-vis spectrophotometer.

Substrate Preparation for Optical Characterization. ITO-coated glass substrates (Thin Film Devices Inc.) were cleaned by sonication in acetone and then isopropanol for 30 min in each solution and then dried under a nitrogen stream. The substrates were then plasma cleaned (Harrick Plasma, PDC-32G) for 3 min with an applied power of 18 W before immersing in a solution of 1 mM 3-mercaptopropyltrimethoxysilane in ethanol for 4 h. The substrates were then rinsed with ethanol and cured at 90 °C under nitrogen for another 4 h, and thereafter stored at room temperature. Before deposition, the stock solution of Au nanoframes was sonicated for 30 sec. The nanoframes were diluted 20X with water. The Au nanoframes were allowed to bind onto the surface for approximately 2 min, for a final particle density of ~10 particles per 100 μm^2. After depositing, the excess particles were extensively rinsed off the surface, and the substrate was soaked in water for 20 min to remove excess PVP, rinsed in water, and finally dried by nitrogen stream. Scattering spectra were taken with an inverted microscope (Nikon, TE2000) with a transmitted dark-field condenser and 75X effective magnification as previously described.[57-59] After optical measurements, the same Au nanoframes were identified and imaged under SEM with the assistance of registration marks.[52,55,57] This allows us to correlate the optical spectra to the structural and dimensional information obtained from SEM imaging.

Surface-Enhanced Raman Scattering Measurements. The SERS spectrum was obtained from aqueous solution using a Renishaw inVia Raman spectrometer coupled to a Leica DMIRB inverted optical microscope. A diode laser with an excitation wavelength 785 nm was used at a power of 4.5 mW. The backscattered Raman signals were collected on a charge-coupled device detector thermoelectrically cooled to -60 ^{o}C. Sample cells were constructed by trimming the bottoms of plastic micro-centrifuge tubes and affixing the top portions to glass cover slips of thickness between 0.13-0.17 mm. Solution for SERS measurements were prepared by dispersing the Au nanoframes in 1.5 mL of 5 mM ethanolic solution of 4-MBT for 3 h prior to the SERS measurements, followed by successive rounds of centrifugation and washing with ethanol to remove excess 4-MBT. The sample was dried under ambient conditions to remove ethanol and then re-dispersed in 100 μL of water. The ordinary Raman spectrum of 4-MBT was obtained from a 100 mM solution in 12 M aqueous NaOH. To ensure that the focal volume was held constant, a motorized Z-stage with an accuracy of 0.1 μm was used to control the focal depth. This step was done by focusing the interface between the glass and the solution, and then using the motorized stage to adjust the focal plane 50 μm into the solution. Scattering spectra were recorded from 800 to 2000 cm^{-1} by using a grating with 1200 lines per millimeter, a spot size of approximately 1.6 μm, and 30 sec accumulation time.

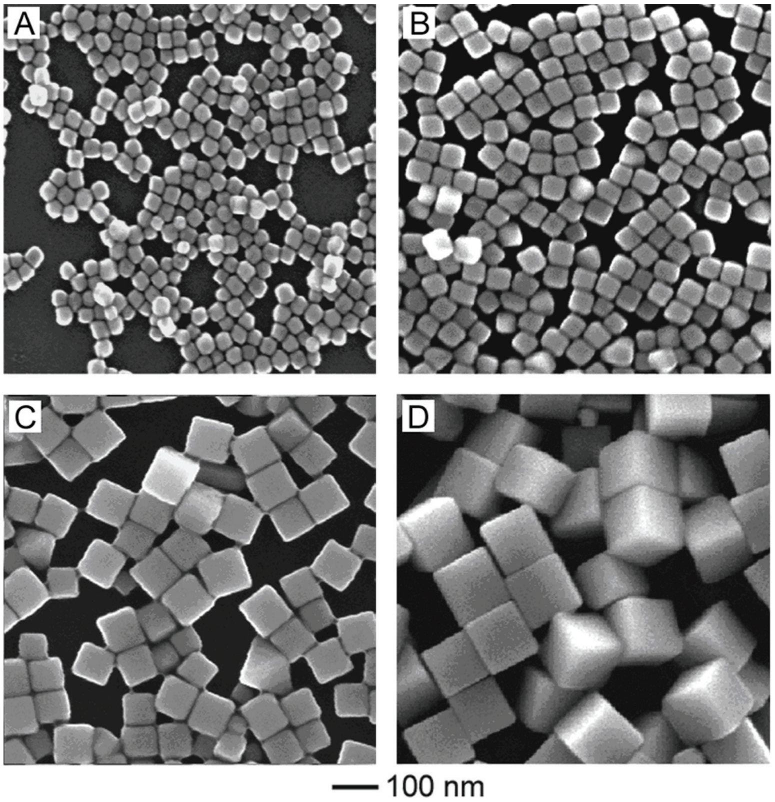

Figure 2.1 Synthesis of Ag nanocubes based on the polyol reduction coupled with an oxidative etching process. SEM images of Ag nanocubes with various sizes: (A) 30 nm; (B) 50 nm; (C) 90 nm; and (D) 110 nm.

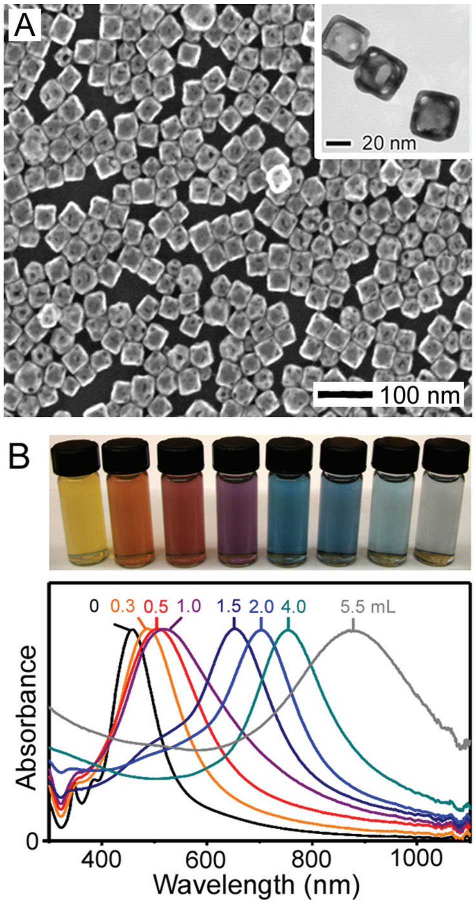

Figure 2.2 Galvanic replacement between Ag nanocubes and $AuCl_4^-$. (A) SEM and TEM (inset) images of typical Au nanocages obtained from this synthesis. (B) The optical resonant peak of Au nanocages can be tuned to different wavelengths depending on the amount of $AuCl_4^-$ added.

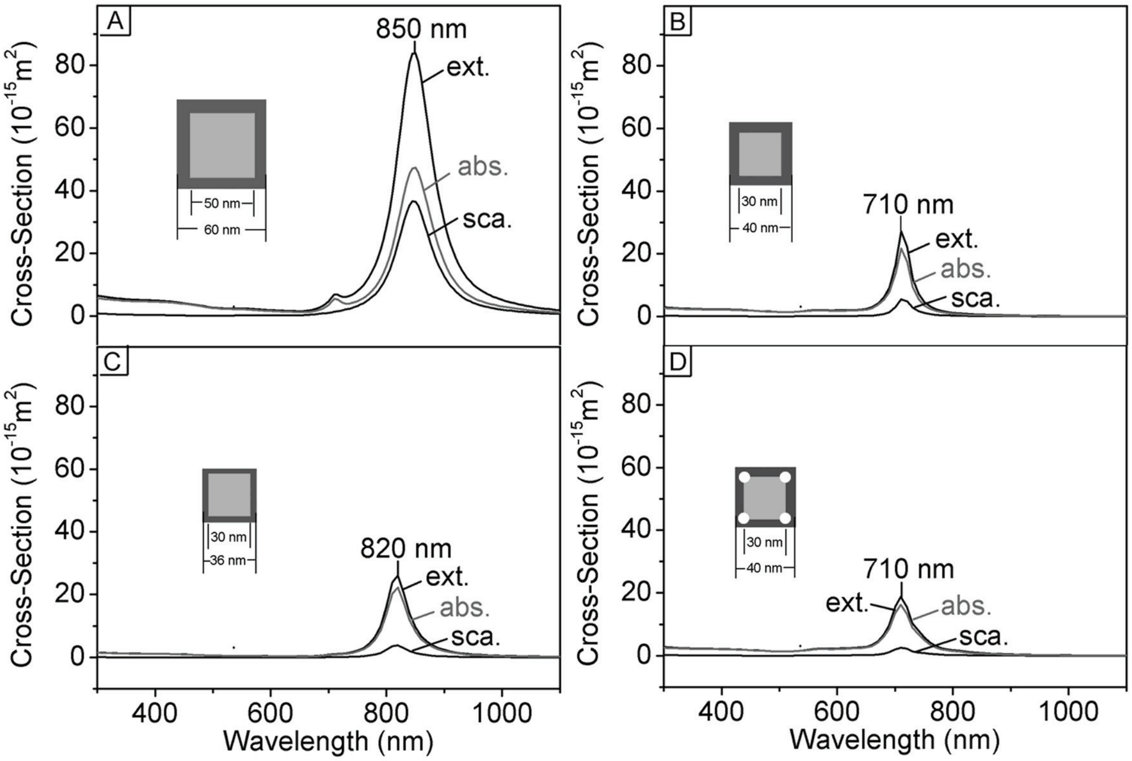

Figure 2.3 Extinction, absorption, and scattering spectra calculated using the DDA method for Au nanocages having four different sets of geometric parameters: (A) a Au nanobox of 50 nm in inner edge length and 5 nm in wall thickness; (B) a Au nanobox of 30 nm in inner edge length and 5 nm in wall thickness; (C) the same as in (B) except that the wall thickness 3 nm; (D) the same as in (B) except that the eight corners are decorated with pores of 5 nm in edge length.

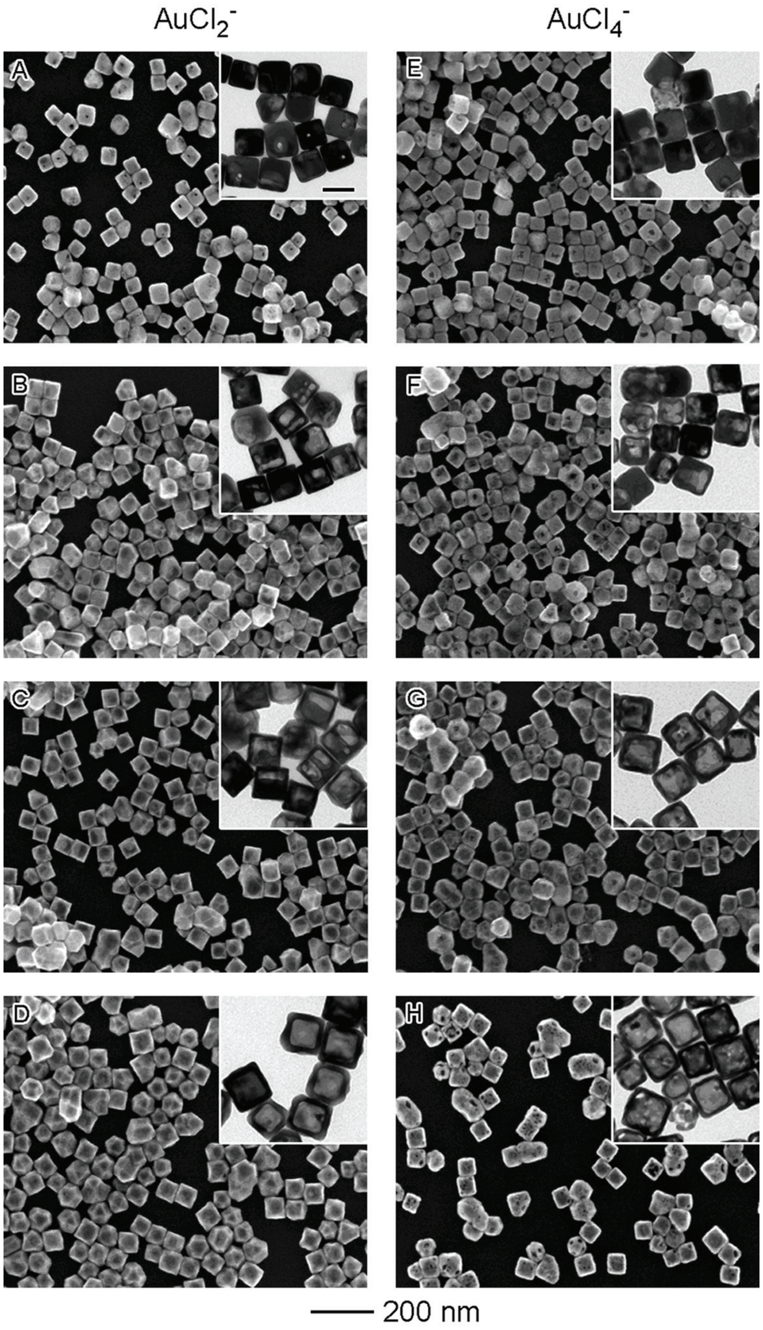

Figure 2.4 SEM and TEM (insets) images showing four different stages involved in the galvanic replacement reaction where Ag nanocubes were titrated with (A-D) 1.0, 3.0, 5.0, 10.0 mL of 0.1 mM $AuCl_2^-$ and (E-H) 0.3, 1.0, 1.6, 3.3 mL of 0.1 mM $AuCl_4^-$, respectively. The scale bar in the inset represents 50 nm and applies to all TEM images.

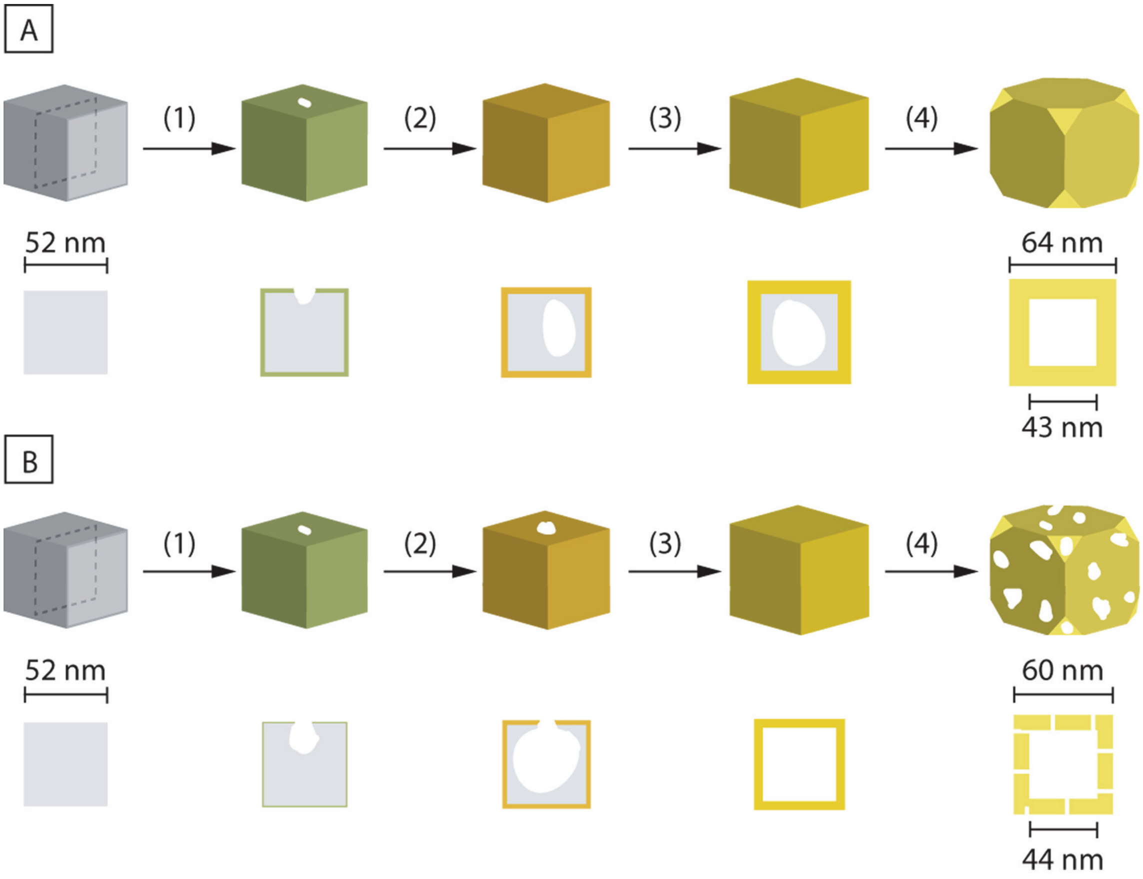

Figure 2.5 Schematic detailing the major differences in terms of morphological and structural changes during the galvanic replacement reaction involving Ag nanocubes and (A) $AuCl_2^-$ and (B) $AuCl_4^-$ in an aqueous medium. The cross-sectional view corresponds to the plane along the dashed lines.

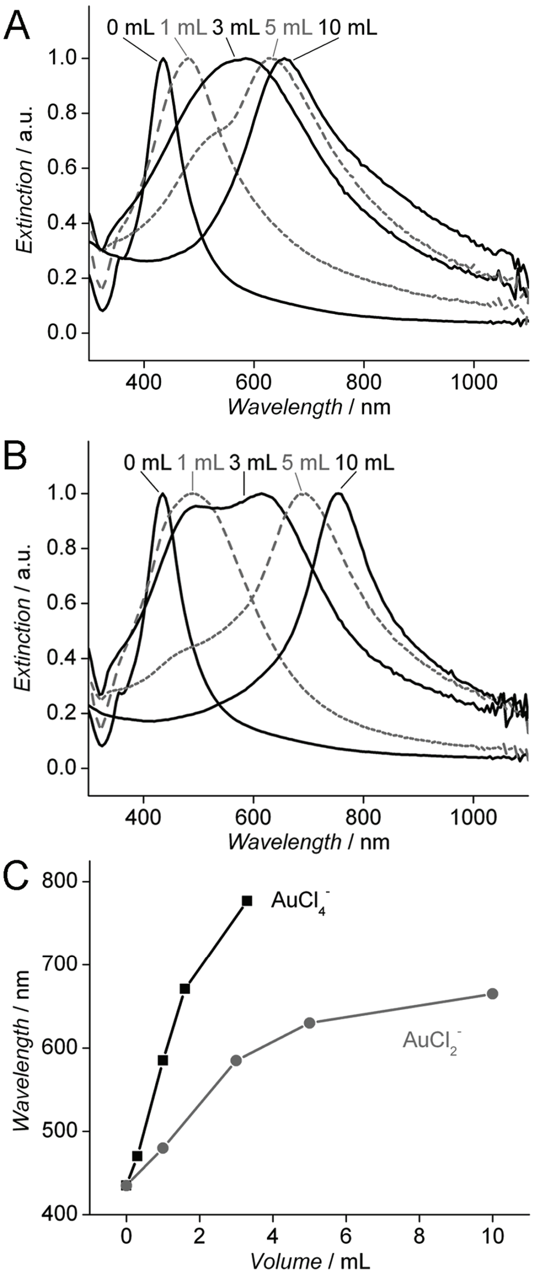

Figure 2.6 UV-vis spectra of the samples obtained by titrating Ag nanocubes with different volumes of 0.1 mM solution of: (A) $AuCl_2^-$ and (B) $AuCl_4^-$, respectively. (C) A plot of the peak position versus the volume of Au precursor, suggesting that $AuCl_2^-$ has a smaller shift (as seen by the gradual slope increase) compared to $AuCl_4^-$ for the same volume of Au precursor added to the reaction solution.

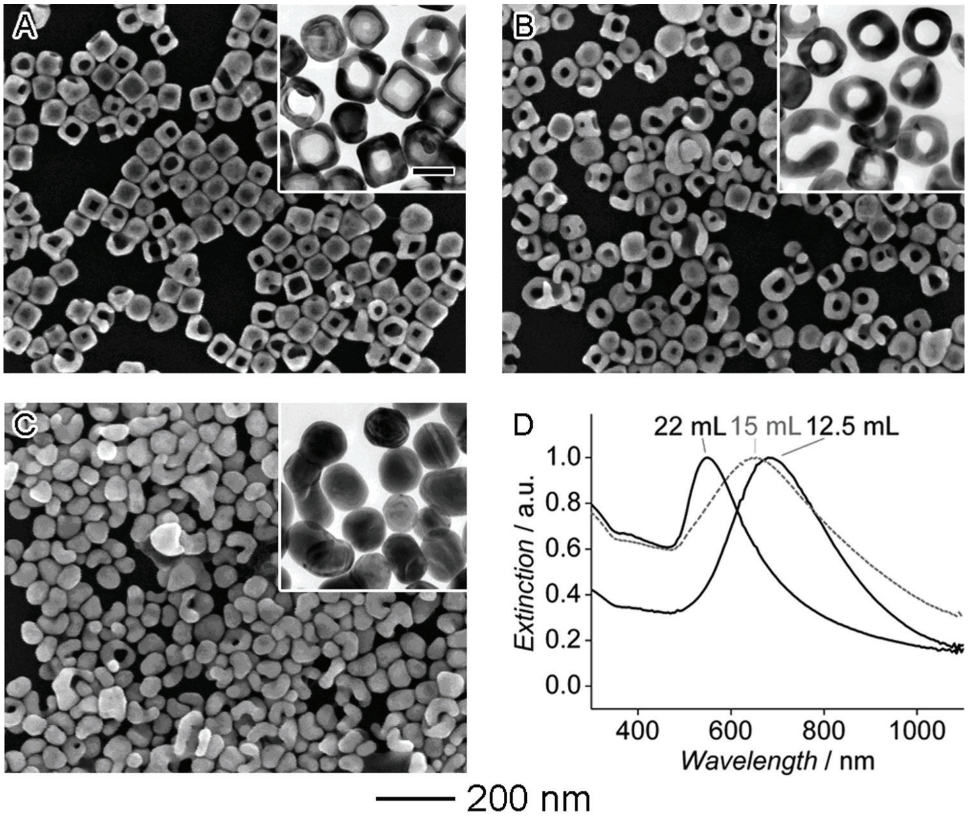

Figure 2.7 SEM and TEM (insets) images showing samples obtained in the later stages of the galvanic replacement reaction where Ag nanocubes were reacted with (A) 12.5 mL, (B) 15.0 mL and (C) 22.0 mL of 0.1 mM $AuCl_2^-$. The scale bar in the inset represents 50 nm and applies to all TEM images. The corresponding UV-vis spectra of the products are shown in (D).

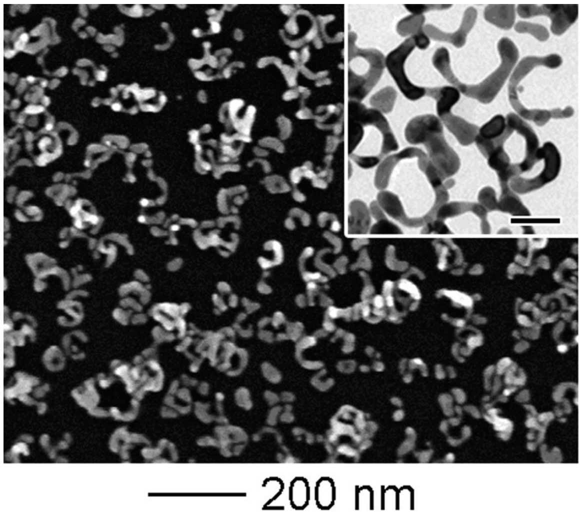

Figure 2.8 SEM and TEM (inset) images showing the product obtained in the late stage of the galvanic replacement reaction where Ag nanocubes were reacted with 5.0 mL of 0.1 mM $AuCl_4^-$. The scale bar in the inset represents 50 nm for TEM image.

Table 2.1 The weight percentage of Au by EDX in the Au/Ag nanostructures obtained by titrating Ag nanocubes with different amounts of 0.1 mM $AuCl_2^-$ or $AuCl_4^-$.

$AuCl_2^-$ [mL]	Au composition [Wt %]	$AuCl_4^-$ [mL]	Au composition [Wt %]
1.0	13	0.3	7
3.0	26	1.0	18
5.0	38	1.6	43
10.0	59	3.3	72
15.0	81	5.0	100
22.0	94		

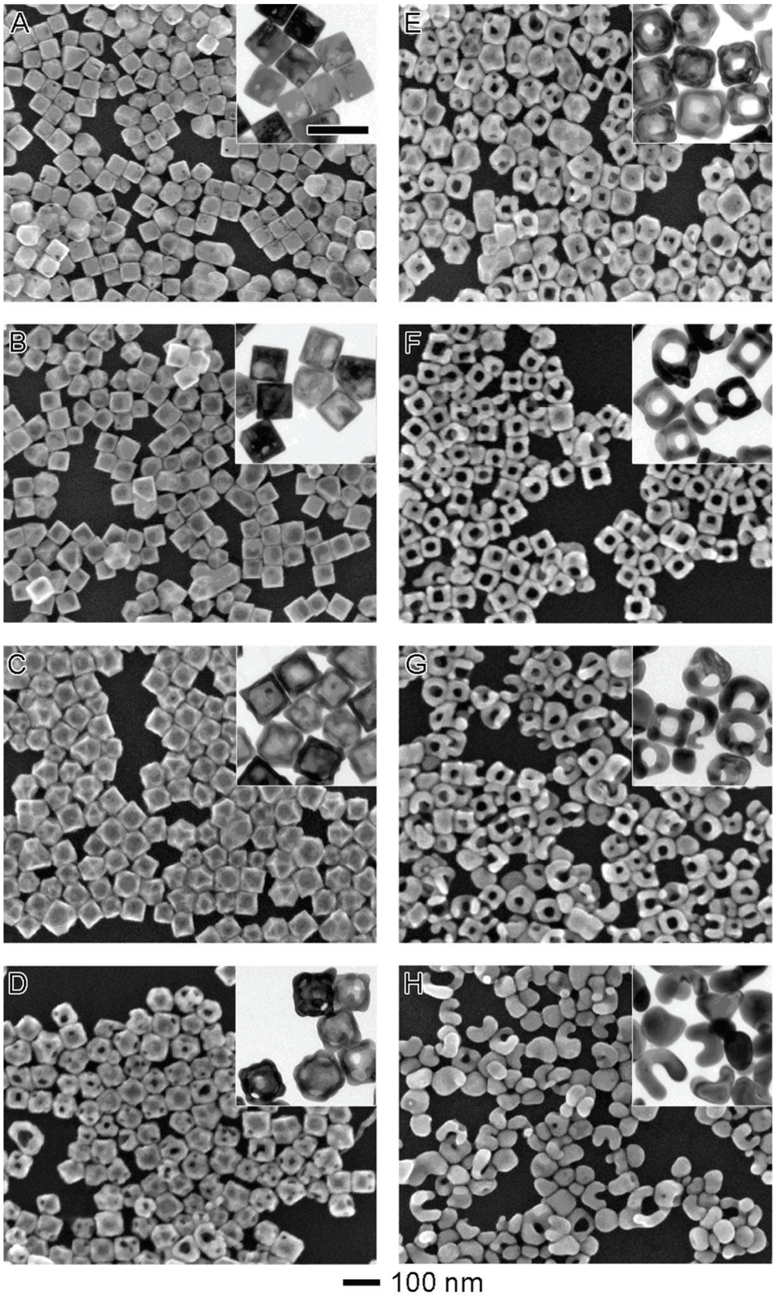

Figure 2.9 SEM and TEM (insets) images showing different stages of the galvanic replacement reaction where Ag nanocubes were titrated with different volumes of 0.2 mM AuCl in 1 mL increments ranging from (A) 1 mL to (H) 8 mL. The scale bar in the inset represents 100 nm and applies to all TEM images.

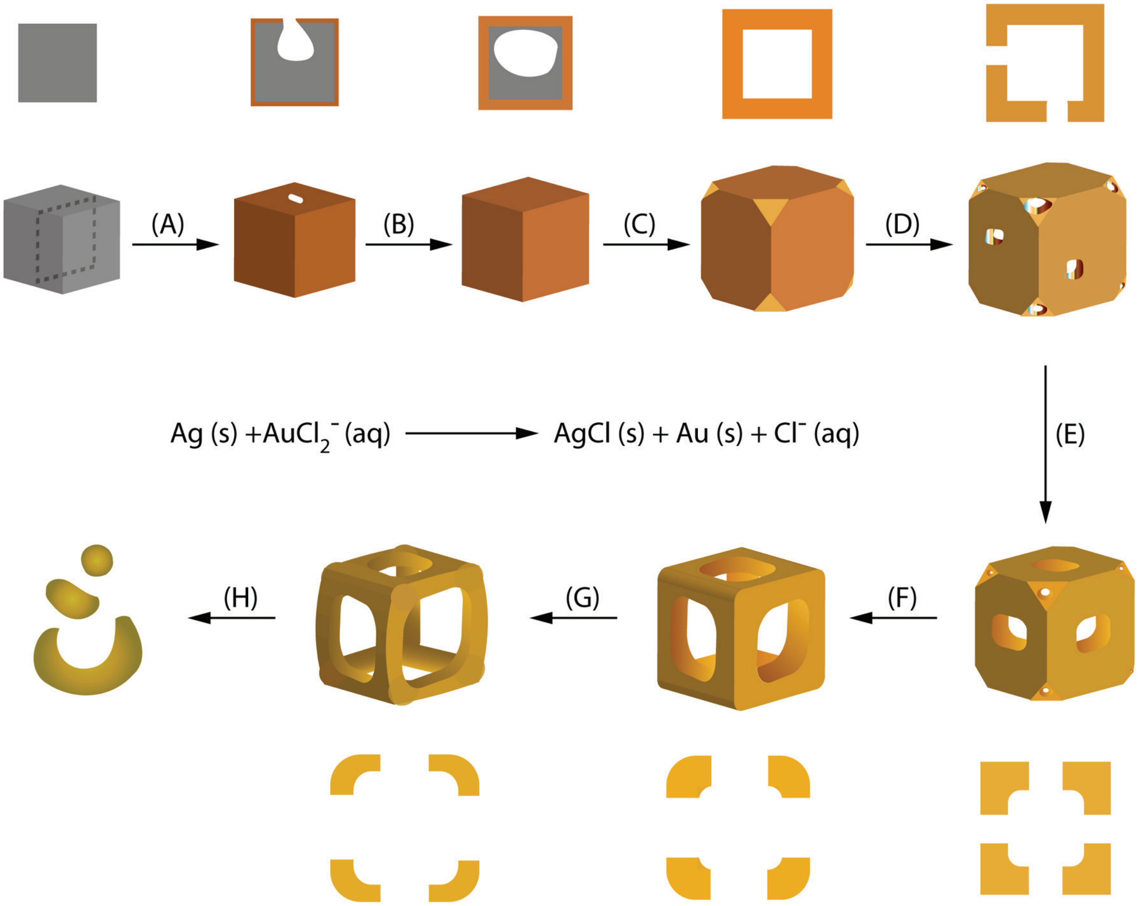

Figure 2.10 A schematic detailing the mechanism of the galvanic replacement reaction between Ag nanocubes and $AuCl_2^-$. The cross-sectional view corresponds to the plane along the dashed lines. The major steps of the reaction include the following: (A) formation of a pinhole at one of the side faces, (B) continuation of the replacement reaction resulting in a partially hollow structure, (C) development of a seamless nanobox with truncated corners, (D) generation of pores at the corners and side faces by dealloying process, (E, F) enlargement of pores at the side faces accompanied by shrinkage of pores at the corners via migration of atoms to the corners, (G) reduction of the ridge thickness and (H) fragmentation of the nanoframes.

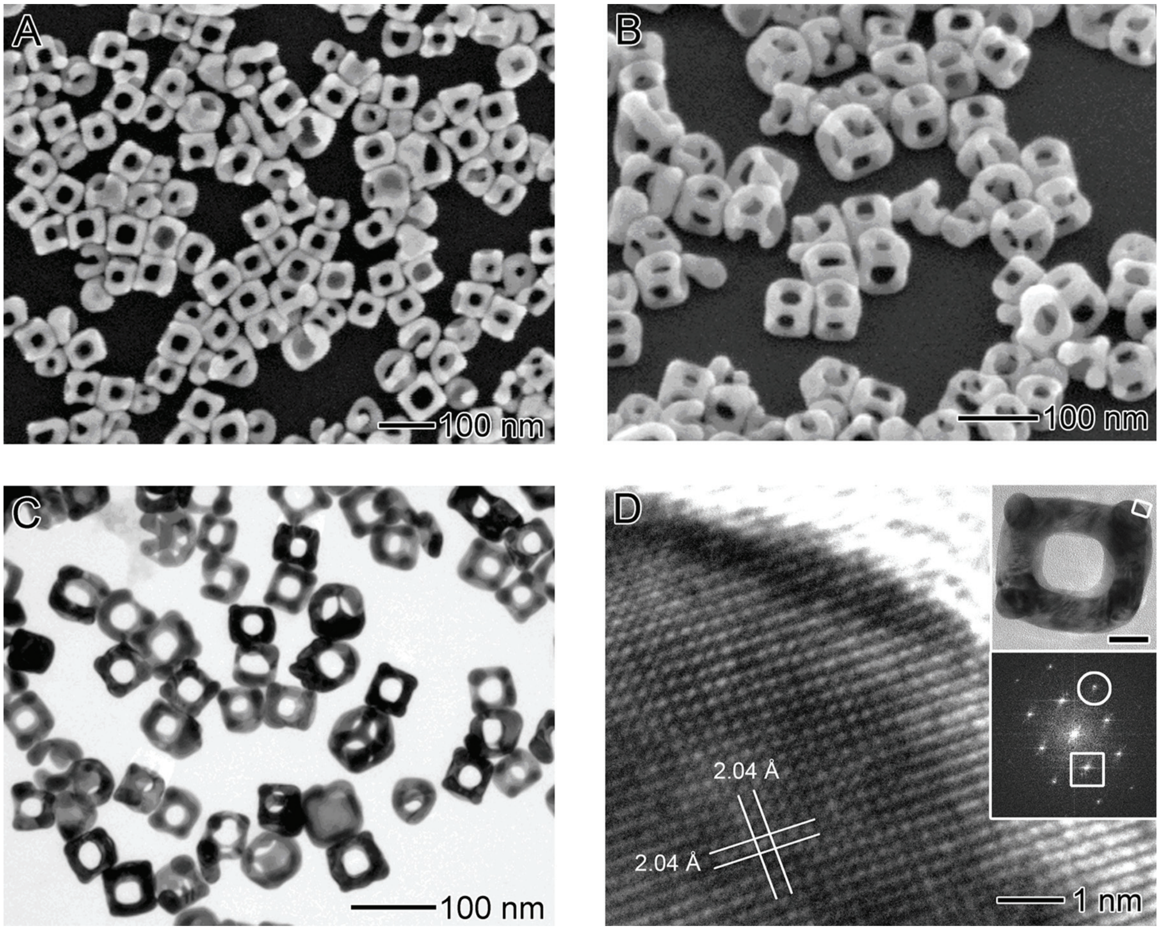

Figure 2.11 Electron microscopy characterization of the Au nanoframes prepared by the galvanic replacement reaction between 50 μl of Ag nanocubes and 6 mL of 0.2 mM $AuCl_2^-$: (A) SEM image of the Au nanoframes and (B) the same sample tilted by 45^o. (C) TEM image of the Au nanoframe. (D) High-resolution TEM image of a corner of the Au nanoframe taken from the region as labeled in the inset. The scale bar in the inset represents 20 nm. The lattice spacing of 2.04 Å can be indexed as the {200} planes of Au. In the FFT pattern, the spots circled and squared can be indexed to the {220} and {200} reflections, respectively.

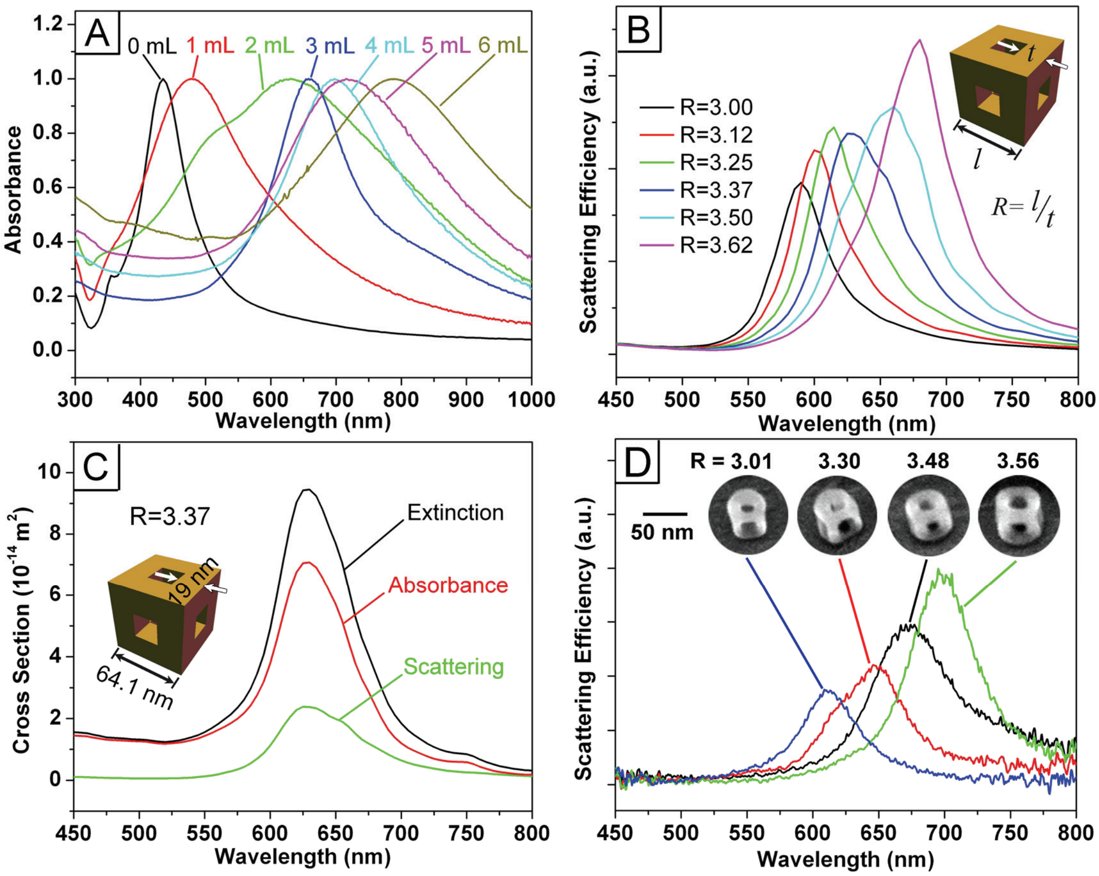

Figure 2.12 (A) UV-vis spectra taken from aqueous suspensions of the structures in Figure 1, A-F, which were synthesized by titrating Ag nanocubes with 1 mL to 6 mL of 0.1 mM $AuCl_2^-$. (B) DDA-calculated scattering spectra for nanoframes with an edge length of 57.0, 59.4, 61.8, 64.1, 66.5, and 68.9 nm, respectively, while the ridge thickness was kept at 19 nm, together with a composition of 89% Au and 11% Ag. The inset shows a drawing of the nanoframe used in these calculations, which has both sharp corners and edges. The plasmon resonance peak red-shifts with increasing the ratio (R) between the outer edge length (l) and the ridge thickness (t). (C) DDA-calculated extinction, scattering, and absorption spectra for a nanoframe with R=3.37. (D) Scattering spectra of individual Au nanoframes and the corresponding SEM images. For DDA calculation in (C) and (D), the nanoframes were filled and surrounded by water.

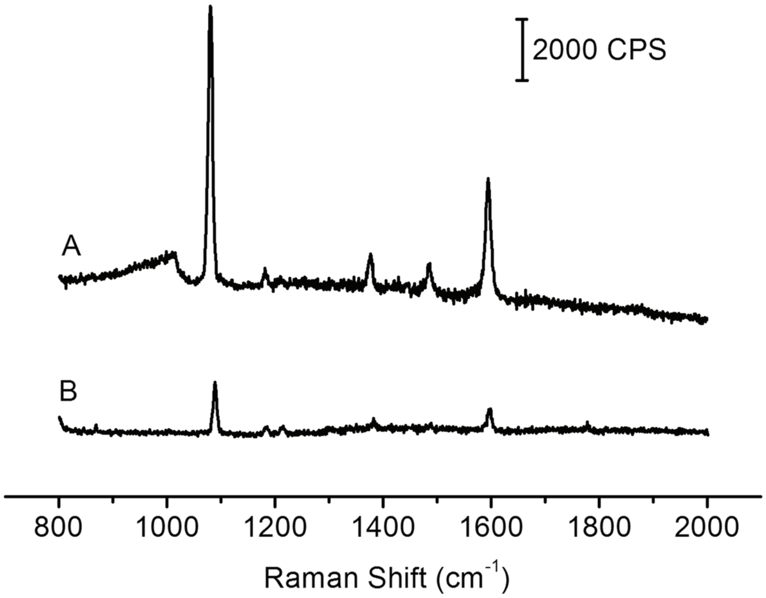

Figure 2.13 (A) The SERS spectrum taken from Au nanoframes whose surface had been derivatized with 4-MBT. (B) The ordinary Raman spectrum of 4-MBT (0.1 M in 12 M aqueous NaOH) taken for reference. The measurements were performed in a solution phase with an excitation wavelength of 785 nm.

2.7 Notes to Chapter 2

[1] Kim, S. W.; Kim, M.; Lee, W. Y.; Hyeon, T. *J. Am. Chem. Soc.* **2002**, *124*, 7642.

[2] Sun, Y.; Xia, Y. *Anal. Chem.* **2002**, *74*, 5297.

[3] Portney, N. G.; Ozkan, M. *Anal. Bioanal. Chem.* **2006**, *384*, 620.

[4] Cang, H.; Sun, T.; Li, Z.-Y.; Chen, J.; Wiley, B. J.; Xia, Y.; Li, X. *Opt. Lett.* **2005**, *30*, 3048.

[5] Chen, J.; Saeki, F.; Wiley, B. J.; Cang, H.; Cobb, M. J.; Li, Z.-Y.; Au, L.; Zhang, H.; Kimmey, M. B.; Li, X.; Xia, Y. *Nano Lett.* **2005**, *5*, 473.

[6] Chen, J.; Wiley, B. J.; Li, Z.-Y.; Campbell, D.; Saeki, F.; Cang, H.; Au, L.; Lee, J.; Li, X.; Xia, Y. *Adv. Mater.* **2005**, *17*, 2255.

[7] Au, L.; Zheng, D.; Zhou, F.; Li, Z.-Y.; Li, X.; Xia, Y. *ACS Nano 2008* **2008**, *2*, 1645.

[8] Chen, J.; Wang, D.; Xi, J.; Au, L.; Siekkinen, A.; Warsen, A.; Li, Z.-Y.; Zhang, H.; Xia, Y.; Li, X. *Nano Lett.* **2007**, *7*, 1318.

[9] Hirsch, L. R.; Gobin, A. M.; Lowery, A. R.; Tam, F.; Drezek, R. A.; Halas, N. J.; West, J. L. *Ann. Biomed. Eng.* **2006**, *34*, 15.

[10] Loo, C.; Lin, A.; Hirsch, L.; Lee, M. H.; Barton, J.; Halas, N.; West, J.; Drezek, R. *Technol. Cancer Res. Treat.* **2004**, *3*, 33.

[11] Chen, J.; McLellan, J. M.; Siekkinen, A.; Xiong, Y.; Li, Z.-Y.; Xia, Y. *J. Am. Chem. Soc.* **2006**, *128*, 14776.

[12] Sun, Y.; Mayers, B.; Xia, Y. *Adv. Mater.* **2003**, *15*, 641.

[13] Sun, Y.; Xia, Y. *Science* **2002**, *298*, 2176.

[14] Wiley, B. J.; Sun, Y.; Chen, J.; Cang, H.; Li, Z.-Y.; Li, X.; Xia, Y. *MRS Bull.* **2005**, *30*, 356.

[15] Yang, J.; Lee, J. Y.; Too, H. P. *J. Phys. Chem. B* **2005**, *109*, 19208.

[16] Yin, Y.; Erdonmez, C.; Aloni, S.; Alivisatos, A. P. *J. Am. Chem. Soc.* **2006**, *128*, 12671.

[17] Fievet, F.; Lagier, J. P.; Figlarz, M. *MRS Bull.* **1989**, *14*, 29.

[18] Skrabalak, S. E.; Wiley, B. J.; Kim, M.; Formo, E. V.; Xia, Y. *Nano Letters* **2008**, *8*, 2077.

[19] Sun, Y.; Mayers, B.; Herricks, T.; Xia, Y. *Nano Lett.* **2003**, *3*, 955.

[20] Wiley, B.; Herricks, T.; Sun, Y.; Xia, Y. *Nano Lett.* **2004**, *4*, 1733.

[21] Siekkinen, A. R.; McLellan, J. M.; Chen, J.; Xia, Y. *Chem. Phys. Lett.* **2006**, *432*, 491.

[22] Skrabalak, S. E.; Au, L.; Li, X.; Xia, Y. *Nat. Protoc.* **2007**, *2*, 2182.

[23] Lu, X.; Chen, J.; Skrabalak, S. E.; Xia, Y. *Proc. IMechE Part N: J. Nanoengineering and Nanosystems* **2007**, *221*.

[24] Chen, J.; Wiley, B. J.; McLellan, J.; Xiong, Y.; Li, Z.-Y.; Xia, Y. *Nano Lett.* **2005**, *5*, 2058.

[25] Sun, Y.; Xia, Y. *J. Am. Chem. Soc.* **2004**, *126*, 3892.

[26] Batzill, M.; Koel, B. E. *Surf. Sci.* **2004**, *553*, 50.

[27] Sun, Y.; Mayer, B.; Xia, Y. *Nano Lett.* **2002**, *2*, 481.

[28] Sun, Y.; Xia, Y. *Nano Lett.* **2003**, *3*, 1569.

[29] The reduction potentials reported are referenced to the SHE at 25 ^{o}C, 1 atm; however, the galvanic replacement reactions discussed here are performed at elevated temperatures under unique conditions, thus the absolute electrochemical potential difference could deviate from that reported. With the relatively high concentration of Cl^- present during the galvanic replacement, I suggest that the site of reaction AgCl nanocrystallites are formed that then dissolve into the bulk solvent at the elevated reaction temperature.

[30] Aizpurua, J.; Garnett, W. B.; Lee, J. R.; Abajo, F. J. G. d.; Brian, K. K.; Mallouk, T. *Phys. Rev. B* **2005**, *71*, 235420.

[31] Fuchs, R. *Phys. Rev. B* **1975**, *11*, 1732.

[32] Haes, A. J.; Haynes, C. L.; McFarland, A. D.; Schatz, G. C.; Van Duyne, R. P.; Zhou, S. *MRS Bull.* **2005**, *30*, 368.

[33] Kottmann, J. P.; Martin, O. J. F.; Smith, D. R.; Schultz, S. *Phys. Rev. B* **2001**, *64*, 235402.

[34] Kreibig, U.; Vollmer, M. Optical Properties of Metal Clusters; Springer: New York, 1995.

[35] Teperik, T. V.; Popov, V. V.; Abajo, F. J. G. d. *Phys. Rev. B* **2004**, *69*, 155402.

[36] Mie, G. *Ann. Phys.* **1908**, *25*, 377.

[37] Draine, B. T.; Flatau, P. J. *J. Opt. Soc. Am. A* **1994**, *11*, 1491.

[38] Wiley, B. J.; Im, S. H.; Li, Z.-Y.; McLellan, J. M.; Siekkinen, A.; Xia, Y. *J. Phys. Chem. B* **2006**, *110*, 15666.

[39] Qian, L.; Yang, X. *Colloids Surf. A* **2005**, *260*, 79.

[40] Dick, K.; Dhanasekaran, T.; Zhang, Z.; Meisel, D. *J. Am. Chem. Soc.* **2002**, *124*, 2312.

[41] Shi, H.; Zhang, L.; Cai, W. *J. Appl. Phys.* **2000**, *87*, 1572.

[42] Fan, H. J.; Knez, M.; Scholz, R.; Hesse, D.; Nielsch, K.; Zacharias, M.; Gosele, U. *Nano Lett.* **2007**, *7*, 993.

[43] Yin, Y.; Erdonmez, C.; Cabot, A.; Hughes, S.; Alivisatos, A. P. *Adv. Funct. Mater.* **2006**, *16*, 1389.

[44] Sieradzki, K. *J. Electrochem. Soc.* **1993**, *140*, 2868.

[45] Roosen, A. R.; Carter, W. C. *Physica A* **1998**, *261*, 232.

[46] Lu, X.; Au, L.; McLellan, J.; Li, Z.-Y.; Marquez, M.; Xia, Y. *Nano Lett.* **2007**, *7*, 1764.

[47] Au, L.; Lu, X.; Xia, Y. *Adv. Mater.* **2008**, *20*, 2517.

[48] Wang, Z. L. *J. Phys. Chem. B* **2000**, *104*, 1153.

[49] Wiley, B. J.; Sun, Y.; Mayers, B.; Xia, Y. *Chem. Eur. J.* **2005**, *11*, 454.

[50] Seo, D.; Yoo, C. I.; Park, J. C.; Park, S. M.; Ryu, S.; Song, H. *Angew. Chem. Int. Ed.* **2008**, *47*, 763.

[51] Tao, A.; Sinsermsuksakul, P.; Yang, P. *Angew. Chem. Int. Ed.* **2006**, *45*, 4597.

[52] McLellan, J. M.; Li, Z.-Y.; Siekkinen, A. R.; Xia, Y. *Nano Lett.* **2007**, *7*, 1013.

[53] McLellan, J. M.; Siekkinen, A.; Chen, J.; Xia, Y. *Chem. Phys. Lett.* **2006**, *247*, 122.

[54] Sherry, L. J.; Chang, S. H.; Schatz, G. C.; Van Duyne, R. P.; Wiley, B. J.; Xia, Y. *Nano Lett.* **2005**, *5*, 2034.

[55] Wiley, B. J.; Chen, Y.; McLellan, J. M.; Xiong, Y.; Li, Z.-Y.; Ginger, D. S.; Xia, Y. *Nano Lett.* **2007**, *7*, 1032.

[56] Chen, Y.; Munechika, K.; Ginger, D. S. *Nano Lett.* **2007**, *7*, 690.

[57] Chen, Y.; Munechika, K.; Ginger, D. S. *MRS Bull.* **2008**, *33*, 536.

[58] Munechika, K.; Smith, J. M.; Chen, Y.; Ginger, D. S. *J. Phys. Chem. C* **2007**, *111*, 18906.

[59] Chen, Y.; Munechika, K.; Plante, I. J.-L.; Munro, A. M.; Skrabalak, S.; Xia, Y.; Ginger, D. S. *Appl. Phys. Lett.* **2008**, *93*, 053106.

Chapter 3

Quantifying the Cellular Uptake of Antibody-Conjugated Gold Nanocages by Two-Photon Microscopy and Inductively Coupled Plasma Mass Spectrometry

3.1 Introduction

Gold nanocages have recently received increasing interests in biomedical imaging for modalities such as OCT and PAT. For imaging of cancerous tissue, it is important for the Au nanocages to have the capability to selectively target cancer cells rather than healthy cells. Antibodies are one class of commonly used ligands that can be easily conjugated to the surface of Au nanocages (and other types of nanostructures) for targeting the receptors typically overexpressed on the surface of cancer cells with high specificity. To this end, a quantitative understanding of the cellular uptake of antibody-conjugated Au nanocages *in vitro* can provide useful information for the design, synthesis, and surface modification of Au nanocages for cancer diagnosis and therapy.

There are a number of ways for analyzing the uptake of Au nanostructures by cells. One of the most commonly used methods is based on inductively coupled plasma mass spectrometry (ICP-MS), which can measure the concentration of Au ions down to the ppb level. This method, however, is rather time consuming as it requires digestion of the cells containing Au nanostructures with aqua regia. In contrast, an optical method will provide many advantages. As reported in literature, Au nanostructures can be excited optically, resulting in photoluminescence (PL) emission. This phenomenon was first observed by Mooradian *et al.* on smooth surfaces of Au, Cu, and their alloys.[1] The phenomenon arose from a recombination of the photo-excited electrons in the *s-p* conduction band with holes in the *d*-band. The efficiency of the resulting PL was extremely low, typically on the order of 10^{-10}. In a subsequent study, Boyd *et al.* compared the PL from smooth and rough surfaces of noble metals,[2] and it was found that the quantum yield of the PL was enhanced by several orders of magnitude on a rough surface due to the local-field enhancement in the proximity to the surface protrusions, which is analogous to surface-enhanced Raman scattering (SERS). Such enhancement is more pronounced for noble metals with feature sizes on the nanometer scale, especially when noble-metal nanoparticles were illuminated by a laser in resonance with the LSPR peak.[3-8] The PL can also be induced by two-photon excitation and the mechanism is the same as that induced by single-photon.[2,9] More recently, plasmon-resonant, two-photon-induced PL has been demonstrated with Au nanoparticles and further explored for three-dimensional cellular imaging.[10,11] When a Ti:sapphire laser is used, the Au nanostructures must have the LSPR peak tuned into the NIR region in order to satisfy the plasmon-resonant condition for strong PL generation. To this end, Wang *et. al.* has demonstrated that Au nanorods with a LSPR peak at 820 nm could produce PL signals 58 times that of the fluorescence signal from rhodamine molecules when excited at 830 nm using a two-photon scheme.[12]

Similar to Au nanorods, Au nanocages also have LSPR peaks tunable in the NIR region and are expected to emit strong PL when excited by two-photon excitation under the plasmon-resonant condition. In this work, I examined the two-photon induced PL of Au nanocages and their use as an imaging agent for two-photon microscopy. I then use two-photon microscopy to evaluate the uptake of anti-EGFR-conjugated Au nanocages by U87MGwtEGFR cells, a cancer cell line that is documented to overexpress epidermal growth factor receptor (EGFR) on the surface. The results were also correlated with ICP-MS analysis of Au content to provide a quantitative understanding of the *in vitro* and targeting and uptake processes.

3.2 Two-Photon Photoluminescence of Anti-EGFR Gold Nanocages

I began my studies with Au nanocages that had mean edge length of 50±3 nm and wall thickness of 5±1.2 nm. The monoclonal antibody, anti-EGFR, was conjugated to the surface of Au nanocages using a two-step protocol to generate anti-EGFR Au nanocages. In the first step, orthopyridyl disulfide-poly(ethylene glycol)-succinimidyl valerate (OPSS-PEG-SVA) was attached to the surface of Au nanocages via the gold-thiolate chemistry. In the second step, anti-EGFR was coupled to the Au-S-PEG-SVA through an amide bond. The number of anti-EGFR per nanocage could be controlled by adjusting the ratio of anti-EGFR to Au nanocages used for the reaction and quantified using the bicinchoninic acid (BCA) protein assay. Figure 3.1A shows a typical absorbance spectrum of the Au nanocages with a typical TEM image in the inset showing their geometry and structure. The LSPR peak of the Au nanocages in an aqueous suspension was initially tuned to 770 nm. Surface modification with anti-EGFR red-shifted the LSPR peak by 10 nm to 780 nm. When the anti-EGFR Au nanocages were transferred into the culture medium, the LSPR peak was further red-shifted to 795 nm due to a change in refractive index for the medium surrounding the nanocages. The LSPR peak of the anti-EGFR Au nanocages remains symmetric in a Lorentzian shape, indicating that the nanocages were well-dispersed in the culture medium. Figure 3.1B shows the PL excitation and emission spectrum from the anti-EGFR Au nanocages as measured using the two-photon microscope. Similar to PL of Au nanorods,[12,13] the Au nanocages exhibited a broad PL band extending from 400 to 700 nm when excited by a two-photon laser with a peak output at 800 nm due to a strong interaction between the localized surface plasmon and the electric field generated by the laser. In a control experiment, no PL was observed for an aqueous solution that contained no Au nanocages.

3.3 Receptor-Mediated Endocytosis of Anti-EGFR Gold Nanocages

The PL from Au nanocages provides a simple and convenient way to evaluate their *in vitro* targeting capability using two-photon microscopy. In a typical study, U87MGwtEGFR cells were incubated with anti-EGFR Au nanocages for 3 h at 37 ^{o}C in the presence of FM4-64, a membrane and endosome marker. The PL from the Au nanocages was recorded in green color (Figure 3.2A) while the fluorescence from the FM4-64 dye exhibited a red color (Figure 3.2B). Figure 3.2C shows superimposition of these two images, clearly indicating that the anti-EGFR Au nanocages and FM4-64 dye molecules were co-localized. This observation implies that the anti-EGFR Au nanocages were not only attached to the surface of the tumor cells, but also had been internalized into the cells. In contrast, tumor cells incubated with the PEGylated Au nanocages under the same condition showed little PL (Figure 3.2, D-F), suggesting that very few PEGylated Au nanocages were attached to or internalized into the tumor cells after 3 h incubation. When the incubation time was extended to 24 h, the PL intensity originating from the Au nanocages was dramatically enhanced for both anti-EGFR (Figure 3.3A) and PEGylated Au nanocages (Figure 3.3B). Note that all the images were taken with the same setting for PL, so their intensities could be directly compared.

I also determined the Au content in the cells by ICP-MS analysis. The concentration of Au was then converted into the number of nanocages using the following equations and plotted in Figure 3.3C. For a Au nanocage of *L* in outer edge length and *l* in inner edge length, the number of Au atoms (*n*) containing in each nanocage was determined by Eq. 3.1, where *a* refers to the lattice constant of a unit cell of Au (*a* = 4.0786 Å) and there are four Au atoms per unit cell. The number of Au nanocages (*N*) can then be calculated by Eq. 3.2, where *M* refers to the measured number of Au atoms from ICP-MS analysis.

$$n = \frac{4(L^3 - l^3)}{a^3} \qquad (3.1)$$

$$N = \frac{M}{n} \qquad (3.2)$$

At t=3 h, the total number of nanocages uptaken by the cells was 57±10 and 408±40, while it increased to 190±31 and 826±50, respectively, at t=24 h for PEGylated and anti-EGFR Au nanocages. The overall uptake of the anti-EGFR Au nanocages by the cells was approximately five times higher than the PEGylated Au nanocages. The extraordinary uptake of anti-EGFR Au nanocages could be attributed to the endocytosis mediated by interactions between the anti-EGFR on the surface of nanocage and their receptors over-expressed on the U87MGwtEGFR cells. The affinity of anti-EGFR to its antigen is on the order of 0.1-1 nM.[14,15] To further confirm the involvement of receptor-mediated endocytosis (RME) for the anti-EGFR Au nanocages, I treated the cells with excess anti-EGFR to saturate the receptors on the cell surface before incubating them with the anti-EGFR Au nanocages. When the receptors on the cell surface were saturated by the excess anti-EGFR,[14,15] no PL was observed for the cells after incubation with the anti-EGFR Au nanocages (Figure 3.3D). However, the FM4-64 dye was still uptaken by the anti-EGFR pre-treated cells and to give a red color (Figure 3.3E). These results indicate that the anti-EGFR Au nanocages entered the cells as a result of the interactions between anti-EGFR and their receptor. The FM4-64 dye molecules were uptaken via a different internalization pathway that did not work for the Au nanocages. In addition, temperature may affect the binding rate of the ligands as well as the lateral mobility of the ligand-receptor complex, resulting in inhibition of the RME process.[16] When the cells were incubated with anti-EGFR Au nanocages and the dye at 4 °C, neither the nanocage nor dye was uptaken by the cells (Figure 3.3F).

The RME process involves the binding of antibodies on the nanoparticles to receptors on the cell surface and internalization of the nanoparticles into the cell when the cell membrane folds inwards. Eventually, the receptors may be recycled back to the membrane surface after delivery of the antibody-conjugated nanoparticles into the cell.

Differentiation of the internalized nanocages from the surface-bound ones could play an important role in understanding the RME mechanism and thus enhancing the delivery efficacy of antibody-conjugated nanocages.[17] After incubation with anti-EGFR Au nanocages, I treated the cells with 20 mM sodium acetate in PBS (pH=3.0) buffer. Lowing pH is one of the most commonly used treatments for breaking the antigen-antibody complexes.[18] In this case, an acidic solution can be used to selectively remove the anti-EGFR Au nanocages bound to the cell surface.[15] Figure 3.4 shows the representative confocal images of the cells before and after the treatment of with an acidic solution. The cells were incubated with anti-EGFR Au nanocages for 1 h at 37 °C and the excess, free nanocages were removed by washing with PBS three times. As it can be seen in Figure 3.4, A and B, both the membrane and the interior of each individual cell were lighted up with green luminescence color due to the presence of Au nanocages. After the treatment with an acidic solution, the PL from Au nanocages was mainly located in the interiors of the cells (Figure 3.4, C and D), indicating that most of the surface-bound nanocages had been selectively removed.

3.4 Time Dependent Study of the Cellular Uptake of Anti-EGFR Gold Nanocages

I then studied the cellular uptake of anti-EGFR Au nanocages as a function of incubation time. The U87MGwtEGFR cells were incubated with anti-EGFR nanocages for different periods of time in the culture medium. After incubation and removal of the free anti-EGFR nanocages, for each well, the cells were rinsed with an acidic solution and the surface-bound nanocages in the washing solution was collected in a conical tube. The cells were then detached from the culture well with trypsin and collected in another conical tube. The washing solution and the trypsinized cells were digested in aqua regia and analyzed for Au concentration by ICP-MS. Figure 3.5 shows plots of surface-bound number (N_s), internalized number (N_i), and total number (N_t) of nanocages per cell as a function of incubation time. Note that N_s and N_i were derived from the Au concentration measured by ICP-MS and N_t is the sum of N_s and N_i. The N_s initially increased, reached a peak around 1 h, and then fell. The internalization of Au nanocages shows two different profiles: N_i went up sharply in the first 30 min, and the uptake rate fell off, but still remained to increase up to 24 h during the course of study. This finding is different from the previous studies with spherical Au nanoparticles uptaken via clathrin-mediated endocytosis where the N_t was significantly increased for the first hour, and then the rate of uptake reached a plateau in 4-7 hours.[19] The discrepancy might be due to the difference in surface receptor availability, ligand-receptor interaction, the equilibrium condition between the surrounding and interior of the cell.[20]

3.5 The Number of Antibodies Per Nanocage and its Influence on Cellular Uptake of Anti-EGFR Gold Nanocages

I also investigated the cellular uptake of Au nanocages with different numbers of antibodies on the surface of the nanocage. In this case, the Au nanocages were reacted with anti-EGFR at different molar ratio to yield samples with 16, 28, and 144 anti-EGFR per nanocage (i.e., anti-EGFR$_{16}$ Au nanocages, anti-EGFR$_{28}$ Au nanocages, and anti-

EGFR_{144} Au nanocages), respectively. Figure 3.6 shows the PL images of the cells after incubation with these anti-EGFR Au nanocages for 3 h, and their corresponding superimpositions with confocal images taken from FM4-64 staining. The co-localization of the PL from the Au nanocages and the fluorescence from the FM4-64 confirmed that the nanocages were bound to and internalized into the cells. The PL intensity from the cells after treatment with nanocages was enhanced as the number of anti-EGFR per nanocages was increased. This observation was in agreement with the ICP-MS data shown in Figure 3.7, indicating that the number of Au nanocages per cell increased as the number of anti-EGFR per nanocage increased.

When a Au nanocage comes into contact with the surface of a cell, only the anti-EGFR on one of the six faces could initially interact with the cell surface because of the cubic shape of the nanocage. In other words, two anti-EGFRs could bind to the cell surface for anti-EGFR_{15} Au nanocage, while five anti-EGFRs could interact with the cell surface for anti-EGFR_{30} nanocage. Doubling the number of antibodies can improve multivalent interaction between nanocages and the receptors, resulting in increase in the number of uptake by 1.5 times. However, when the number of antibodies was increased by another 5 times to 24 anti-EGFRs on each side face of the nanocage, the number of internalized nanocages only went up by another 1.3 times. The reduction in uptake could be attributed to the local depletion of the available receptors as driven by the ligand-receptor binding in the RME process because each anti-EGFR_{144} nanocage would require 5 and 10 times more receptors as compared to anti-EGFR_{16} and anti-EGFR_{44} nanocages, respectively.[21]

3.6 Size Dependent Study of the Cellular Uptake of Anti-EGFR Gold Nanocages

Finally, I compared the internalization of Au nanocages with different sizes. For receptor-mediated endocytosis, many variables affect the uptake rate of particles, including driving force of ligand-receptor binding and the receptor mobility on the cell surface. Gao *et. al.* developed a model involving a wrapping process for the membrane and predicted that the optimum diameter in the range of 54-60 nm would be wrapped the most efficient for spherical particles.[21] From the thermodynamic point of view, Zhang *et. al.* also predicted that spherical particles of 50-60 nm in diameter would have a maximum number of uptake into the cell in the range of 500 to 5000.[20]

I chose Au nanocages with an edge length of 35±4, 50±3, and 90±8 nm (i.e. Au-35, Au-50, and Au-90) for this study. All the Au nanocages were conjugated with a maximum number of anti-EGFR per nanocage. By converting the edge length of cubic nanocage into its effective diameter (d_e) with the assumption of equal volume, d_e equals 44, 62, and 112 nm for Au-35, Au-50, and Au-90 nanocage, respectively. Figure 3.8 shows the number of Au nanocages per cell analyzed by ICP-MS after the cells were incubated with the Au nanocages with different edge lengths. The number of internalized Au nanocages was 605±33, 334±30, 170±5, for Au-35, Au-50, and Au-90 nanocages, respectively. Note that there was a small number for the surface-bound Au-90 nanocages because the acid solution might not be able to remove the surface-bound nanocages effectively due to the strong binding between the multiple anti-EGFRs on each nanocage to the receptors. The Au-35 nanocages with d_e of 44 nm were internalized into the cells with the maximum number. This finding is supported by the theoretical calculation and previous experimental results that the optimum size for receptor-mediated internalization is 40-50 nm in diameter for spherical particles.

3.7 Summary

I have evaluated the uptake of anti-EGFR Au nanocages by U87MGwtEGFR cancer cells using two-photon confocal microscopy. Gold nanocages with LSPR peak tuned to 780 nm exhibited a broad luminescence band extending from 400 to 700 nm when excited in a two-photon scheme with a Ti:sapphire laser centered at 800 nm. Confocal optical images clearly indicate that the anti-EGFR Au nanocages were both attached to the cell surface and internalized into the cell through receptor-mediated endocytosis. The qualitative PL results agree well with the quantitative analysis of Au by ICP-MS. My time-dependent study shows that there was a peaked uptake at 24 h, with a total of ~800 Au nanocages per cell. The multivalent effect could increase the uptake of the nanocages although it might compromise the availability of receptors if too many ligands were present per nanocage. The optimum size of nanocage for internalization is ~35 nm in edge length. The two-photon PL from Au nanocages can be used to quickly screen their interactions with cells, as well as evaluate their distribution in tissue for *ex vivo* and *in vivo* studies.

3.8 Experimental Section

Synthesis and characterization of Au nanocages. Gold nanocages with mean edge lengths of 35, 50, and 90 nm were synthesized through galvanic replacement by reacting chloroauric acid and Ag nanocubes of 30, 45, and 70 nm in edge length, respectively. The detailed procedure has been reported in our previous publications.[22,23] The LSPR peaks of these nanocages were tuned to 770 nm by controlling the amount of chloroauric acid added into the suspensions of Ag nanocubes. The absorbance spectra were recorded using a Cary 50 UV-vis spectrophotometer (Varian, Palo Alto, CA). TEM samples were prepared by dropping an aqueous suspension of the nanocages onto a carbon-coated copper grid (Ted Pella, Redding, CA) and allowing it to dry under ambient conditions. The sample was continuously rinsed with water for one hour to remove residual PVP and then dried before TEM characterization. TEM images were collected on a Tecnai G2 Spirit Twin microscope (FEI, Hillsboro, OR) operated at 120 kV. The Au and Ag concentrations of the nanocage suspensions were measured using an Agilent 7500ce ICP-MS (Agilent Technologies, Santa Clara, CA). From the ICP-MS data and TEM images, the molar concentrations of the nanocages can be calculated. For size comparison, Au nanocages with mean edge lengths of 35, 50, and 90 nm were prepared and studied.

Bionconjugation of Au nanocages. Gold nanocages were functionalized with monoclonal antibodies using a two-step protocol.[24] First, 1 mL of a 1 mM aqueous solution of OPSS-PEG-SVA (MW≈5000, Laysan Bio, Arab, AL) was mixed with a suspension of Au nanocages 25 pM in concentration. The suspension of nanocages was then agitated for 4 h at room temperature in the dark. After incubation, the solution was centrifuged at 10,000 rpm for 20 min, and the supernatant was removed. The nanocages were washed once with PBS. In the second step, 1 mL of PBS containing 10-120 μg of anti-EGFR (clone LA1, Millipore, Temecula, CA) was added to the nanocages and incubated at 4 °C for 12 h under agitation. The nanocages were centrifuged and the supernatant containing free anti-EGFR was kept for BCA assay. The anti-EGFR Au nanocages were re-dispersed in PBS and stored at 4 °C until future use. For PEGylated sample, the same amount of Au nanocages was mixed with 1 mL of 1 mM mPEG-SH (MW≈5000, Nektar Therapeutics, San Carlos, CA). The solution was agitated for 4 h in the dark at room temperature. Afterwards, the solution was centrifuged, washed once with PBS, and re-dispersed in 1 mL of PBS. The Au and Ag contents were analyzed using ICP-MS to determine the final concentration of the functionalized nanocages.

Quantifying the number of anti-EGFR per nanocage. The supernatant collected previously containing unbound anti-EGFR was analyzed using the BCA assay (Thermo Scientific, Rockford, IL). This assay uses a bicinchoninic acid formulation for the colorimetric detection and quantification of protein. The procedures were carried out as provided by the manufacturer's instructions. The number of antibodies per nanocage (N_a) was calculated as follows: N_a = the total number of antibodies added – the number of antibodies in the supernatant. Incubation with 10, 35, and 120 μg of anti-EGFR yielded roughly 16, 28, 144 anti-EGFR per Au nanocage, respectively.

Cell culture. The U87MGwtEGFR cell line was obtained from Prof. Michael J. Welch in the Department of Radiology at Washington University in St. Louis. The cells were cultured in the Dulbecco's modified eagle medium with high glucose (DMEM, HG, Gibco, Carlsbad, CA) supplemented with 10% fetal bovine serum (FBS, Gibco) and 500 mg/L of Geneticin (G418, Gibco) under 5% CO_2 at 37 ^{o}C. The U87MGwtEGFR cells were reseeded 24 h before experiments in 6-well plate at a population of 5×10^5 cells per well. The medium was changed immediately prior to incubation with Au nanocages. Nanocages (at a final concentration of 0.02 nM) were added into each well and incubated with gentle rotation for a given amount of time as noted in the text. Dye FM4-64 (Molecular Probe Inc., Eugene, OR), a widely used marker for staining membrane and endosomes, was incubated with the cells simultaneously at a final concentration of 5 μg/mL. After incubation, the cells were rinsed three times with PBS to remove any unbound Au nanocages. For the removal of surface-bound nanocages, the cells were subsequently washed for 10 min at 4 ^{o}C with 2 mL of a PBS solution containing 20 mM sodium acetate with pH adjusted to 3.0 with HCl. They were then rinsed again with the 2 mL PBS solution containing sodium acetate. The washings were collected and saved for ICP-MS analysis. For blocking experiments, anti-EGFR with a final concentration of 100 nM was added to the cells 1 h prior to the addition of nanocages. For experiments at a low temperature, the cells were refrigerated at 4 ^{o}C for 10 min prior to and then for 1 h under gentle agitation after the addition of nanocages. The cells were only incubated for 1 h at 4 ^{o}C because longer incubation time resulted in cells lifting off from the growth vessel during the washing process.

Two-photon confocal imaging. After washing off the unbound Au nanocages, the cells were covered with a coverslip (#1.5, Corning, Corning, NY) and sealed with vacuum grease. They were kept in the dark and imaged within the next few hours. The imaging was performed using an upright Zeiss LSM 510 NLO system (Carl Zeiss) coupled with a Ti:sapphire laser (Chameleon, Coherent), a green helium-neon (543 nm) laser, and a 63× water immersion objective (Carl Zeiss). The Ti:sapphire laser was operated in a mode-locked configuration at a wavelength overlapping with the LSPR peak of the nanocages, generating sub-200 fs pulse trains at 90 MHz. The PL data were collected using BP500-550IR. The fluorescence dye was excited at 543 nm, and the emission was collected with BP650-700IR. Multi-track mode was used to collect both luminescence and fluorescence images. For comparison, all the confocal images were taken at the same conditions. The PL emission and excitation spectra of anti-EGFR Au nanocages in PBS were collected using the same microscope. The suspension of nanocages was drawn into a microcapillary tube (Vitrocom, 5002-050) for imaging. For the emission spectrum, the sample was irradiated at 800 nm and the fluorescent images were simultaneously collected at different wavelengths (380-720 nm, 10 nm intervals). For the excitation spectrum, the solution was excited at different wavelengths (720-950 nm, 10 nm intervals), and the corresponding fluorescent images, also known as lambda stack, were simultaneously collected using a BP500-550IR filter. The emission and excitation spectra were derived from the intensity of the fluorescent signal and from the collected images using the Zeiss LSM software.

Sample preparation for ICP-MS analysis. For the analysis of surface-bound Au nanocages, the PBS-acetate washings that were previously collected were digested in 5% aqua regia. For internalized nanocages, the cells which were washed with the PBS-acetate solution were removed from the bottom of the well using 2 mL of trypsin, followed by two rinses with 1 mL aliquots of media. This solution was collected and then digested in 5% aqua regia. All solutions were centrifuged at 3,000 rpm for 5 min to remove any cellular debris which may clog the instrument. The Au and Ag contents of the solution were then analyzed using ICP-MS.

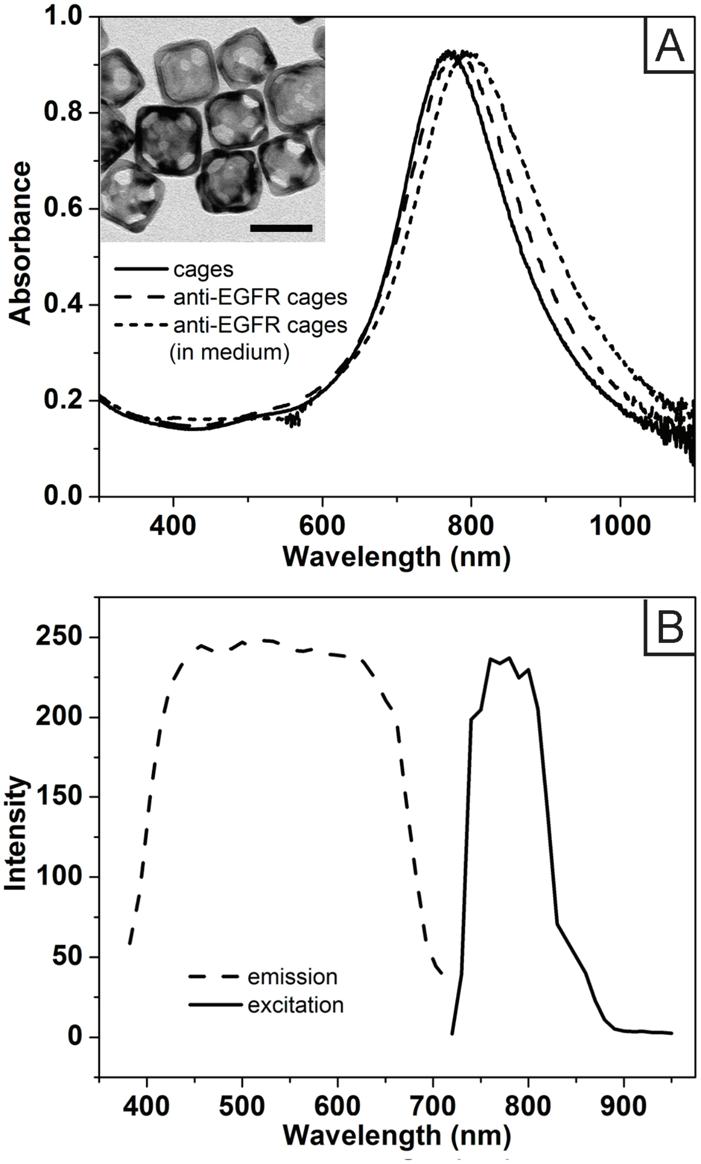

Figure 3.1 (A) UV-vis-NIR absorbance spectra of the Au nanocages (solid line) in PBS, anti-EGFR-conjugated Au nanocages (dashed line) in PBS, and anti-EGFR Au nanocages (dotted line) in the culture medium. The inset shows a TEM image of the corresponding Au nanocages with a mean edge length of 50 ± 3 nm and wall thickness of 5 ± 1.2 nm. The scale bar in the inset represents 50 nm. (B) PL excitation (solid line) and emission spectra (dashed line) of the Au nanocages.

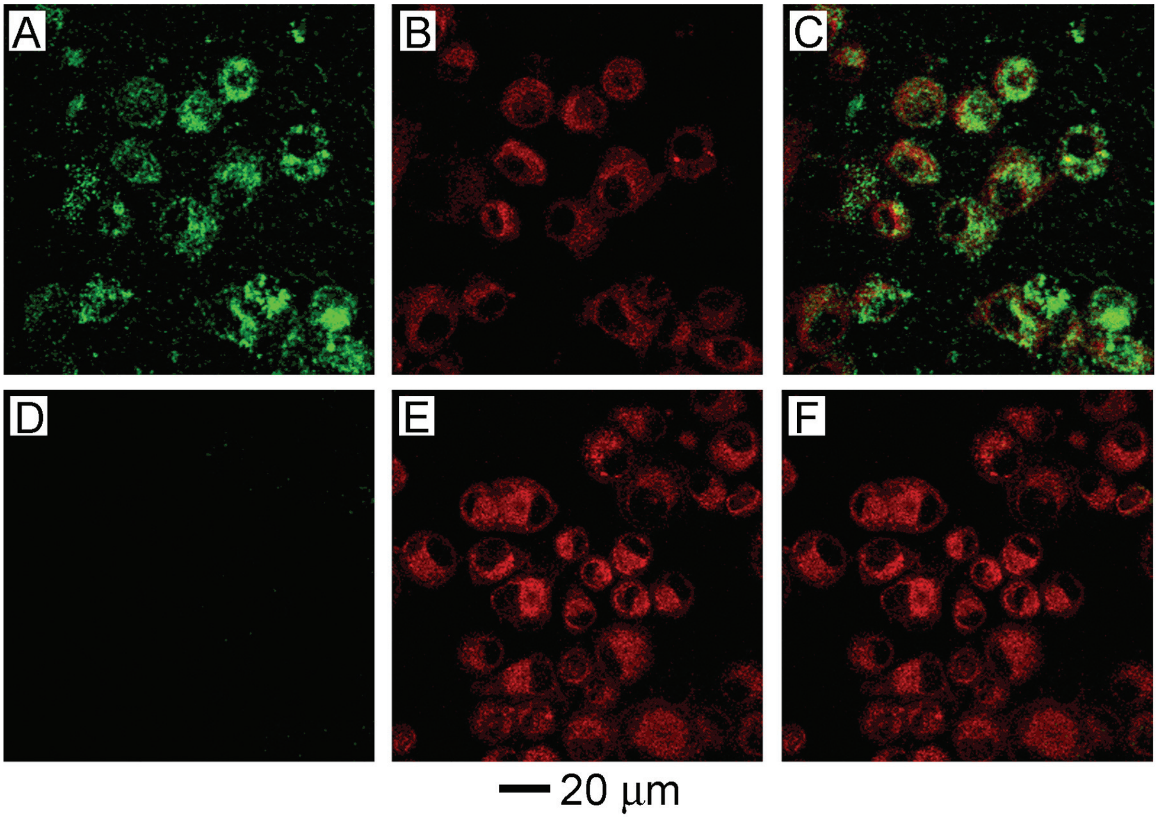

Figure 3.2 (A-C) Confocal images of the U87MGwtEGFR cells after incubation for 3 h with 0.02 nM of anti-EGFR Au nanocages and 5 μg/mL of FM4-64 dye: (A) photoluminescence from Au nanocages; (B) red fluorescence from FM4-64; and (C) superimposition of (A) and (B). (D-E) Confocal images of the U87MGwtEGFR cells after incubation with PEGylated Au nanocages and FM4-64 dye for 3 h: (D) luminescence from Au nanocages; (E) red fluorescence from FM4-64; and (F) superimposition of (D) and (E). The scale bar applies to all images.

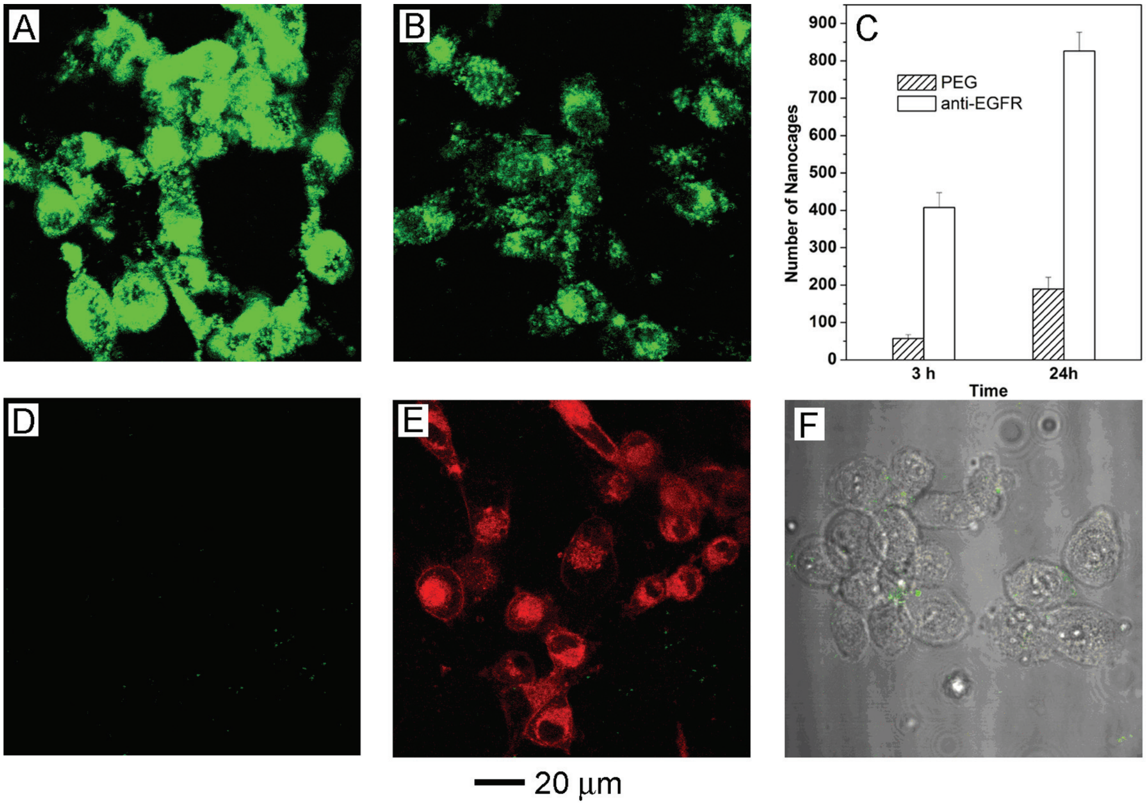

Figure 3.3 Confocal images of the U87MGwtEGFR cells after they had been incubated for 24 h with (A) anti-EGFR and (B) PEGylated Au nanocages, respectively. (C) Quantitative ICP-MS plots showing the number of anti-EGFR and PEGylated Au nanocages per cell for incubation time of 3 h and 24 h, respectively. (D-F) Confocal images of the cells that were treated with excess anti-EGFR (100 nM) for 1 h prior to incubation with anti-EGFR nanocages and FM4-64 for 3 h: (D) photoluminescence from Au nanocages and (E) superimposition of the luminescence from Au nanocages and red fluorescence from FM4-64, indicating that the EGF receptors were effectively saturated and there was essentially no uptake for the nanocages. (F) Superimposition of the luminescence from Au nanocages, red fluorescence from FM4-6, and phase contrast image of the cells that were incubated with anti-EGFR nanocages and FM4-64 dye at 4 °C for 1 h.

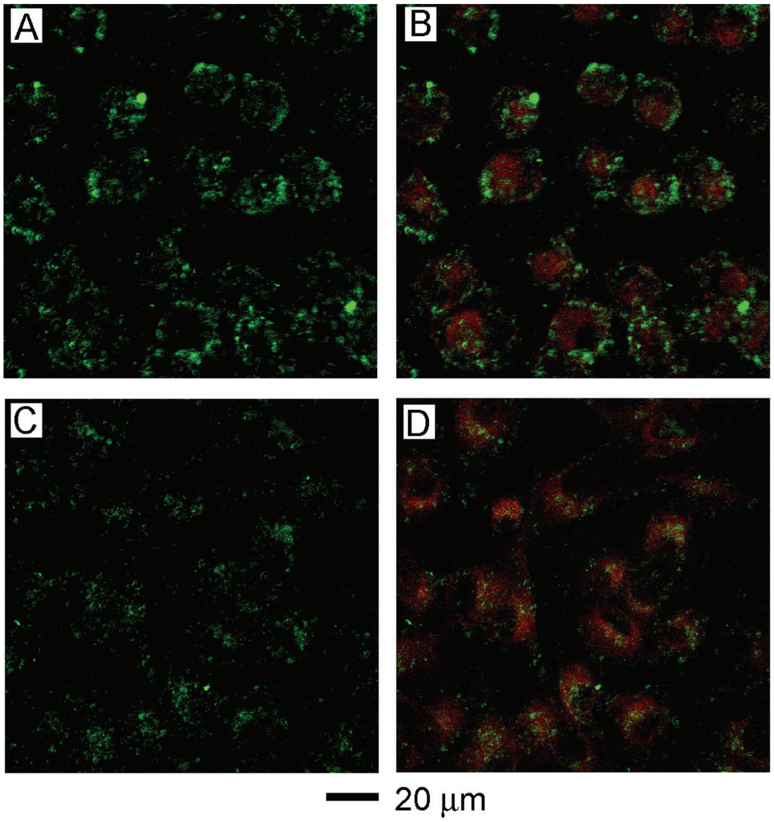

Figure 3.4 Confocal images of the U87MGwtEGFR cells after incubating with anti-EGFR Au nanocages and FM4-64 for 1 h: (A) luminescence from Au nanocages and (B) superimposition of the luminescence from Au nanocages and red fluorescence from FM4-64. Confocal images of the cells incubated with anti-EGFR Au nanocages and FM4-64 for 1 h, followed by extensive washing with PBS (pH=3.0) containing 20 mM sodium acetate for the removal of surface-bound nanocages: (C) luminescence from Au nanocages and (D) superimposition of the luminescence from Au nanocages and red fluorescence from FM4-64.

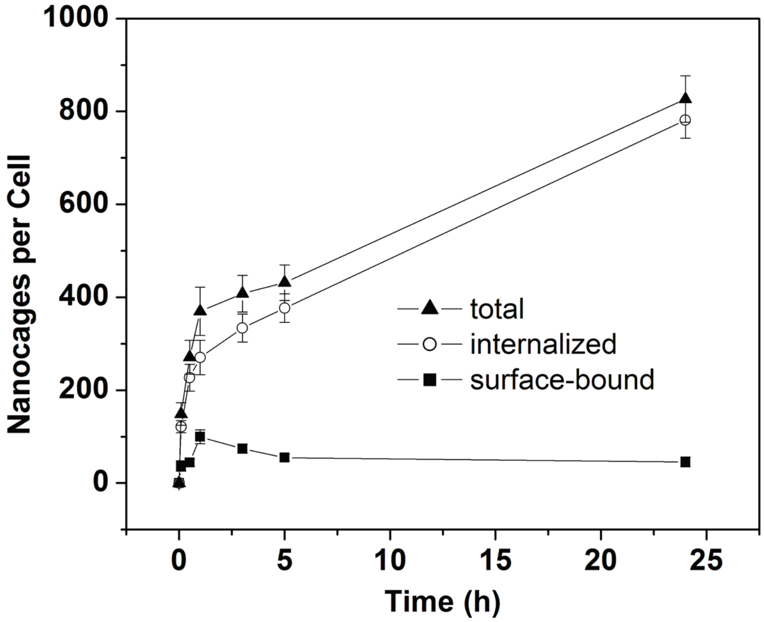

Figure 3.5 Quantitative ICP-MS analysis of the number of anti-EGFR Au nanocages per cell for samples prepared with different incubation times. The surface-bound Au nanocages were selectively detached from the cell surface during the treatment with PBS (pH=3.0) containing 20 mM of sodium acetate.

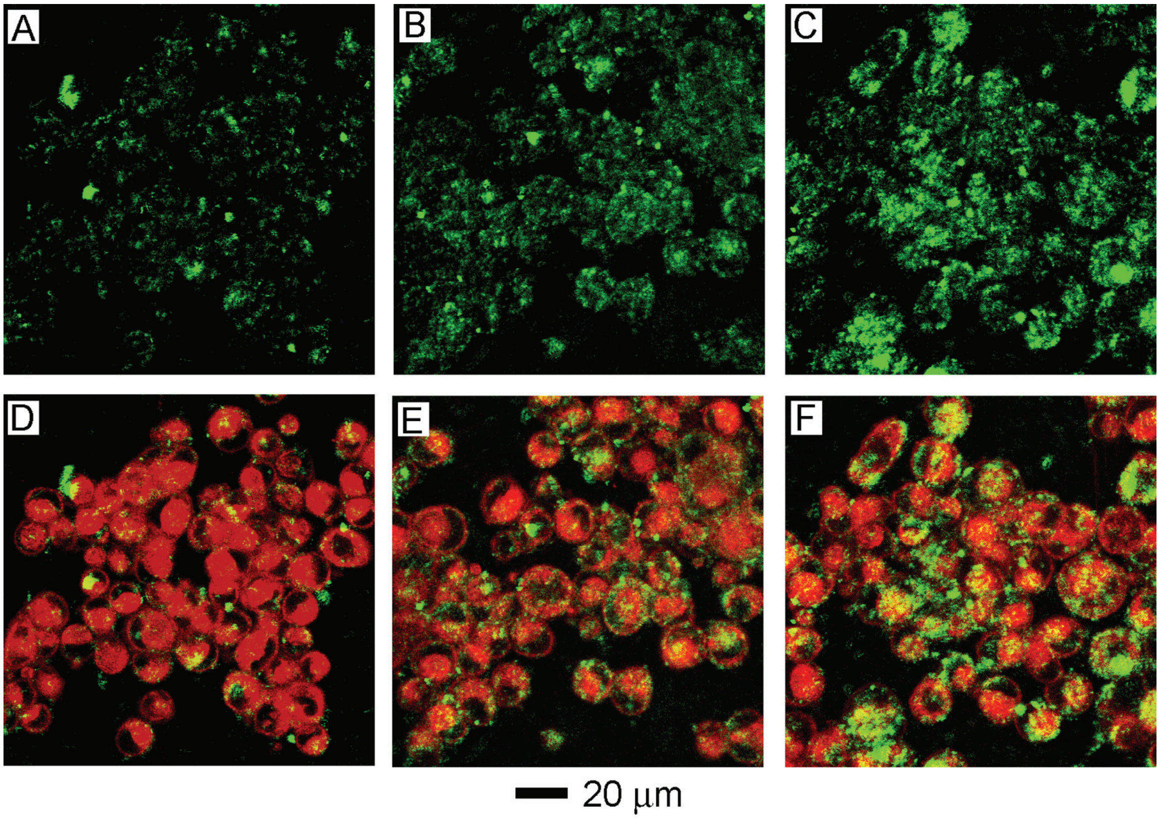

Figure 3.6 Confocal images of the U87MGwtEGFR cells incubated for 3 h with 5 μg/mL of FM4-64 dye and 0.02 nM of Au nanocages having different numbers of anti-EGFR on the surface. (A-C) Photoluminescence from Au nanocages with roughly (A) 16, (B) 28, and (C) 144 anti-EGFR on the surface of each nanocage, and (D-F) superimpositions of the luminescence from Au nanocages and red fluorescence from FM4-64.

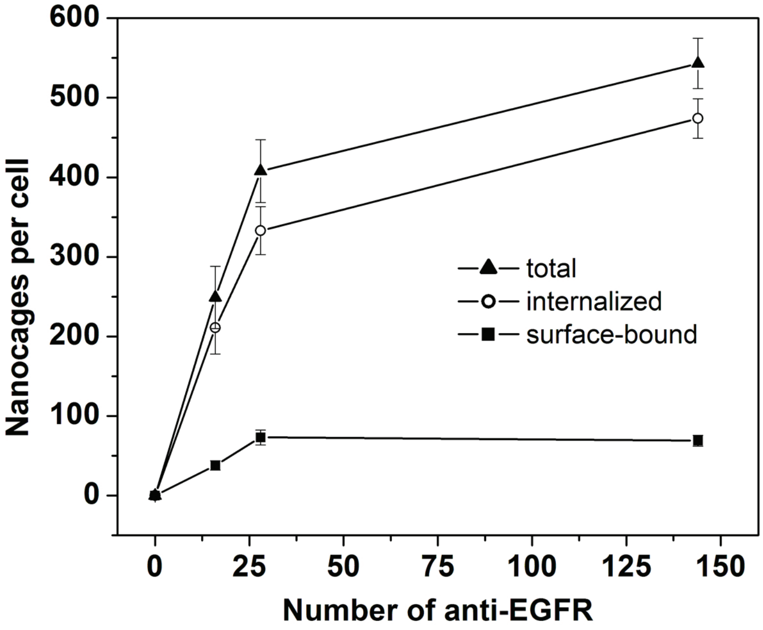

Figure 3.7 Quantitative ICP-MS analysis of the number of surface-bound (■), internalized (○), and total (▲) anti-EGFR Au nanocages per cell when incubated for 3 h with 0.02 nM of nanocages having different numbers of anti-EGFR on the surface: 16, 28, and 144. The surface-bound Au nanocages had been selectively detached from the cell surface by treating with PBS (pH=3.0) containing 20 mM of sodium acetate.

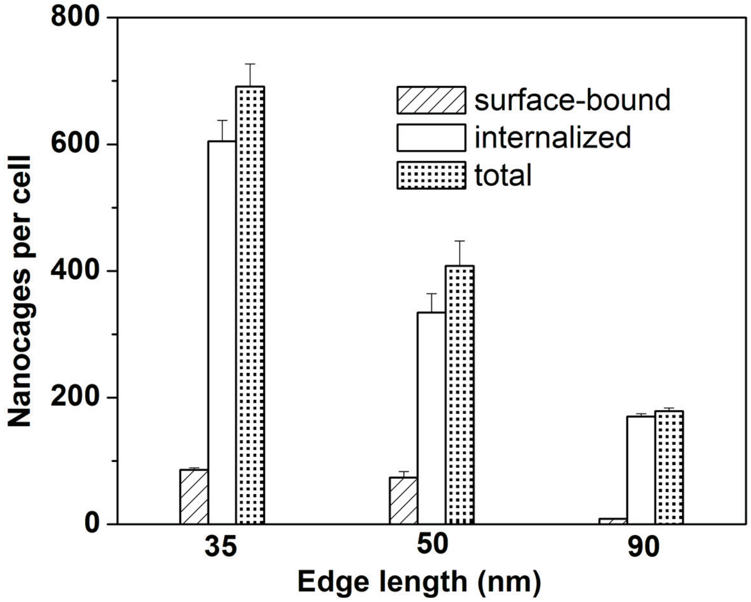

Figure 3.8 Quantitative ICP-MS analysis of the number of anti-EGFR Au nanocages per cell when incubated for 3 h with 0.02 nM of nanocages with different mean edge lengths: 35, 50, and 90 nm. The surface-bound Au nanocages had been detached from the cell surface by treating with PBS (pH=3.0) containing 20 mM of sodium acetate.

3.9 Notes to Chapter 3

[1] Mooradian, A. *Phys. Rev. Lett.* **1969**, *22*, 185.

[2] Boyd, G. T.; Yu, Z. H.; Shen, Y. R. *Phys. Rev. B* **1986**, *33*, 7923.

[3] Wilcoxon, J. P.; Martin, J. E.; Parsapour, F.; Wiedenman, B.; Kelley, D. F. *J. Chem. Phys.* **1998**, *108*, 9137.

[4] Mohamed, M. B.; Volkov, V.; Link, S.; El-Sayed, M. A. *Chem. Phys. Lett.* **2000**, *317*, 517.

[5] Peyser, L. A.; Lee, T.-H.; Dickson, R. M. *J. Phys. Chem. B* **2002**, *106*, 7725.

[6] Bouhelier, A.; Beversluis, M. R.; Novotny, L. *Appl. Phys. Lett.* **2003**, *83*, 5041.

[7] Drachev, V. P.; Khaliullin, E. N.; Kim, W.; Alzoubi, F.; Rautian, S. G.; Safonov, V. P.; Armstrong, R. L.; Shalaev, V. M. *Phys. Rev. B* **2004**, *69*, 035318.

[8] Imura, K.; Nagahara, T.; Okamoto, H. *J. Am. Chem. Soc.* **2004**, *126*, 12730.

[9] Farrer, R. A.; Butterfield, F. L.; Chen, V. W.; Fourkas, J. T. *Nano Lett.* **2005**, *5*, 1139.

[10] Yelin, D.; Oron, D.; Thiberge, S.; Moses, E.; Silberberg, Y. *Opt. Express* **2003**, *11*, 1385.

[11] Nagesha, D.; Laevsky, G. S.; Lampton, P.; Banyal, R.; Warner, C.; DiMarzio, C.; Sridhar, S. *Int. J. Nanomedicine* **2007**, *2*, 813.

[12] Wang, H.; Huff, T. B.; Zweifel, D. A.; He, W.; Low, P. S.; Wei, A.; Cheng, J.-X. *P. Natl. Acad. Sci. USA* **2005**, *102*, 15752.

[13] Black, K. C.; Kirkpatrick, N. D.; Troutman, T. S.; Xu, L.; Vagner, J.; Gillies, R. J.; Barton, J.; Utzinger, U.; Romanowski, M. *Mol. Imaging* **2008**, *7*, 50.

[14] Delves, P. J.; Martin, S. J.; Burton, D. R.; Roitt, I. M. Roitt's Essential Immunology; Wiley-Blackwell: Malden, 2006.

[15] Eiblmaier, M.; Meyer, L. A.; Watson, M. A.; Fracasso, P. M.; Pike, L. J.; Anderson, C. J. *J. Nucl. Med.* **2008**, *49*, 1472.

[16] Pastan, I.; Willingham, M. C. Endocytosis; Plenum Press: New York, 1985.

[17] Ruoslahti, E. *Scand. J. Immunol.* **1976**, *5*, 3.

[18] Cho, E. C.; Xie, J.; Wurm, P. A.; Xia, Y. *Nano Lett.* **2009**, *9*, 1080.

[19] Chithrani, B. D.; Ghazani, A. A.; Chan, W. C. W. *Nano Lett.* **2006**, *6*, 662.

[20] Zhang, K.; Fang, H.; Chen, Z.; Taylor, J.-S. A.; Wooley, K. L. *Bioconjugate Chemistry* **2008**, *19*.

[21] Gao, H.; Shi, W.; Freund, L. B. *P. Natl. Acad. Sci. USA* **2005**, *102*, 9469.

[22] Sun, Y.; Xia, Y. *J. Am. Chem. Soc.* **2004**, *126*, 3892.

[23] Skrabalak, S. E.; Au, L.; Li, X.; Xia, Y. *Nat. Protoc.* **2007**, *2*, 2182.

[24] Chen, J.; Wiley, B.; Li, Z. Y.; Campbell, D.; Saeki, F.; Cang, H.; Au, L.; Lee, J.; Li, X.; Xia, Y. *Adv. Mater.* **2005**, *17*, 2255.

Chapter 4

Quantifying the Photothermal Effect of Antibody-Conjugated Gold Nanocages Targeted to SK-BR-3 Breast Cancer Cells

4.1 Introduction

The strong optical absorption of some Au nanostructures makes them attractive as photothermal agents for cancer therapy.[4] Unlike the conventional methods for cancer treatment (e.g., surgical removal, radiotherapy, and chemotherapy), photothermal treatment – in which light is converted to heat *in vivo* to kill cells via hyperthermia – holds promise as a noninvasive technique for the selective destruction of cancer cells with minimal injury to the surrounding healthy cells. Several types of Au nanostructures with strong optical absorption in the near-infrared region have been developed; among these are Au nanoshells supported on silica cores,[5,6] Au nanorods,[7-9] and Au nanocages.[10,11] Calculations based upon the DDA method indicate that the nanoshells tend to scatter light predominately, whereas both the nanorods and nanocages are stronger light absorbers.[1] Although the ratio of light absorption to scattering may vary slightly with the dimensions of the nanostructures, these calculations suggest that the nanocages and nanorods are more effective optical absorbers than nanoshells. The large absorption cross-section of the Au nanocages was recently confirmed experimentally by

OCT measurements and found to be approximately five orders of magnitude greater than that of the conventional organic dyes.[12] Finally, I have found that the absorption peaks of nanocages can be more conveniently and precisely fine-tuned than those of other Au nanostructures, potentially allowing for their large scale production for practical applications.[13,14]

The photothermal effects of the various Au nanostructures were recently demonstrated, and all were shown qualitatively to be able to destroy targeted cancer cells upon irradiation with a near-infrared laser.[15-19] However, there are no quantitative studies of the cellular damage in which parameters such as the number of immobilized Au nanostructures per cell, the waiting time after irradiation, and the duration of laser exposure were considered. In this work, I quantify the photothermal effect of anti-EGFR Au nanocages (i.e., nanocages conjugated with anti-EGFR monoclonal antibodies) targeted to SK-BR-3 cells – a well-characterized breast cancer cell line that overexpresses the EGFR – by employing flow cytometry. In doing so, I was able to better elucidate the interactions between the nanocages, cells, and laser, which will contribute to the optimization of treatment parameters for future *in vivo* experiments.

4.2 Preparation and Characterization of the Anti-EGFR Gold Nanocages

For this study, Au nanocages of 65±7 nm in edge length and 7.5±1 nm in wall thickness were synthesized through a galvanic replacement reaction using silver nanocubes (~54 nm in edge length) as the sacrificial template and chloroauric acid,

$HAuCl_4$, as the precursor to Au.[10-14] Figure 4.1A shows SEM and TEM images of the Au nanocages. These Au nanocages were shown to contain 37% residual Ag in the form of an alloy with Au by EDX analysis. If necessary, the residual Ag can be selectively removed through a dealloying process with the use of $Fe(NO_3)_3$ or NH_4OH.[20] Using the DDA method, the absorption, scattering, and extinction spectra were calculated for a Au nanocage with an edge length of 65 nm, a wall thickness of 7.5 nm, and a pore diameter of 20 nm at the corners. The results are shown in Figure 4.1B. The C_{abs} and C_{sca} were found to be peaked at 6.16×10^{-14} m^2 and 2.02×10^{-14} m^2, respectively, with a C_{abs}/C_{sca} ratio of ~3.0. The measured extinction spectrum of the nanocages shown in the inset is consistent with the calculation. The discrepancy in peak width can be ascribed to the variations in edge length, wall thickness, the degree of corner truncation, and the porosity for the Au nanocages contained in a bulk sample. The Au nanocages were then conjugated to anti-EGFR antibodies using a two-step procedure which was described in Chapter 3.[21,22] After conjugation, the extinction peak of these anti-EGFR Au nanocages slightly red-shifted from 800 nm to 805 nm, which was expected due to the small change of refractive index on the surface of the nanocages. It is worth pointing out that this small shift can be taken into account during the preparation of the pristine Au nanocages to ensure that there will be an exact overlap between the resonance peak of the anti-EGFR Au nanocages and the central wavelength of the laser. Recently, Au nanocages with similar optical properties were demonstrated by us to be effective agents for the *in vitro* photothermal destruction of cancer cells.[15] Thus, it was reasoned that these anti-EGFR Au nanocages would work well for the quantitative studies described here.

4.3 Quantification of the Targeting Process *in vitro*

Previously, the targeting selectivity of my bioconjugation protocol was demonstrated by immunofluorescence imaging and SEM.[21,22] However, no information with regards to the number of nanocages attached to the cell surface was obtained. This information is important as it can tell us the amount of nanocages necessary to induce a photothermal therapeutic effect and allow for better comparisons between my nanocages and other nanostructures. Thus, in the first part of this study, I sought to quantify the average number of Au nanocages attached per cell. In addition to Au nanocages, Au nanospheres of 40 nm in diameter were used as a reference to validate the experimental procedure due to their well-defined size, shape, and composition. As a first approximation, SEM images were taken of the SK-BR-3 cells treated with anti-EGFR Au nanocages or nanospheres. The number of nanostructures observed in a randomly selected 2 μm by 1.5 μm portion of the cell was counted from multiple samples. Based upon the number of nanostructures measured in that section and the dimensions of the cell as revealed by SEM imaging, the surface coverage was estimated to be approximately 200-2000 Au nanostructures per cell. This broad range could be attributed to the inhomogeneous distribution of receptors on the cell surface.[23] Figures 4.2A and B show SEM images of individual cells that had been targeted with the anti-EGFR Au nanospheres and nanocages, respectively. Interestingly, TEM imaging of a microtomed sample revealed that the Au nanocages were not solely immobilized on the surface of the cell. As Figure 4.2C shows, some of them were internalized into the cell, although none appeared to enter the nucleus. The EGFR antibodies have been reported to trigger endocytosis, but the exact mechanism for nanocage uptake has yet to be elucidated.[24,25]

While electron microscopy allows us to see where the anti-EGFR Au nanostructures are located (on the surface *vs.* inside) and roughly at what coverage, this technique is of rather limited power when dealing with large numbers of cells. To more accurately quantify the targeting efficiency of the anti-EGFR Au nanostructures, I decided to use flow cytometry coupled with ICP-MS. With this approach, the amount of Au contained in a specific number of cells can be determined. Then from the geometric parameters of the nanostructures, the number of nanostructures per cell can be calculated. Specifically, the amount of Au can be easily determined by analyzing the sample with ICP-MS, while the number of cells in the sample can be easily quantified by spiking it with a known amount of Sphero Ultra Rainbow beads, followed by flow cytometry counting. Figure 4.2D shows a typical flow cytometry graph where forward scatter (x-axis) and right angle scatter (y-axis) can be used to differentiate the size difference between the beads and the cells. Then the number of cells can be quantified using FCS Express software to gate the populations of both cells and beads. For the standard *in vitro* targeting procedure described in the experimental section, I found that there were approximately 460±130 Au nanospheres per cell and roughly 400±90 Au nanocages per cell; both numbers fall within the initial estimates from SEM images. In future *in vivo* studies, this information should allow for the administration of anti-EGFR Au nanocages in proper dosages to induce a photothermal effect for tumors of known sizes.

4.4 Quantification of the Photothermal Treatment Process *in vitro*

The photothermal treatment with the anti-EGFR Au nanocages was implemented *in vitro* with SK-BR-3 cells. The central wavelength of the radiation was 805 nm with a bandwidth of 54 nm so there was an optimal overlap with the absorption peak of the anti-EGFR Au nanocages. Yet, good spectral overlap between the light source and the light absorbing nanostructure will not alone ensure a good therapeutic effect. Factors such as time of cellular response to laser irradiation, laser power density, and time of laser exposure could also influence the efficiency of the photothermal effect. Thus, I systematically varied these parameters and quantified the amount of cellular death under each condition using flow cytometry coupled with propidium iodide (PI) staining.

PI is a popular nuclear or chromosomal counterstain in multicolor fluorescence techniques and is commonly used in flow cytometry to differentiate cell cycles. When PI binds to DNA by intercalating between the bases, it fluoresces about 20-30 folds stronger than unbound PI.[26] Since PI is not permeable to live cells, it works well as a marker to quantify the number of dying or dead cells in a sample. In addition, it only requires a short incubation time (<15 min) and can generate well-separated populations of live and dead/dying cells. In a typical flow cytometry measurement, one can use PI fluorescent and forward scattering signals to quantify the cellular death caused by the photothermal effect.

Figure 4.3A shows the experimental setup, where cells in the center of a well (6.38 mm in diameter; 96-well plate) were irradiated with the Ti:Sapphire laser with a spot size of 2 mm. The SK-BR-3 cells are adherent, hence their position is fixed on the surface of the well. It should be pointed out that the laser only irradiated 9.8% of the cells in each well (note cells are not drawn to the scale). I also tried to use smaller wells (e.g., 3.7 mm in diameter; 384-well plate), but were found to increase the experimental error so the 96-well plate was used. In one study, the treated cells were harvested at various times after irradiation to investigate when cells start to respond to the photothermal treatment. In Figure 4.3B, the cells were irradiated at a laser power density of 4.77 W/cm^2 for 5 min. After that, the cells were returned to a 37 ^{o}C incubator for a specific duration of time before the percentage of cellular damage was quantified. Cells targeted with the anti-EGFR Au nanocages (in black) exhibited more cellular damage at early harvest times. The cellular damage decreased at harvest times greater than 3 h after laser exposure, which could possibly be attributed to: *i*) the cells untouched by the laser proliferated during their course in the incubator, resulting in a dilution of the destructed cells, and/or *ii*) some of the damaged cells recovered from the photothermal effect. Cells irradiated under the same conditions but without the anti-EGFR Au nanocages (in red) exhibited no significant response during the given time. A small, unavoidable percentage of cellular death was observed, probably due to the pipetting and handling of cells during sample preparation. The results of this study indicate that the cells respond immediately to the photothermal treatment and should be harvested within 3 h after irradiation to better reflect the treatment. Harvest times shorter than 1 h after laser irradiation are not feasible due to the time required to prepare the sample for flow cytometry.

Figures 4.3C and D show the flow cytometry graphs of the cells with and without targeting by the anti-EGFR Au nanocages, respectively, at a harvest time of 3 h after laser irradiation. Forward scatter is plotted on the x-axis and PI emission signal is plotted on the y-axis. The flow cytometry graphs were sectioned into four quadrants. Quadrant-I, exhibiting a large forward scattering and low PI signal, represents the population of live cells. Since the live cells have intact cell membranes, PI could not stain their DNAs. Quadrant-II, displaying large forward scattering and high PI signal, corresponds to the population of dying cells. The membranes of these cells had been compromised so PI could penetrate and then hybridize with their DNAs. The population of dead cells, or stained DNAs, exhibits a high PI and small forward scattering signal as shown in quadrant-III. These are free DNAs, no longer enclosed within a membrane. Quadrant-IV reveals a population with small forward scattering and low PI signal that could be attributed to instrumental background signals and debris from ruptured cells. The population in quadrant-IV does not representatively correspond to live or damaged cells, so the percentage of cellular damage was normalized to the population in quadrants I, II and III. A higher population of damage was observed when the cells were targeted with the anti-EGFR Au nanocages. These results exemplify that the anti-EGFR Au nanocages are effective photothermal agents capable of absorbing light and converting it into heat. The flow cytometry data also reveals that cells targeted by the anti-EGFR Au nanocages display irreversible damage upon photothermal treatment, as shown by the larger population in quadrant-III, where the cellular membrane is broken to such an extent that the cell can no longer function nor recover from the damage. Although a small portion of damaged cells are present in quadrant-II, the majority is observed in quadrant-III suggesting that the decrease of cellular damage over time was cause by the proliferation of cells outside the spot size and not by the recovery of the compromised cells as speculated earlier.

I also investigated the effect of the laser power density. Figure 4.4 shows a plot of cellular damage against the laser power density for cells irradiated for 5 min and harvested 3 h after irradiation. In the control, the cells without Au nanocages (in red) maintained viability and the values are consistent with the control experiments shown in Figure 4.3. Cells treated with the anti-EGFR Au nanocages (in black) exhibited little or no damage at power densities less than 1.6 W/cm^2. At some threshold between 1.6 and 2.4 W/cm^2, the damage becomes significantly greater than the control. At power densities greater than 1.6 W/cm^2, the damage for cells treated with the anti-EGFR Au nanocages increases linearly, similar to what was found in previous publication.[15] As the power density increased to 6.4 W/cm^2, the cellular damage increased to 55%. Since the laser irradiated only 9.8% of the well, the cellular damage extended beyond the spot size of the laser, as is expected because the amount of heat generated increases with increasing laser power. As will be discussed later, the heat generated within the spot size can transfer to surrounding regions. Depending on the stage and type of cancer, cancerous cells can invade local regions of tumor sites and removal of nearby regions may be necessary, thus this linear relationship provides a means of calibrating the treatment to kill cancerous cells that have broken away from the primary tumor. Alternatively, by keeping the power density low, collateral damage to nearby healthy cells can be minimized.

The cells were also exposed to the laser for different periods of time. Figure 4.5

shows a plot of cellular damage against the duration of laser exposure for cells irradiated at 4.77 W/cm^2 and harvested 3 h after irradiation. In the control, cells without anti-EGFR Au nanocage treatment (in red) maintained viability, which is consistent with the results from the control experiments shown in Figures 4.3 and 4.4. The percentage of damage for cells treated with anti-EGFR Au nanocages (in black) continuously increased for the first 5 min. After 5 min, the cellular death reached a steady percentage at about 35%. An exposure time of 1 min resulted in cellular damage (18%) larger than the percentage of cells irradiated by the laser (9.8%), suggesting that Au nanocages in the spot size of the laser irradiation responded quickly to the exposure. As the exposure time increased to 5 min, the cellular death increased signifying that the death outside the spot size of the laser depends on the amount of time necessary for heat generated from the anti-EGFR Au nanocages to transfer to cells outside the irradiated regions. The cellular death becomes steady after 5 min, which could be attributed to other temperature gradients in the surroundings thus establishing equilibrium. This relationship is important for calibrating the laser parameters for practical applications of *in vivo* photothermal treatment. For example, a high-powered laser can be expensive, so rather than increasing the power of the laser, the time of laser exposure could be easily prolonged; however, after some extended period of time, the cellular death will become steady. This parameter provides another approach to treat the local invasion of tumor.

4.5 Summary

I have quantified the targeting and photothermal therapeutic effects of 65-nm anti-

EGFR Au nanocages on SK-BR-3 breast cancer cells. Additionally, by combining PI fluorescent labeling with flow cytometry, I was able to distinguish between live and dead cells. This technique proved to be extremely powerful at determining and quantifying the number of nanocages per cell. The relationship between laser parameters (i.e. power density and duration of laser exposure) and cellular damage was also better elucidated. The information garnered from this work will aid in future *in vivo* studies in which the dosage of anti-EGFR Au nanocages and the power density and exposure time of the laser can be optimized to treat individual conditions (e.g., tumor size and local invasion of tumor). Additionally, this study provided more information about the interaction between the cells, anti-EGFR Au nanocages, and laser. For example, it was previously unknown that the anti-EGFR Au nanocages were internalized by the cells. My photothermal studies also showed that cells targeted with anti-EGFR Au nanocages respond immediately to the laser stimuli, and that the amount of cellular death can be controlled by both the exposure time and power density of the laser. Cells treated under the same experimental conditions but without anti-EGFR Au nanocages maintained their viability. The efficacy for the anti-EGFR Au nanocages to kill cancer cells can be attributed to their selective targeting and large absorption cross-section of near-infrared light. The results reported here provide insight into how the photothermal response of anti-EGFR Au nanocages can be optimized and controlled. This knowledge is critical to providing effective, noninvasive treatment of cancer *in vivo* via photothermal therapy. Future work will also address the stability of Au nanocages in conjunction with its biodistribution via local and systemic administration as well as collateral damage to nearby healthy cells.

4.6 Experimental Section

Preparation of anti-EGFR Au nanocages. Au nanocages were prepared using the galvanic replacement reaction between $HAuCl_4$ and Ag nanocubes as the template. The detailed procedure was described in Chapter 2. SK-BR-3 and U87MGwtEGFR cells both overexpress EGFR on their surface, so the same two-step protocol in Chapter 3 was employed here to target SK-BR-3 cells. For these experiments, the amount and concentration of Au nanocages needed are 1 mL of a 2 nM solution. The thiolated poly(ethylene glycol) (PEG) was OPSS-PEG-SC (Laysan Bio, MW≈5,000) and the amount and concentration used was 1 mL of a 1 mM solution.

Cell culture. The breast cancer cell line SK-BR-3 (ATCC, HTB-30) was cultured in McCoy's 5a Medium Modified (ATCC, 30-2007) containing 10% Fetal Bovine Serum (FBS, Invitrogen, 16000) and 5% streptomycin/penicillin (Invitrogen, 15140) at 37 ^{o}C in 5% CO_2 (v/v). The medium was changed 2-3 times a week. When they reached a confluency of 60-90%, the adherent cells were removed from the growth vessel with trypsin (Gibco, 25200). The trypsin was deactivated by adding the growth medium. The suspension of cells was centrifuged for 5 min at 1,000 rpm, and the pellet of cells were resuspended in growth medium and then transferred to a desired growth vessel (flask, multi-well plate, or petri dish) for quantitative and photothermal studies.

Preparation and imaging of SEM samples. The SK-BR-3 cells were transferred to a silicon wafer and allowed to settle overnight in a 12-well plate. The SK-BR-3 cells were fixed with methanol, and then washed three times with tris-buffered saline tween-20 (TBST), followed by a rinse with tris-buffered saline (TBS). The cells were incubated with 20 μL of the anti-EGFR Au nanocages in TBS for at least 3 h, with 1 h of gentle agitation. After that, the cells were washed three times with TBST and one time with TBS. The sample was briefly rinsed with water and dried before SEM characterization using a Sirion XL field-emission microscope (FEI, Hillsboro, OR) operated at 5 kV.

Preparation and imaging of microtomed samples. The SK-BR-3 cells were grown in a 35-mm Petri dish. They were then incubated with 50 μL of the anti-EGFR Au nanocages in medium for 3 h, with 1 h of gentle agitation. Then, the cells were rinsed three times with PBS and fixed with a solution containing glutaraldehyde (2.5%), cacodylate (0.1 M), sucrase (0.1 M), $CaCl_2$ (0.4 mM) overnight at 4 ^{o}C. The cells were post-fixed with OsO_4 (1 %) in cacodylate (0.1 M) and $CaCl_2$ (0.4 mM) for 2 h at room temperature, followed by uranyl acetate (2 %) in water for 1 h at room temperature. The cells were dehydrated through a graded ethanol series, and finally embedded in eponate (Ted Pella, Redding, CA) epoxy resin and set aside to polymerize for 48 h at 60-65 ^{o}C. A microtome (Reichert/Jung Ultra-cut E, Leica, Arcadia, CA) equipped with a diamond knife was used to cut the cured epoxy resin into slices with a thickness of 80-100 nm. The cell slices were contrasted with an aqueous solution of uranyl acetate (7 %) and lead citrate.[27] The samples were examined using a JEOL EXIII TEM.

Quantification of the number of Au nanostructures attached per cell. SK-BR-3 cells were grown in a 12-well plate and incubated with 20 μL of the anti-EGFR Au nanospheres (Ted Pella, 40 nm in diameter) or 20 μL of the anti-EGFR Au nanocages for

3 h (with 1 h of gentle agitation) in a solution that contained the growth medium. They were rinsed three times with PBS. The adherent cells were removed from the growth vessel with trypsin as described previously. The suspension of cells was collected and spiked with a known amount of Sphero Ultra Rainbow beads (Spherotech, URFP-100-2, 10.2 μm). A known amount of the sample was then inserted into an influx flow cytometer (Cytopeia) with a 488 nm argon laser as the excitation source. Data analysis was performed using FCS Express (DeNovo) software to determine the number of cells in the solution. The remainder of the sample was analyzed to determine the amount of Au present in the sample using ICP-MS (PerkinElmer Elan DRC-e).

Photothermal treatment. SK-BR-3 cells in 96-well plates were incubated with 12 μL of the anti-EGFR Au nanocages for 3 h (with 1 h of gentle agitation). The cells in the center of the wells were irradiated with a Ti:Sapphire laser with a central wavelength at 805-nm and a bandwidth of 54 nm. The near-infrared light source was a femtosecond pulsed irradiation generated from a home-built Kerr-lens mode-locked Ti:Sapphire laser with 82 MHz repetition rate. The Gaussian beam size was adjusted with a convex lens (B coating, BK7, f = 75 mm) and the sample was positioned at a distance such that the spot size was 2 mm in diameter. An iris diaphragm was used to block light outside the spot. The laser power density was adjusted using a neutral attenuator. The duration of irradiation and the power density for photothermal treatment are described in the text. After laser irradiation, the cells were incubated in the medium at 37 °C until they were harvested and analyzed.

Quantification of the photothermal effect. After a certain period of incubation (as indicated in the text), the cells were rinsed with PBS and then harvested with trypsin as described previously. The suspension of cells and rinses with PBS were collected in a tube for flow cytometry analysis. The cellular suspension (400 μL) was treated with PI (12 μL, Molecular Probes, 1 μg/mL stock, in dH_2O) and then inserted into the flow cytometer. The PI fluorescent signal was collected using a 625/25 BP filter. The data was analyzed using the FCS Express software.

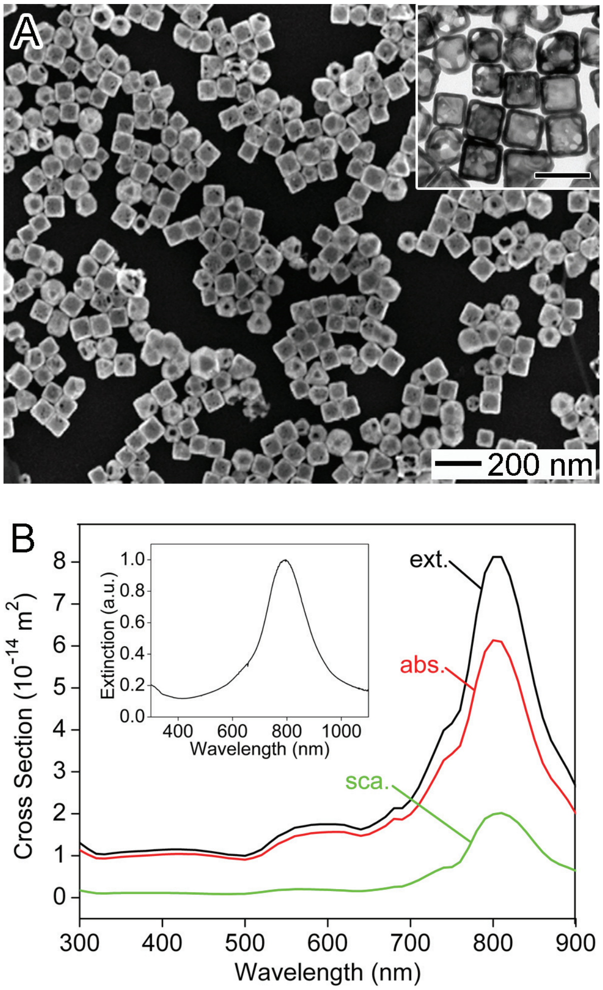

Figure 4.1 (A) SEM and TEM (inset) images of Au nanocages synthesized using the galvanic replacement reaction in which Ag nanocubes serve as a sacrificial template. The scale bar in the inset represents 100 nm. (B) The absorption (C_{abs}), scattering (C_{sca}), and extinction (C_{ext}) cross-sections (note that $C_{ext} = C_{abs} + C_{sca}$) as a function of wavelength were calculated using the DDA method for a Au nanocage with the following geometrical parameters: edge length = 65 nm, wall thickness = 7.5 nm, and corner holes with diameter = 20 nm. Also for the DDA calculations, the nanocages were assumed to be in water and have a composition of 37 % Ag and 63 % Au. The inset shows the UV-visible absorbance spectrum for the nanocages shown in (A), which have a resonance peak at 800 nm, in agreement with the calculations.

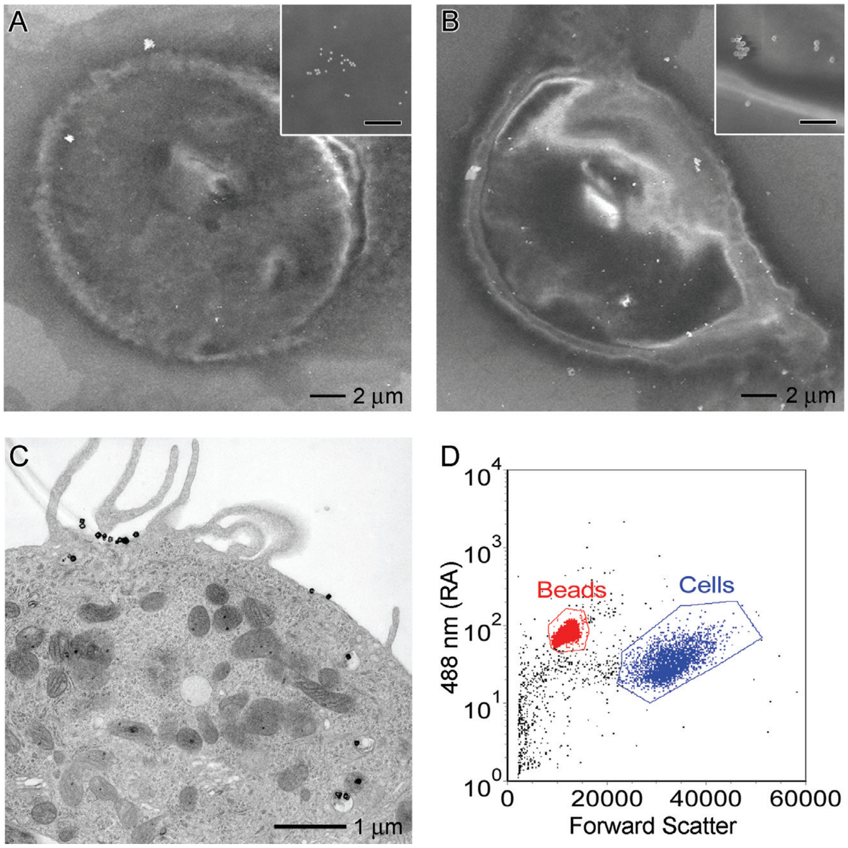

Figure 4.2 SEM images of SK-BR-3 cells targeted with anti-EGFR Au nanospheres (A) and nanocages (B). SEM images at higher magnification (insets) reveal that the bright spots in the SEM images are indeed nanospheres and nanocages, respectively. The scale bar in the insets represents 500 nm. (C) A TEM image of a microtomed SK-BR-3 cell conjugated with anti-EGFR Au nanocages. In addition to anti-EGFR Au nanocages decorating the surface of the cell, this microtomed TEM image reveals that some anti-EGFR Au nanocages are internalized by the cell. However, they do not appear to enter the nucleus. (D) A typical flow cytometry graph indicating how the forward scatter (x-axis) and right angle scatter (y-axis) can be used to differentiate the size difference between beads and cells. As the concentration of beads is known for a given sample, it provides an internal reference for measuring the concentration of cells; when this data is coupled with ICP-MS analysis for Au, the number of anti-EGFR Au nanocages per cell can be estimated.

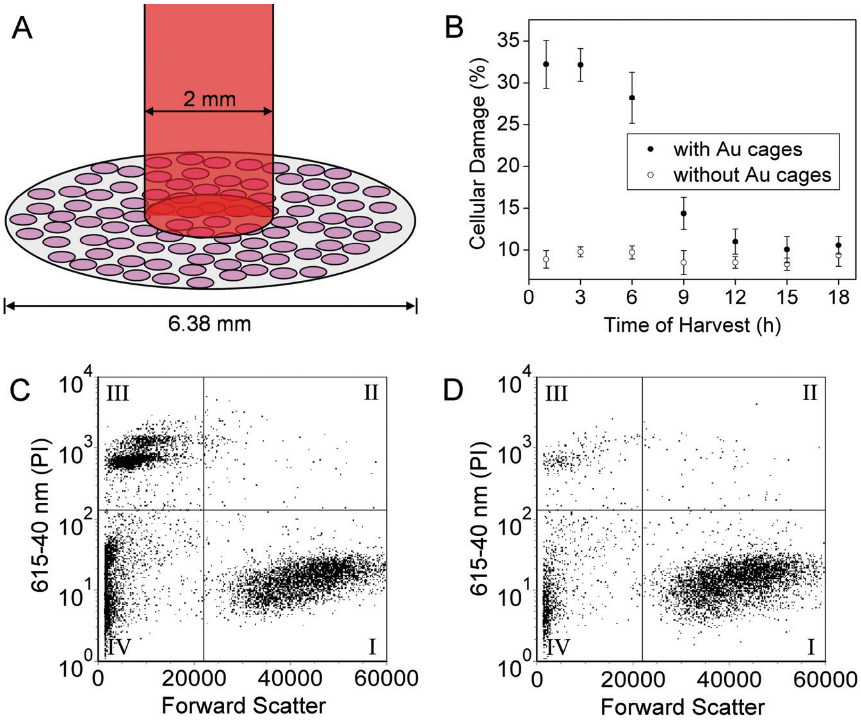

Figure 4.3 (A) An illustration depicting the experimental setup used for photothermal therapy of SK-BR-3 cells. The cellular growth vessel had a diameter of 6.38 mm. The cells were irradiated with an 805-nm Ti-Sa laser with a spot size of 2 mm. Thus, only 9.8 % of the cells in the well were exposed to the laser. Note: cells not drawn to scale. (B) Plots of the percentage of cellular damage versus harvest time when SK-BR-3 cells were irradiated for 5 min at a laser power of 4.77 W/cm^2. The solid dots show the results for cells targeted with anti-EGFR Au nanocages, and the open dots show the control (no incubation with anti-EGFR Au nanocages). (C) The flow cytometry graph analyzed to determine the percentage of cellular death after SK-BR-3 cells were incubated with anti-EGFR Au nanocages, irradiated for 5 min at a power density of 4.77 W/cm^2, then harvested at 3 h for analysis. (D) The flow cytometry graph obtained from the control experiment in which SK-BR-3 cells were not treated with anti-EGFR Au nanocages but treated to similar laser treatment. For both (C) and (D), the signal in quadrant III corresponds to population of dead cells.

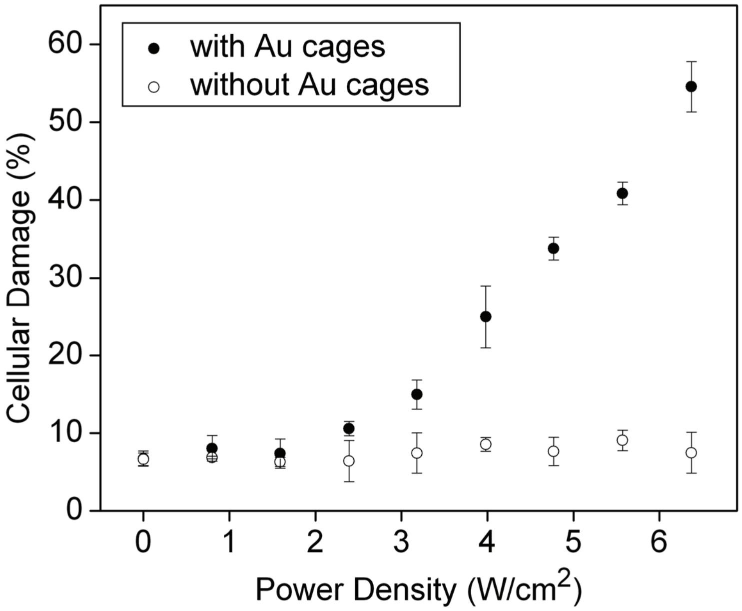

Figure 4.4 Plot of cellular damage versus laser power density for SK-BR-3 cells incubated with anti-EGFR Au nanocages (solid dots) and for the control in which cells were not incubated with anti-EGFR Au nanocages (open dots). Cells were irradiated for 5 min and then harvested for analysis 3 h after irradiation.

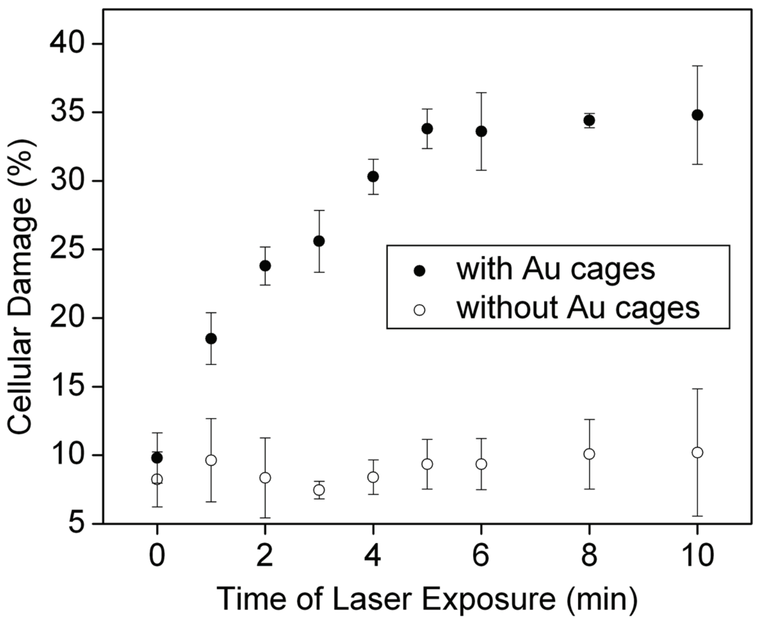

Figure 4.5 Plot of cellular damage versus laser exposure time for SK-BR-3 cells incubated with anti-EGFR Au nanocages (solid dots) and for the control in which cells were not incubated with anti-EGFR Au nanocages (open dots). In both cases, the cells were irradiated with a 805 nm laser at a power density of 4.77 W/cm^2 then then harvested for analysis 3 h after irradiation.

4.7 Notes to Chapter 4

[1] Hu, M.; Chen, J.; Li, Z. Y.; Au, L.; Hartland, G. V.; Li, X.; Marquez, M.; Xia, Y. *Chem. Soc. Rev.* **2006**, *35*, 1084.

[2] Jain, P. K.; Huang, X.; El-Sayed, I. H.; El-Sayed, M. A. *Accounts of Chemical Research* **2008**, *41*, 1578.

[3] Xia, Y.; Halas, N. J. *MRS Bull.* **2005**, *30*, 338.

[4] Pissuwan, D.; Valenzuela, S. M.; Cortie, M. B. *Trends Biotechnol.* **2006**, *24*, 62.

[5] Averitt, R. D.; Westcott, S. L.; Halas, N. J. *J. Opt. Soc. Am. B* **1999**, *16*, 1824.

[6] Oldenberg, S. J.; Averitt, R. D.; Westcott, S. L.; Halas, N. J. *Chem. Phys. Lett.* **1998**, *28*, 243.

[7] Kelly, K. L.; Coronado, E.; Zhao, L. L.; Schatz, G. C. *J. Phys. Chem. B* **2003**, *107*, 668.

[8] Link, S.; El-Sayed, M. A. *J. Phys. Chem. B* **1999**, *103*, 8410.

[9] Murphy, C. J.; Sau, T. K.; Gole, A. M.; Orendorff, C. J.; Gao, J.; Gou, L.; Hunyadi, S. E.; Li, T. *J. Phys. Chem. B* **2005**, *109*, 13857.

[10] Sun, Y.; Xia, Y. *Science* **2002**, *298*, 2176.

[11] Sun, Y.; Xia, Y. *J. Am. Chem. Soc.* **2004**, *126*, 3892.

[12] Cang, H.; Sun, T.; Li, Z.-Y.; Chen, J.; Wiley, B. J.; Xia, Y.; Li, X. *Opt. Lett.* **2005**, *30*, 3048.

[13] Siekkinen, A. R.; McLellan, J. M.; Chen, J.; Xia, Y. *Chem. Phys. Lett.* **2006**, *432*, 491.

[14] Skrabalak, S. E.; Au, L.; Li, X.; Xia, Y. *Nat. Protoc.* **2007**, *2*, 2182.

[15] Chen, J.; Wang, D.; Xi, J.; Au, L.; Siekkinen, A.; Warsen, A.; Li, Z.-Y.; Zhang, H.; Xia, Y.; Li, X. *Nano Lett.* **2007**, *7*, 1318.

[16] Hirsch, L. R.; Stafford, R. J.; Bankson, J. A.; Sershen, S. R.; Rivera, B.; Price, R. E.; Hazle, J. D.; Halas, N. J.; West, J. L. *Proc. Natl. Acad. Sci. U.S.A.* **2003**, *23*, 13549.

[17] Huang, X.; El-Sayed, I. H.; Qian, W.; El-Sayed, M. A. *J. Am. Chem. Soc.* **2006**, *128*, 2115.

[18] Loo, C.; Lowery, A.; Halas, N.; West, J.; Drezek, R. *Nano Lett.* **2005**, *5*, 709.

[19] O' Neal, D. P.; Hirsch, L. R.; Halas, N. J.; Payne, J. D.; West, J. L. *Cancer Lett.* **2004**, *209*, 171.

[20] Lu, X.; Au, L.; McLellan, J.; Li, Z.-Y.; Marquez, M.; Xia, Y. *Nano Lett.* **2007**, *7*, 1764.

[21] Chen, J.; Saeki, F.; Wiley, B. J.; Cang, H.; Cobb, M. J.; Li, Z.-Y.; Au, L.; Zhang, H.; Kimmey, M. B.; Li, X.; Xia, Y. *Nano Lett.* **2005**, *5*, 473.

[22] Chen, J.; Wiley, B. J.; Li, Z.-Y.; Campbell, D.; Saeki, F.; Cang, H.; Au, L.; Lee, J.; Li, X.; Xia, Y. *Adv. Mater.* **2005**, *17*, 2255.

[23] Nagy, P.; Jenei, A.; Kirsch, A. K.; Szollosi, J.; Damjanovich, S. *J. Cell Sci.* **1999**, *112*, 1733.

[24] Frankel, A. *Clin. Cancer Res.* **2002**, *8*, 1699.

[25] Hurwitz, E.; Stancovski, I.; Sela, M.; Yarden, Y. *Proc. Natl. Acad. Sci. U.S.A.* **1995**, *92*, 3353.

[26] Arndt-Jovin, D. J.; Jovin, T. M. *Methods Cell. Biol.* **1989**, *30*, 417.

[27] Reynolds, E. S. *J. Cell Biol.* **1963**, *16*, 208.

Chapter 5

Synthesis of Gold Microplates Using Bovine Serum Albumin as a Reductant and a Stabilizer

5.1 Introduction

Anisotropic 2-D structures have been recently gained attention because of their unique optical properties and potential use in chemical and biological sensing. Triangular and hexagonal plates are of interest because they have particularly attractive optical properties. They exhibit both dipole and quadrupole plasmon resonance peaks due to their anisotropic shape. It has been demonstrated that as Au nanoplates grow larger into microplates, their dipole resonance shifts into the near-infrared region and their quadrupole resonance peak becomes more prominent.[1,2] Their resonance peaks in the near-infrared region are useful for biological applications because soft tissues are transparent in this range. Moreover, their sharp corners and edges also make them useful as substrates for surface-enhanced Raman scattering (SERS).[3] Researchers have long studied the synthesis of plates and their mechanism of formation using electron microscopy and theoretical modeling.[4-7] The major conclusions reached thus far are the following: plates are derived from seeds with planar defects (e.g., lamellar twins or stacking faults). These planar defects can be obtained from kinetically controlled syntheses, in which the reduction of a salt precursor is relatively slow and the atoms will rearrange in a randomly hexagonal closed-packed (rhcp) structure—a mixture of both hexagonal close-packed (hcp) and cubic close-packed (ccp) stacking. Nuclei with an rhcp structure can easily evolve into a plate-like seed which are characterized by vertical stacking faults. Nanoplates have been synthesized in various ways through thermal and photochemical methods.[8,9] Recently, there has been a number of green chemistry methods developed to produce Au plates using biological molecules.

Biological systems assemble inorganic nanoscale building blocks into structures with controlled size and complex patterning, such as bones and shells. Researchers have long tried to understand this process, and more recently, to harness it to grow nanostructures with controlled morphologies. For gold, previous biological syntheses have employed extracts from lemongrass,[10] brown seaweed,[11] unicellular green alga[12] and filamentous fungus[13] to grow nanoplates. These extracts are inherently mixtures of proteins, so it is difficult to identify the particular protein structure responsible for guiding the growth of nanoplates.

Serum albumin is the most abundant plasma protein in mammals and is essential for the regulation of the colloidal osmotic pressure and maintenance of pH levels in blood.[14] It is the principal transporter for a variety of substances with different properties (e.g., hydrophobic or hydrophilic, anionic or cationic). Bovine serum albumin (BSA) is one of the most thoroughly characterized, inexpensive and ubiquitous proteins. BSA has a molecular weight of ~66 kDa and is composed of 582 amino acids, of those, 35 are threonine and 32 are serine units.[15-18] These amino acids bearing hydroxyl groups can serve as reducing agents. For example, poly(vinyl pyrrolidone) containing two hydroxyl end groups has been shown to be a mild reducing agent capable of producing nanoplates of noble metals such as Au, Ag, Pt, Pd.[19]

Previously, BSA has been shown to be a good stabilizer for the synthesis of Au-Ag and Ag-Pt alloy nanoparticles owing to their excellent foaming behavior and ability to simultaneously bind to both Ag^+ and $AuCl_4^-$ or $PtCl_6^-$, respectively, ions due to its zwitterionic characteristic at the isoelectric point (BSA pI = 4.7).[20,21] I found that BSA not only acts as a stabilizing agent against the aggregation of Au nanoparticles, but also, the hydroxyl groups of BSA make it a reducing agent, so no additional reductant is required. In this study, I focus on the effect of BSA on the growth of triangular and hexagonal Au microplates in an aqueous buffered solution. The conformation of the protein is an important factor for the synthesis of these Au microplates and is dependent on temperature and pH of the reaction. Additionally, the ions in the environment are important to the stability of the protein structure.

5.2 Unfolding the Structure of BSA

In its native state, BSA is a heart-shaped protein and consists of three homologous domains (I, II, and III), each bearing a number of ionizable groups.[22,23] The secondary structure of BSA consists of 67% helix, 10% turn, and 23% extended chain.[24] The cysteine residues are responsible for the tertiary structure of the protein. They form 17 disulfide bonds which results in nine loops. It is worth pointing out that BSA has one free sulfhydryl group located at the cysteine residue in position 34 of the amino acid sequence (Cys-34). Cys-34 is located in a crevice near the surface of the protein and is thereby protected by neighboring residues. Figure 5.1A shows an illustration of a portion of BSA. When the protein is exposed to heat and $HAuCl_4$, the structure of BSA can unfold to reveal the reductive hydroxyl groups in threonine and serine units. Customarily, disulfide bonds in protein are reduced with mercaptans such as thioglycolic acid, 2-mercaptoethanol, and cysteine.[25] However, in the presence of gold, the disulfide bond will break and form a Au-thiolate bond. It has been previously observed that $HAuCl_4$ in the presence of a thiol can from a Au-chloride-sulfur complex.[26] Recently, it was reported the cys-34 residue of BSA and thiomalate (Stm) can coordinate to form albumin-S-Au-Stm.[27] Hence, it is possible that such an intermediate complex could be formed in my system, which will facilitate in breaking the disulfide bonds in BSA and further promote the unfolding of the protein and expose more hydroxyl groups. Both hydroxyl and sulfhydryl groups are important for the synthesis of Au microplates: the hydroxyl group serves as the reducing agent and the sulfhydryl group provides the BSA molecule a chemical method of attaching to the Au surface to function as a stabilizing agent.

The scanning electron microscopy (SEM) image in Figure 5.1B shows the microplates obtained at the experimentally determined optimal conditions. In this case, 0.050 g of BSA was dissolved in 5 mL of tris-buffered saline (TBS, pH = 7.4) and heated at 55 ^{o}C for 30 minutes before the addition of 3 mL of 18.8 mM $HAuCl_4$ in TBS. Throughout this chapter, this protocol will be referred to as the standard procedure or method. The initial BSA solution was clear and colorless. Upon the addition of $HAuCl_4$, the solution became cloudy and yellow. This yellow color was due to the presence of Au^{3+} ions and the turbidity was due the denaturation of BSA. Within 10 minutes, the yellow color disappeared, leaving behind a white opaque solution. The loss of the yellow color indicated the reduction of Au^{3+} to Au^{1+}. The cloudy solution then developed a light reddish-brown color, indicating the presence of nanoparticles. As the reaction continued, the Au particles grew to form micron-sized plates and the solution evolved to a clear, shimmery yellow solution after 2 hours. The pH of the solution was measured after the addition of $HAuCl_4$ and found to have dropped from 7.4 to 2.0. The majority of the products were hexagonal and triangular plates with mean edge lengths of 3.6 ± 0.6 μm and 8.6 ± 2.0 μm, respectively. Figure 5.1C and D show TEM images of single hexagonal and triangular plates, respectively. Their corresponding electron diffraction (ED) pattern (insets of Figure 5.1, C and D) was taken by directing the electron beam perpendicular to the flat faces. Three sets of patterns can be seen. The squared, triangled, and circled spots can be indexed to the {220}, {422}, and forbidden 1/3{422} reflections, respectively. Such diffraction spots are consistent with previous observations of Au and Ag plate structures.[2,19,28] The observation of the forbidden 1/3{422} reflection reveals the presence of (111) stacking faults. This twinned defect disrupts the *fcc* symmetry of gold and is responsible for the formation of anisotropic disc structures. It should be noted out that planar defects can be produced by the slow reduction derived from the mild reducing power of BSA.

5.3 Effect of Temperature

Temperature plays an important role in this synthesis. As previously discussed, it is expected to influence the conformation of the protein. The driving force for protein denaturation is entropy, and an increase in the temperature would increase the entropic effect. Moreover, the temperature should affect the reduction rate of Au ions as well as the rates of the nucleation and growth processes of the nanocrystals. I explored various temperatures ranging from 4 ^{o}C to 75 ^{o}C, while keeping the rest of the parameters the same as the standard procedure. I found that at 4 ^{o}C, BSA had very little reduction capability. The reaction remained yellow and cloudy for up to one week. A TEM image of this sample at 40 hours revealed that 1-10 nm seeds were embedded within the protein as shown in Figure 5.2A. This result means that BSA protein had some reductive capability at 4 ^{o}C, though the reduction of Au ions was exceedingly slow and the growth of these seeds into larger crystals was not observed. Subsequently, I increased the temperature of the reaction to physiological temperature, 37 ^{o}C. The reaction was completed within 18 hours and exhibited the same color progression as the standard method over this time period. Few hydroxyl groups are expected to be exposed at 37 ^{o}C since BSA only begins to denature at 40 ^{o}C, and as a result, the reduction was very slow. I also conducted the synthesis at 45 ^{o}C and found that the reaction rate increased considerably; the reaction was completed within 4 hours. However, the products obtained at 37 ^{o}C and 45 ^{o}C were polydispersed samples containing both particles and a broad size distribution for the plates. Figure 5.2B shows the SEM image of the products obtained at 37 ^{o}C. This polydispersity was likely due to the different conformations of the BSA present during heating. During the initial stages of heating, unlocking the tertiary structure removed a number of bonds holding the structure together, thus increasing the number of possible BSA configurations. The hydrogen bonds within the alpha helices were broken and the structure unfolded to random coils, which can align and hydrogen bond between each other to form β-sheets. It is worth pointing out that the conformation of the protein was reversible for temperatures less than 52 ^{o}C, resulting in small fluctuations between the structures of BSA molecules which may be responsible the polydispersed sample.

It was not until the reaction was increased to 55 ^{o}C when I obtained a good distribution of Au plates (Figure 5.1B). The unfolding of the α-helices of BSA molecules was irreversible at temperatures higher than 52 ^{o}C because the cysteine pocket unfolded and formed disulphide bonds between the β-sheets. [24,29-31] Thus, I expect the structure of the protein to be quite stable at 55 ^{o}C, which will aid in the formation of uniform plates. Figure 5.2C shows hexagonal and triangular plates that were obtained at a reaction temperature of 65 ^{o}C. The plates have a similar size distribution to those obtained in the standard procedure. It seems that within this temperature range, 55 ^{o}C - 65 ^{o}C, the structure of the BSA was relatively stable and formed uniform plates. However, at temperatures above 70 ^{o}C the α-helices continue to unfold and form β-aggregation. As the temperature of the reaction was increased to 75 ^{o}C, the color of the reaction progressed differently. It evolved from yellow and turbid, to cloudy white, and then finally opaque dark reddish-brown. The SEM image in Figure 5.2D shows that the product obtained at 75 ^{o}C consisted of a mixture of spherical particles and plates. The inset in Figure 5.2D shows a SEM image at a higher magnification for the spherical particles revealing that they were actually decahedrons and icosahedrons. These twinned particles are typically observed from seeds with metastable rhcp structure.[5] The hexagonal and triangular plates have mean edge lengths of 1.5 ± 0.7 and 3.0 ± 2.5 nm, respectively. The sizes of the hexagonal and triangular plates synthesized at 75 °C were significantly smaller than those that were synthesized at 55 °C.

This dramatic difference is likely attributable to the conformation of the protein rather than the faster reduction of Au ions at higher temperatures. To prove this hypothesis, I conducted a reaction where the BSA solution was heated to 75 °C for 30 minutes, and then lowered to 55 °C. The shape of the protein should not change when the temperature was lowered since the conformation is irreversible when heated above 52 °C. $HAuCl_4$ was added to the solution and the reaction was completed in 2 hours. The SEM image in Figure 5.3 reveals that the products were a mixture of plates and particles, similar to what was obtained when the reaction was held at a constant temperature of 75 °C. The hexagonal and triangular plates have mean edge lengths of 1.2 ± 0.5 μm and 2.3 ± 2.1 μm, respectively, which were not significantly different from the products obtained at the constant 75 °C. Though the temperature had some influence on the reaction kinetics, it was the conformation of the BSA that strongly affected the synthesis at this temperature range.

5.4 Effect of pH

As mentioned earlier, the pH value is also expected to affect the structure of the protein. BSA contains a large number of groups that can be protonated at different pH conditions, which can alter the hydrogen bonding within BSA molecules (i.e. α-helices) and lead to variation in the structure of the protein.[32] BSA has five pH-dependent structural transitions, all of them are reversible.[33] These states and their points of transition are summarized in Table 1 (modified from ref. [32]). In my previous syntheses, the BSA was preheated for 30 minutes in TBS solution with a pH value of 7.4. At this pH value, the BSA was in its native, globular state also known as the normal dominant (N) form. When $HAuCl_4$ was added to the solution, the pH value decreased to 2.0 and the protein underwent two structural changes: the fast migration (F) and expanded (E) forms. The N-F transition implies the opening of the protein by unfolding domain III, resulting in a loss of α-helix content.[34] The macromolecule further unfolds and loses the helical structure connecting domain I with domain II and III in F-E transition.[35]

In this section, I examined the effect of pH by changing the initial pH value of TBS solution from ~9 to 3.0 or 10.0 through the addition of HCl and NaOH, respectively. The reaction was carried out the same manner as the standard method, except the TBS solution utilized in the reaction had a pH value of 3.0 or 10.0. When the reaction was conducted with TBS of pH = 3.0, the color of the reaction progressed similar to the standard procedure. The final solution was a clear, shimmery yellow solution. Figure 5.4A shows the Au microplates obtained at when TBS with pH = 3.0 was utilized. The pH of the solution was measured at the end of the reaction and found to have decreased to 1.7, similar to the pH value of 2.0 that was measured for the standard method. The structure of the protein at the end of the reaction is expected to be the same structure as in the standard method, which is the E form. The mean edge lengths of hexagonal and triangular plates were 5.8 ± 1.6 and 15.8 ± 3.9 nm, respectively. These plates were significantly larger than the plates obtained in the standard procedure. It was previously observed that in acidic conditions, Au plates grew larger than those synthesized in less acidic environment.[36] I propose that the presence of additional H^+ ions provides increased stability for the Au ions by forming a Au ion complex and hence slowing down the reduction of Au. As a result, the number of seeds formed was reduced and more atoms can be adsorbed to the seeds, which allowed for the formation of larger crystals.

For the reaction conducted with TBS at pH = 10.0, the reaction progressed in different manner. Upon the injection of $HAuCl_4$, the reaction was a clear yellow solution instead of the previously cloudy solution. The solution started turning cloudy after one hour and remained light yellow and cloudy for the next day and a half. Around 40 hours into the reaction, the solution turned light purple, indicating the formation of nanoparticles. When the reaction was carried out for longer times, the solution turned into a dark purple color. Figure 5.4B shows the product obtained at 40 hours are indeed a mixture of nanoparticles. While most of the products were spherical nanoparticles with mean diameter of 8.6 ± 1.0 nm, triangular nanoplates with a mean edge length of 12.2 ± 3.5 nm were produced. The pH of the solution was measured and found to have dropped from 10.0 to 5.6, which means that the structure of the BSA was in the N form at the end of the reaction. By varying the pH of the reaction, I have found that microplates tended to form in acidic conditions when the protein was in the E form, whereas small nanoparticles formed in neutral conditions when the protein was in the N form.

It was previously reported that BSA has one sulfhydryl group available at pH = 7 and three sulfhydryl groups exposed at pH = 3 in the presence of thioglycolic acid.[37] At these pH values, the shape of the BSA corresponds to the N and E forms, respectively. I suspected that in addition to the shape of the protein, the number of sulfhydryl groups available was responsible for the different Au structures synthesized. I observed that the N form produced many small spherical nanoparticles, whereas the E form produced the larger triangular and hexagonal plates. The N form of the protein is globular with one sulfhydryl group exposed, which means that many BSA molecules can surround and stabilize the small nanoparticle. On the other hand, the E form of BSA is an elongated, linear structure and has multiple sulfhydryl groups which can attach to various points on the surface of a flat Au structure. This linear conformation of BSA promotes the growth of plates by attaching to its flat surface, thereby allowing atoms to add on to the edges.

5.5 Effect of BSA Concentration

Figure 5.5 shows the SEM images of the products synthesized with different amounts of BSA while keeping the rest of the parameters the same as the standard method. Generally as the amount of BSA increased from 0.010 to 0.090 g, the edge length of hexagonal plates decreased from 4.6 µm ± 1.9 µm to 1.8 µm ± 0.2 µm. This trend has been observed in many other systems and can be attributed to the following logic: the increase of reductant resulted in the formation of more nuclei. Consequently, less salt precursor was available per nuclei so crystals could not grow to larger sizes.[38] Considering BSA as a stabilizing agent, an increased concentration of stabilizing agent would more effectively form a stabilizing layer around each plate thus preventing the growth of larger plates. Previous syntheses using poly(vinyl pyrrolidone) as the stabilizing agent for the platinum oxide nanoparticles have also demonstrated this behavior.[39] There was no color change to indicate reduction for reactions with less than 0.010 g of BSA. Reactions containing more than 0.15 g of BSA resulted in the formation of gels.

5.6 AFM Characterization of Gold Microplates

The Au microplates synthesized using the standard method were also characterized by atomic force microscopy (AFM) in tapping mode. Figure 5.6A shows the height image of a single hexagonal plate. The thickness of the plates was measured and found to have a mean thickness of 90 ± 10 nm. Figure 5.6B shows the corresponding amplitude image of the same plate. In the amplitude image, finer structures on the surface of the microplates can be observed. When I focus on these finer features, small regular bumps were observed on the surface of the microplate. The phase contrast image shown in Figure 5.6C show that there were significant changes in the phase angle of the cantilever probe along the surface, suggesting that the surface has a heterogeneous chemical composition. The bumps are likely BSA on the surface of the Au microplate since there were only two ingredients in this recipe, gold and BSA. Figure 5.6, D-F are the height, amplitude, and phased contrast images, respectively, of the boxed region in Figure 5.6C.

To fully determine whether the bumps on the surface are BSA, I attempted to displace the proteins from the surface. Proteins are known to be digested in a solution of strong acid (i.e., food digestion). I soaked the Au microplates in a 50/50 solution of HNO_3 and water overnight. The gold was not expected to oxidize under this condition because this noble metal requires both HCl and HNO_3 for oxidation. Gold can form a complex with chloride in oxidizing environments, so prior to incubation with HNO_3, the microplates were washed multiple times with water to ensure no sodium chloride was left behind from the reaction solution. The sample was reimaged with AFM. Figure 5.7, A-C, shows the height, amplitude, and phase contrast images, respectively, of the Au microplates. The HNO_3 treatment did not have any effect on the overall shape and size of the Au microplates; however, a closer look at the surface of the microplates revealed that the surface of the microplates had changed. The height, amplitude, and phase contrast images of the boxed region in Figure 5.7C are shown in Figure 5.7, D-F, respectively. The bumps on the surface of the plate no longer appear regular; instead they seem to have aggregated into larger clumps. These results confirmed that the bumps on the surface are indeed BSA and not gold, since the metal should not have been affected by HNO_3. The strong acid caused the protein across the surface to shrink, thus to form larger aggregates. Additionally, no divots were observed on the surface of the plate after HNO_3 treatment, suggesting the BSA molecules are not embedded within the Au microplates but rather reside on the surface only.

5.7 Effect of Ionic Environment

In addition to temperature and pH, the ionic environment is important to the structure of proteins. In a biological system, the solvent is not pure water; it contains many ions which are involved in the regulation of protein structure and function. Proteins have charges distributed non-uniformly across their surface. For BSA, domains I, II, and III have a calculated net charge of -10, -8 and 0, respectively, at pH = 7. The ions in solution stabilize these charges, and therefore the BSA structure, by direct interactions via salt bridges, as well as indirect interactions through the electrostatic shielding or osmotic stress.[40] Hence, the ionic environment can induce numerous protein conformations.

To understand the effect of ions on my synthesis, the reaction was first conducted in the absence of any additional ions (i.e., tris, NaCl, HCl, NaOH). TBS was replaced with 18 MΩ water in the procedure and the temperature of the reaction was varied from 37 °C to 75 °C. I observed that the removal of the ions had a stronger effect on the reactions at lower temperatures than at higher temperatures. Figure 5.8A shows that the product obtained at 37 °C exhibited a screw dislocation in the center of the plate. In 1949, F. C. Frank suggested that linear defects oriented normally to the growing surface formed the core of a lattice structure, similar to a spiral staircase.[41,42] Figure 5.8B shows a tilted SEM image of the same sample. Unlike the reaction at 37 °C, multiple screw dislocations appeared near the edge of the plate for the reaction conducted at 55 °C, shown in Figure 5.8D. The edge shown in the inset of Figure 5.8D was decorated with dislocations. A possible explanation for this observation is that as the plate grew, the strain on the surface was too great and resulted in dislocations near the edges. When the temperature was increased to 75 °C, screw dislocations were no longer observed. The products synthesized were mostly hexagonal and triangular plates, and occasionally plates adjoined together, shown in Figure 5.8D. The white arrows point out where the edge of one plate merges with another. The inset of Figure 5.8D shows the merging region at a higher magnification. The removal of ions from the solution has induced conformational changes to BSA in such a way, different from the temperature and pH, that promoted dislocations during the growth of plates. However, at higher temperatures (75 °C), the denaturation of the protein was dominated by the temperature rather than ionic conditions, consequently no screw dislocations were observed.

A variety of proteins are known to denature at low salt concentration.[43-46] There are two main components of TBS: sodium chloride (NaCl) and tris (hydroxymethyl aminomethane) (tris). NaCl is the primary constituent in the TBS solution, about five times more than tris. NaCl is found in nearly all biological systems and is known to affect the structure of BSA. BSA is in its native state at NaCl concentrations greater than 0.1 *m*. Decreasing concentrations of NaCl was previously reported to denature BSA molecules, similar to the effect of heat-induced denaturation.[40] The other constituent is tris, a weak base commonly used for buffers. To determine the effect these two ions have in my system, I performed the reactions following the standard procedure, except the TBS solution was replaced with 18 MΩ water supplemented with either NaCl or tris. The concentration of NaCl or tris was consistent to the concentration in the standard protocol. Figure 5.9A shows the SEM image of the products acquired when the reaction was performed in 18 MΩ water with NaCl. Screw dislocations were not observed; Au microplates were synthesized once more. The hexagonal microplates had edge lengths of 3.3 ± 1.2 μm. These hexagonal plates were bigger and had a larger size distribution than those obtained during the standard protocol. When the reaction was performed with tris instead of NaCl, screw dislocations were again observed along with relatively small irregular shaped particles, shown in Figure 5.9B. These products were different from those obtained in pure water (Figure 5.8C). From these experiments, it was clear that both NaCl and tris influenced the structure of the protein. I concluded that NaCl was critical for the formation of microplates given that experiments carried out without NaCl resulted in Au structures with screw dislocations. Additionally, it was possible that NaCl may also affect the nucleation and growth of the crystal, but the exact mechanism is not yet known. Tris alone did not seem to play a major role in synthesizing Au microplates; however, I found that the addition of tris with NaCl yielded plates with a narrower distribution than the reactions without tris. Tris and NaCl may have co-solute interactions with the protein, consequently resulting in different structures of BSA that can affect the quality of the products. The exact structure of BSA in these conditions has yet to be characterized.

5.7 Summary

I have examined the effect of one of the most ubiquitous proteins, BSA on the growth of Au nanocrystals into micron-sized plates. The hydroxyl groups in BSA served as a weak reducing agent at mild temperatures, thus providing a kinetically controlled pathway to produce seeds with planar defects, which then grow into Au microplates.

These hydroxyl groups were exposed by denaturing the structure of BSA through various conditions such as temperature, pH, and the ionic environment. The cysteine residues provided a chemical method of adhering BSA on to the Au surface to function as a stabilizing agent. Gold microplates were obtained when the structure of BSA denatured at 55 °C in acidic conditions containing NaCl. These Au microplates were synthesized with biomacromolecules and can be readily translated into biosystems. For example, they can be used as a platform for confining cellular growth or as a substrate for the SERS detection of biomarkers. Additionally, these microplates have both nano- and micro- characteristics. The thickness of the Au microplates was on the scale of nanometers which allowed them to be transparent, and the lateral dimensions were on the scale of micrometer, which gave these plates their reflective and conductive characteristics. Hence, Au microplates can potentially serve as transparent electrodes and deformable mirrors. I have only begun to examine the possibilities of using biological molecules to control the growth of nanostructures into a desired morphology. Using biological molecules provided a simple method to control the assembly of metal atoms in solution.

5.9 Experimental Section

TBS solutions were prepared by dissolving tris (0.030 M, Fisher) and NaCl (0.14 M) in 18 MΩ water. The pH was adjusted to 3.0, 7.4, or 10.0 using HCl or NaOH. In a typical synthesis, BSA (0.0100 g to 0.0900 g, Aldrich, A9647) was dissolved in TBS (5.0 mL) in a 24 mL vial and the given temperature specified in the text for 30 minutes. In the meantime, $HAuCl_4$ solutions (18.8 mM, Aldrich, 520198) were prepared in the appropriate TBS solutions. After, the $HAuCl_4$ solution (3 mL) was injected rapidly into the vial. The entire synthesis was carried out under magnetic stirring. The reaction solution was centrifuged at 13,200 rpm for five minutes. The Au structures were then suspended in water by sonication while the protein remained as a pellet. The supernatant containing Au plates was washed with water three times to further remove BSA. A drop of the aqueous suspension of the Au product was placed on a piece of silicon water (for SEM and AFM) or carbon-coated copper grid (Ted Pella, Redding, CA, for TEM and ED) and dried under ambient conditions for characterization. SEM images were collected using a FEI field-emission scanning microscope (Sirion XL) operated at an accelerating voltage of 10 kV. TEM images and ED patterns were captured using a Phillips 420 transmission electron microscope operated at 100 kV. Height, amplitude, and phase contrast images were collected simultaneously in tapping mode using a Nanoscope V Multimode SPM (Veeco Instruments Inc.).

Table 5.1 pH-Dependent Conformations for BSA (reproduced from ref. [32])

State	E		F		N		B		A
Description	Expanded	←→	Fast migration	←→	Normal	←→	Basic	←→	Aged
pH of transition		2.7		4.3		8		10	

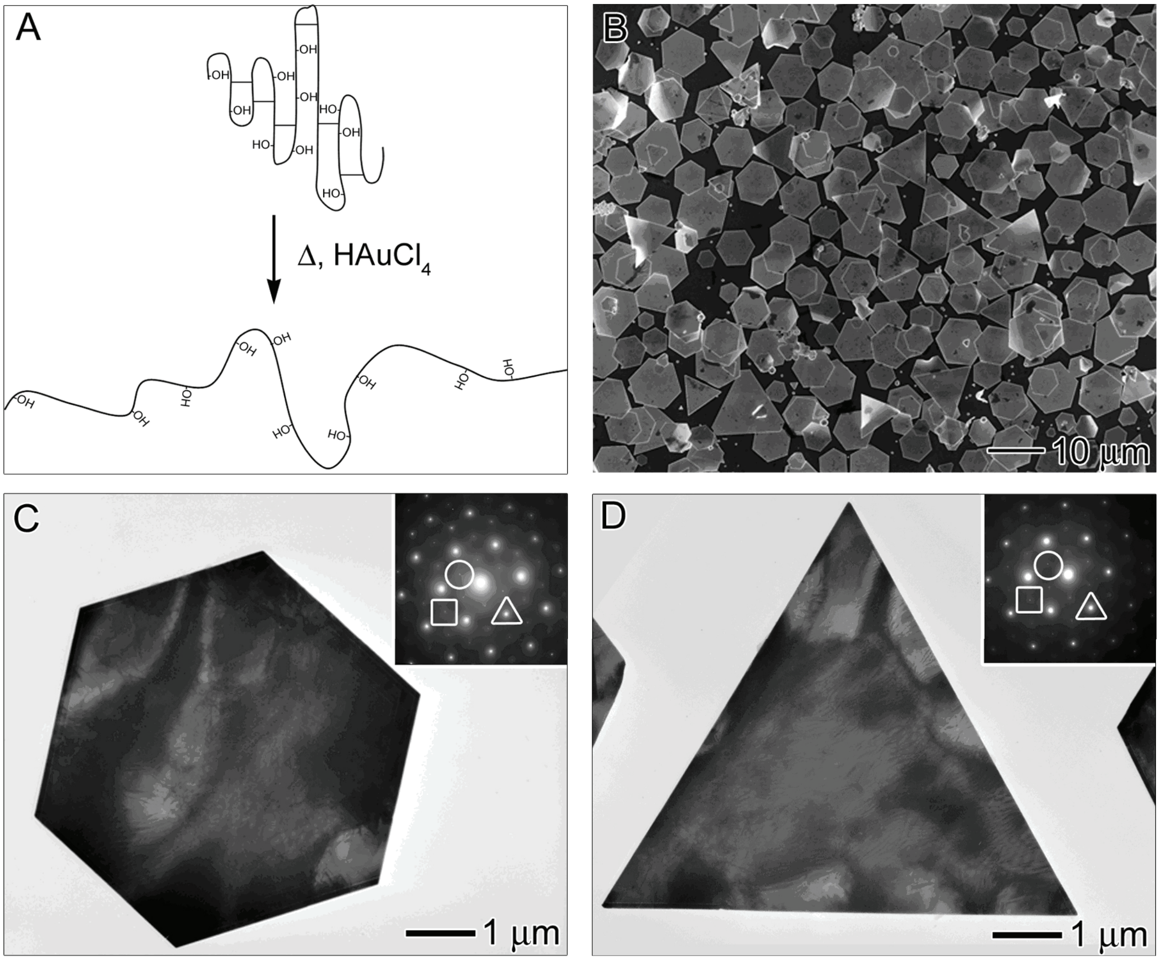

Figure 5.1 (A) Illustration of a portion of BSA undergoing structural changes when exposed to heat and $HAuCl_4$. The protein unfolds and the disulfide bonds break thereby exposing the reductive hydroxyl groups in threonine and serine. (B) SEM and (C, D) TEM images of hexagonal and triangular plates synthesized using the standard procedure, with the addition of 3 mL of 18.8 mM $HAuCl_4$ into a 5 mL TBS solution (pH = 7.4) containing 0.050 g BSA at 55 ^{o}C for 2 hours. The insets in (C) and (D) show the corresponding ED pattern taken by directing the electron beam perpendicular to the flat faces of each plate. The spots squared, triangled, and circled can be indexed to the {220}, {422}, and forbidden 1/3{422} reflections, respectively.

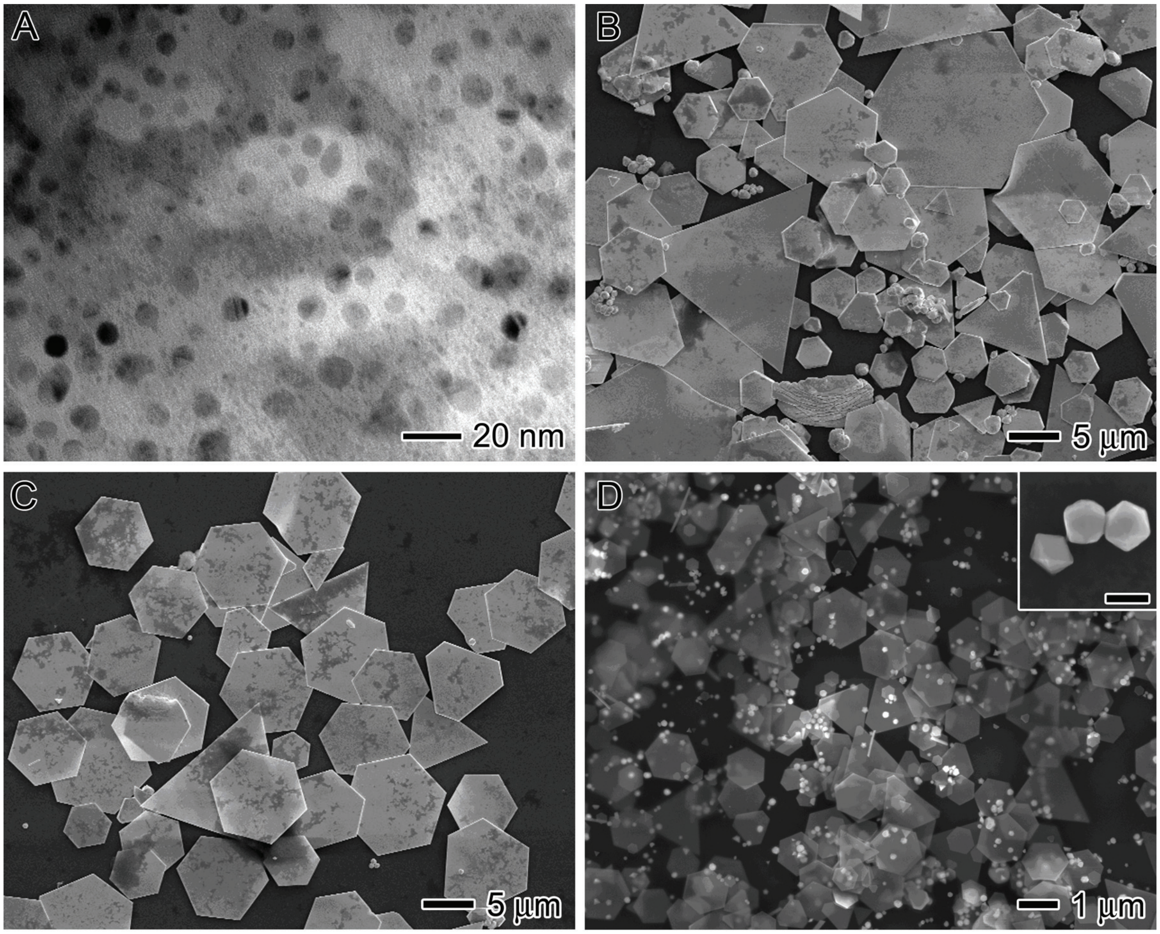

Figure 5.2 Influence of temperature on size and morphology. (A) TEM and (B-D) SEM images of the products synthesized using the standard procedure except at a temperature of 4, 37, 65, and 75 °C, respectively. The scale bar in the inset is 200 nm.

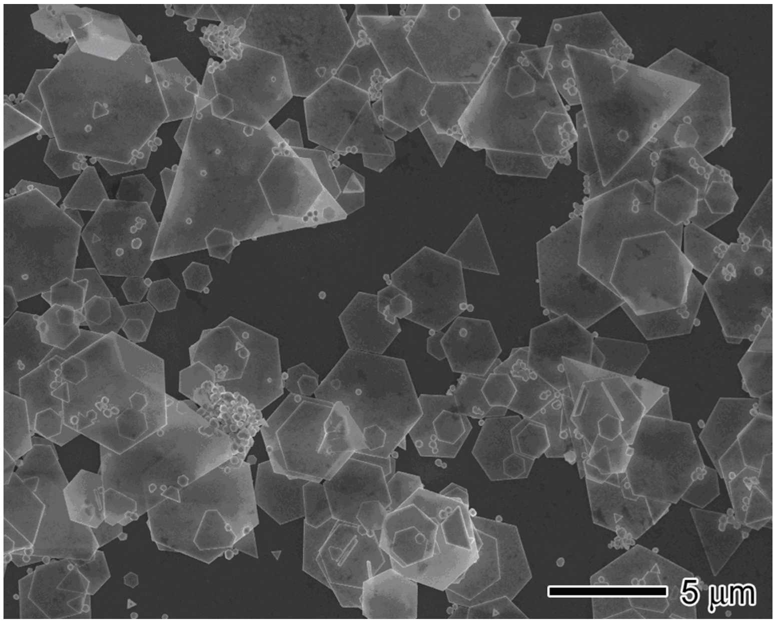

Figure 5.3 Influence of BSA structure on the size and morphology. A SEM image of the product obtained using the standard protocol, except that the BSA solution was heated beforehand for 30 minutes at 75 °C and then reduced to 55 °C.

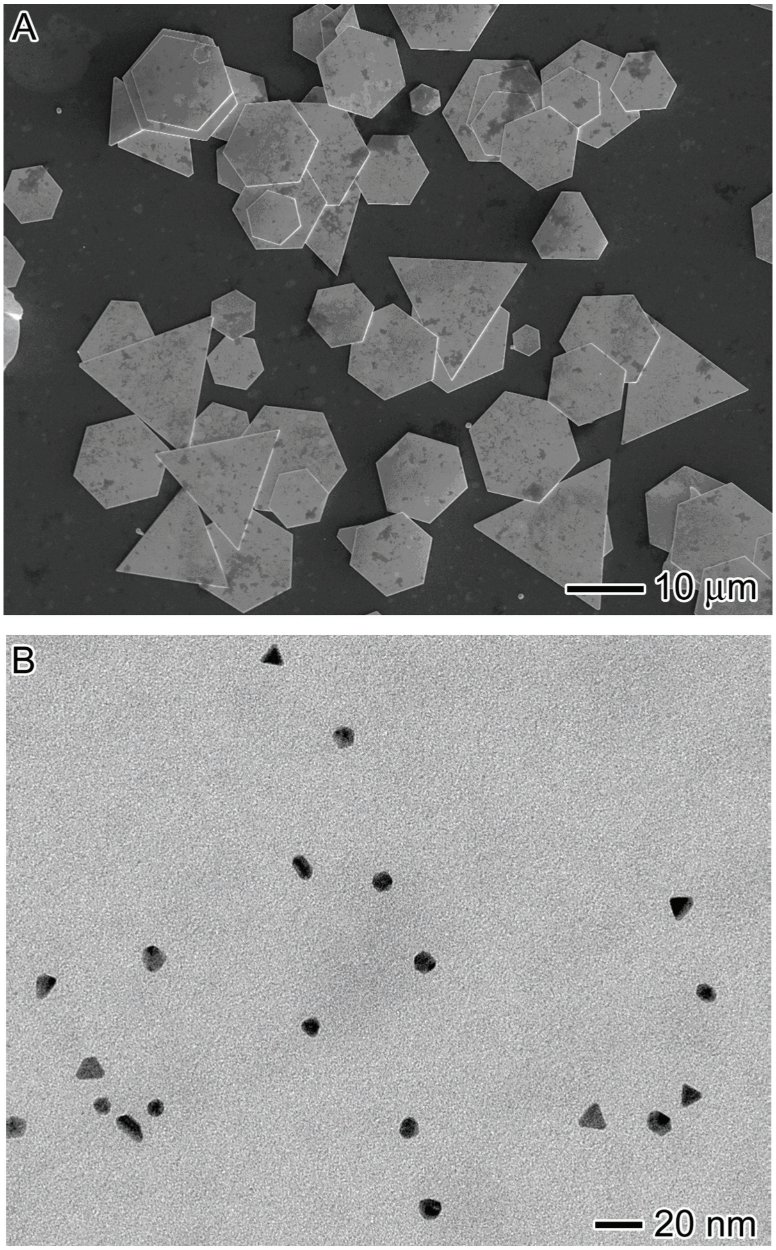

Figure 5.4 Influence of pH value on size and morphology. (A) SEM and (B) TEM images of the products synthesized using the standard procedure, except at starting pH values of 3.0 and 10.0, respectively.

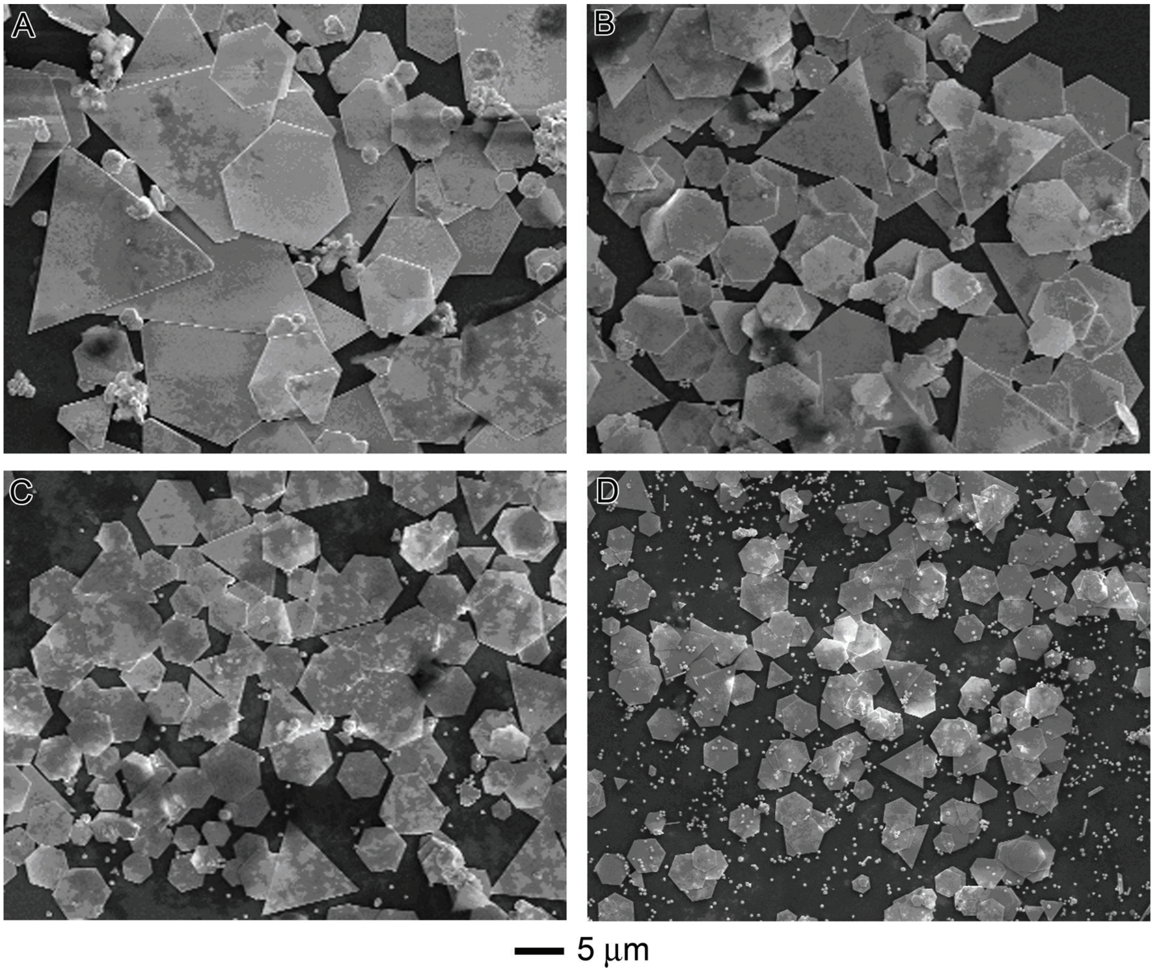

Figure 5.5 Influence of BSA concentration on size and morphology. SEM images of products synthesized using the standard procedure, except with different amounts of BSA: (A) 0.03, (B) 0.04, (C) 0.07, and (D) 0.09 g.

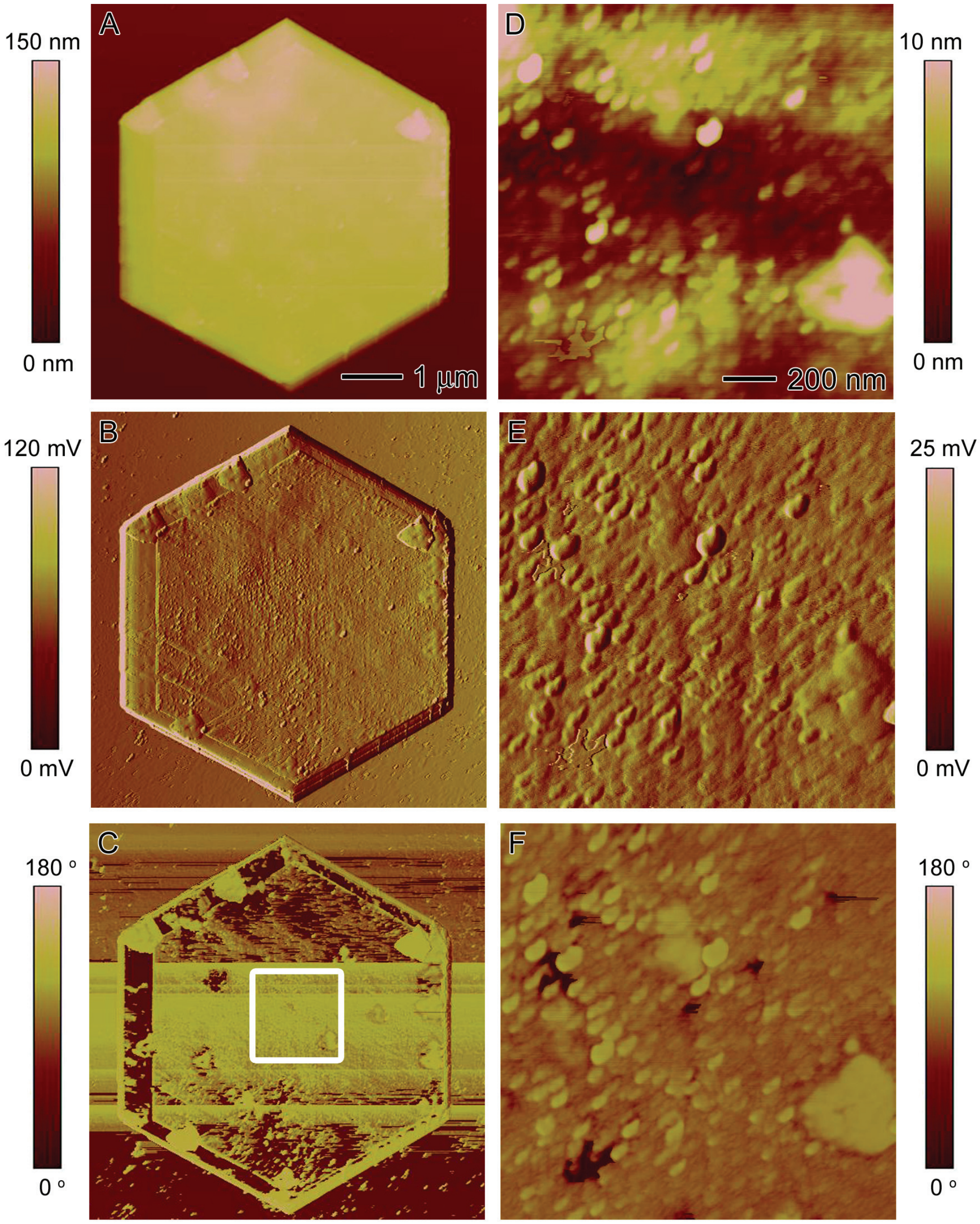

Figure 5.6 AFM characterization of the surface of a Au microplate. AFM height (A), amplitude (B), and phase contrast (C) images of a Au microplate synthesized using the standard procedure. (C-F) Height, amplitude, and phase contrast images, respectively, of the boxed region in (C).

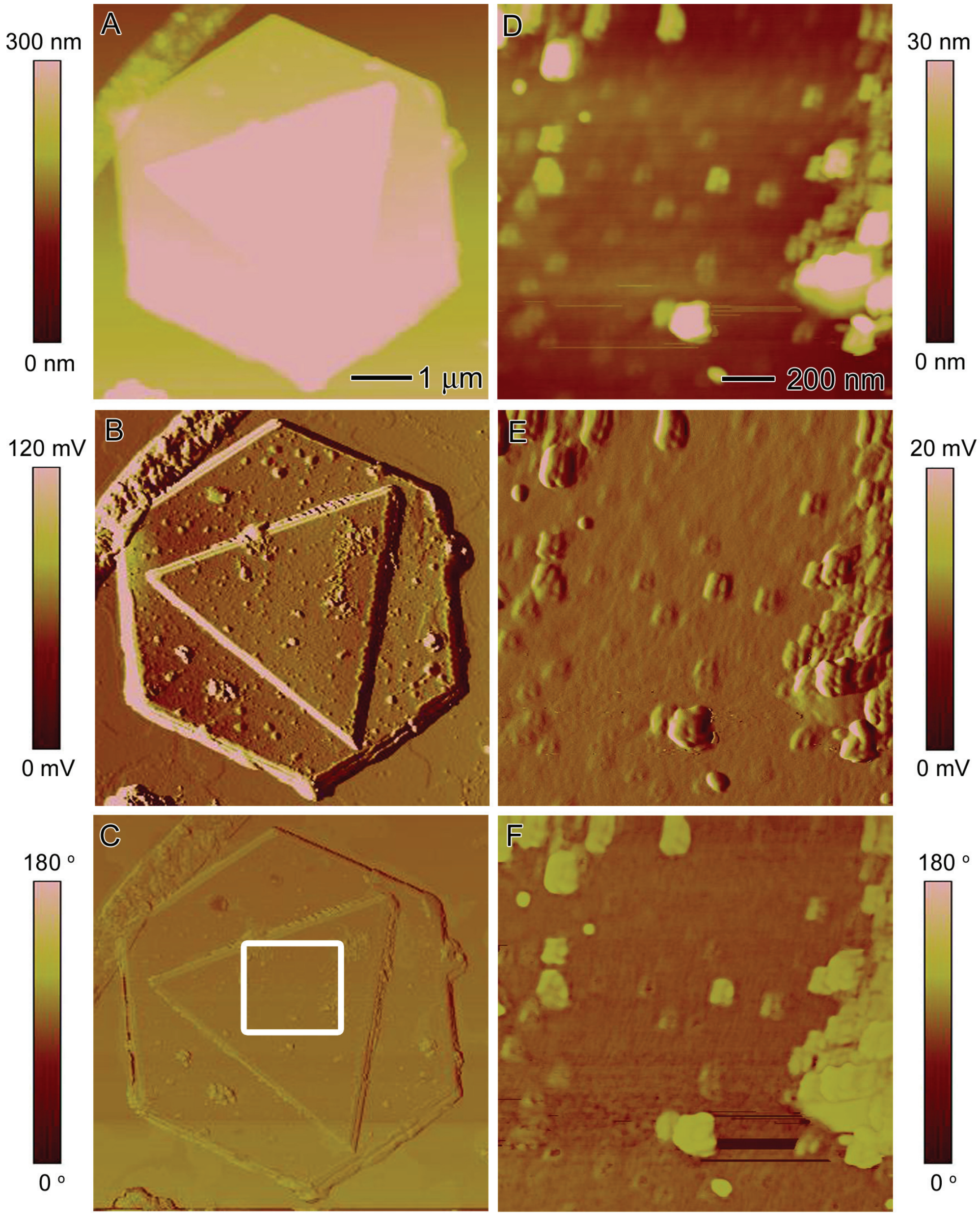

Figure 5.7 AFM height (A), amplitude (B), and phase contrast (C) images of Au microplates synthesized using the standard procedure after HNO_3 treatment in an attempt to remove BSA from the surface. (C-F) Height, amplitude, and phase contrast images, respectively, of the boxed region in (C). The aggregation of the bumps after treatment with HNO_3 indicated that it was BSA residing on the surface of the Au microplate.

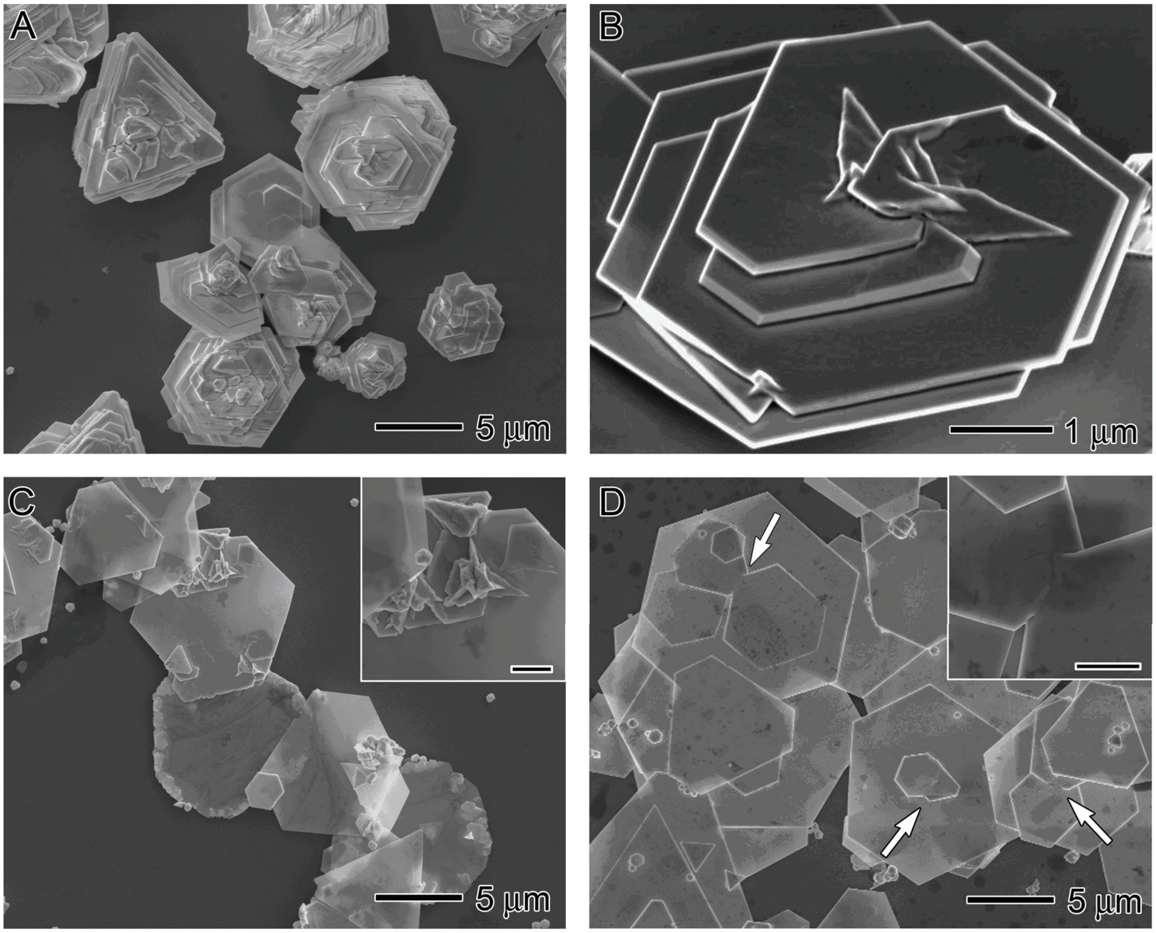

Figure 5.8 Influence of ions on size and morphology. SEM images of products synthesized using the standard procedure except replacing the TBS solution with 18 MΩ water at (A, B) 37, (C) 55, and (D) 75 °C. (B) A tilted SEM image of the same sample in (A) showing the screw dislocation. (D) The arrows point to the junction between two adjoining plates. The scale bars in the insets are 2 μm.

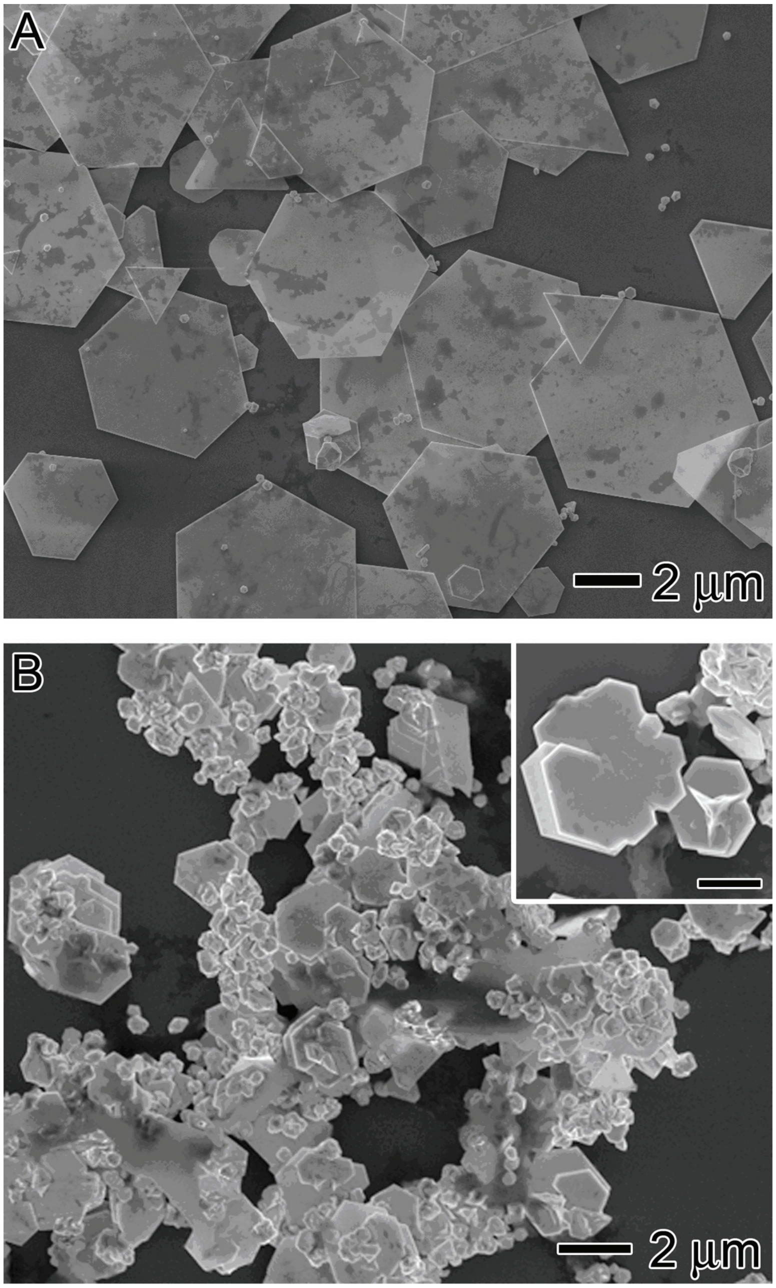

Figure 5.9 Influence of NaCl and tris on size and morphology. SEM image of the products synthesized using the standard procedure, except that the TBS was substituted with 18 MΩ water supplemented with (A) NaCl and (B) tris.

5.10 Notes to Chapter 5

[1] Millstone, J. E.; Park, S.; Shuford, K. L.; Qin, L.; Schatz, G. C.; Mirkin, C. A. *J. Am. Chem. Soc.* **2005**, *127*, 5312.

[2] Kan, C.; Zhu, X.; Wang, G. *J.Phys. Chem. B* **2006**, *110*, 4651.

[3] Xiong, Y.; McLellan, J. M.; Chen, J.; Yin, Y.; Li, Z.-Y.; Xia, Y. *J. Am. Chem. Soc.* **2005**, *127*, 17118.

[4] Xue, C.; Metraux, G. S.; Millstone, J. E.; Mirkin, C. A. *J. Am. Chem. Soc.* **2008**, *130*, 8337.

[5] Lim, B.; Camargo, P. H. C.; Xia, Y. *Langmuir* **2008**, *24*, 10437.

[6] Xia, Y.; Xiong, Y.; Lim, B.; Skrabalak, S. E. *Angew. Chem. Int. Edit.* **2009**, *48*, 60.

[7] Lofton, C.; Sigmund, W. *Adv. Funct. Mater.* **2005**, *15*, 1197.

[8] Jin, R.; Cao, Y.; Mirkin, C. A.; Kelly, K. L.; Schatz, G. C.; Zheng, J. G. *Science* **2001**, *294*, 1901.

[9] Sun, Y.; Mayers, B.; Xia, Y. *Nano Lett.* **2003**, *3*, 675.

[10] Shankar, S. S.; Rai, A.; Ankamwar, B.; Singh, A.; Ahmad, A.; Sastry, M. *Nat. Mater.* **2004**, *3*, 482.

[11] Liu, B.; Xie, J.; Lee, J. Y.; Ting, Y. P.; Chen, J. P. *J. Phys. Chem. B* **2005**, *109*, 15256.

[12] Xie, J.; Lee, Jim Y.; Wang, D. I. C.; Ting, Y. P. *Small* **2007**, *3*, 672.

[13] Xie, J.; Lee, J. Y.; Wang; Ting, Y. P. *J. Phys. Chem. C* **2007**, *111*, 16858.

[14] Carter, D. C.; Ho, J. X. In Advances in Protein Chemistry; Academic Press, 1994, p 153-203.

[15] Brown, J. R. *Fed. Proc.* **1975**, *34*, 591.

[16] Patterson, J. E.; Geller, D. M. *Biochem. Biophys. Res. Comm.* **1977**, *74*, 1220.

[17] McGillivray, R. T. A.; Chung, D. W.; Davie, E. W. *Eur. J. Biochem.* **1979**, *98*, 477.

[18] Hirayama, K.; Akashi, S.; Furuya, M.; Fukuhara, K. I. *Biochem. Biophys. Res. Comm.* **1990**, *173*, 639.

[19] Xiong, Y.; Washio, I.; Chen, J.; Cai, H.; Li, Z.-Y.; Xia, Y. *Langmuir* **2006**, *22*, 8563.

[20] Singh, A. V.; Bandgar, B. M.; Kasture, M.; Prasad, B. L. V.; Sastry, M. *J. Mater. Chem.* **2005**, *15*, 5115.

[21] Singh, A. V.; Patil, R.; Kasture, M. B.; Gade, W. N.; Prasad, B. L. V. *Colloid Surf. B* **2009**, *69*, 239.

[22] Bos, O. J. M.; Labro, J. F. A.; Fischer, M. J. E.; Witling, J.; Janssen, L. H. M. *J. Biol. Chem.* **1989**, *264*, 953.

[23] Carter, D. C.; He, X. M.; Munson, S. H.; Twigg, P. D.; Gernert, K. M.; Broom, M. B.; Miller, T. Y. *Science* **1989**, *244*, 1195.

[24] Murayama, K.; Tomida, M. *Biochem.* **2004**, *43*, 11526.

[25] Rüegg, U. T.; Rudinger, J.; Hirs, C. H. W.; Serge, N. T. In Methods in Enzymology; Academic Press, 1977, p 111-116.

[26] Smith, G. M. *J. Am. Chem. Soc.* **2002**, *44*, 1769.

[27] Shaw III, C. F. *Chem. Rev.* **1999**, *99*, 2589.

[28] Germain, V.; Li, J.; Ingert, D.; Wang, Z. L.; Pileni, M. P. *J. Phys.l Chem. B* **2003**, *107*, 8717.

[29] Clark, A. H.; Saunderson, D. H. P.; Suggett, A. *Int. J. Pept. Protein Res.* **1981**, *17*, 353.

[30] Lin, V. J. C.; Koenig, J. L. *Biopolymers* **1976**, *15*, 203.

[31] Wetzel, R.; Becker, M.; Behlke, J.; Billwitz, H.; Bohm, S.; Ebert, B.; Hamann, H.; Krumbiegel, J.; Lassmann, G. *Eur. J. Biochem.* **1980**, *104*, 469.

[32] Su, T. J.; Lu; Thomas, R. K.; Cui, Z. F.; Penfold, J. *J. Phys. Chem. B* **1998**, *102*, 8100.

[33] Sadler, P. J.; Tucker, A. *Eur. J. Biochem.* **1993**, *212*, 811.

[34] Khan, M. Y. *Biochem. J.* **1986**, *236*, 307.

[35] W.F. Harrington; Johnson, P.; Ottewill, R. H. *Biochem. J.* **1956**, *62*, 569.

[36] Suito, E.; Uyeda, N. *Bull. Inst. Chem. Res.* **1965**, *42*, 511.

[37] Katchalski, E.; Benjamin, G. S.; Gross, V. *J. Am. Chem. Soc.* **1957**, *79*, 4096.

[38] Li, X.; Li, Y.; Tan, Y.; Yang, C.; Li, Y. *J. Phys. Chem. B* **2004**, *108*, 5192.

[39] He, B.; Ha, Y.; Liu, H.; Wang, K.; Liew, K. Y. *J. Colloid Interf. Sci.* **2007**, *308*, 105.

[40] Zimmerman, R. J.; Kanal, K. M.; Sanders, J.; Cameron, I. L.; Fullerton, G. D. *J. Biochem. Biophys. Meth.* **1995**, *30*, 113.

[41] Burton, W. K.; Carbrera, N.; Frank, F. C. *Nature* **1949**, *163*, 398.

[42] Burton, W. K.; Cabrera, N.; Frank, F. C. *Phil. Trans. R. Soc. Lond. A* **1951**, *243*, 299.

[43] Krishnan, G.; Altekar, W. *Biochemistry* **2002**, *32*, 791.

[44] Lanyi, J. K. *Bacteriol. Rev.* **1974**, *38*, 272.

[45] Baxter, R. M.; Gibbons, N. E. *Can. J. Microbiol.* **1956**, *2*, 599.

[46] Holmes, P. K.; Halvarson, H. O. *J. Bacteriol.* **1965**, *90*, 312.

Chapter 6

Conclusion

For my dissertation, I developed some novel Au nanostructures and tailored their optical properties for biomedical applications. For Au nanocages, their size, wall thickness, and porosity determined the LSPR peak position as well as their scattering and absorption cross-sections. By tuning their LSPR peak to the near-infrared region and maximizing their absorption to scattering ratio, Au nanocages were used for imaging and photoablation of cancerous cells.

Gold nanocages with hollow interiors and porous walls were synthesized through the galvanic replacement reaction of Ag nanocubes and $AuCl_4^-$. By controlling the amount of $AuCl_4^-$ added to the reaction, the LSPR peak could be tuned from 400 nm to the near-infrared region. DDA calculations show that the Au nanocages have strong absorption cross-sections, about five orders of magnitude larger than organic dyes.

As an extension to the replacement reaction, I compared the galvanic replacement reactions between Ag nanocubes and two Au precursors with different oxidation numbers: $AuCl_2^-$ and $AuCl_4^-$. Both reactions resulted in hollow nanostructures, but the Au nanostructures produced were thicker for the reaction with $AuCl_2^-$ than $AuCl_4^-$. This effect was attributed to the stoichiometric change between the number of Ag atom(s) consumed per Au atom formed (1:1 *versus* 3:1). The thicker edges and thus more robust structures were able to survive the dealloying process to form Au nanoframes.

The galvanic replacement reaction of Ag nanocubes and $AuCl_2^-$ formed nanoframes, a novel shape with all faces open. I studied the relationship between LSPR properties and the variations in edge length, ridge thickness, and corner sharpness using single-nanoparticle spectroscopy and DDA calculations. These results confirmed that the LSPR peak red-shifted with increasing ratio between the outer edge length and the ridge thickness. Additionally, the scattering intensity of the peak increased as this ratio value increased. Lastly, I demonstrated that Au nanoframes are promising substrates for SERS.

After optimizing the synthesis and LSPR properties, I applied the Au nanocages to the imaging of cancer cells. I functionalized the surface of the Au nanocages with anti-EGFR antibodies to target the overexpressed EGFR on the surface of U87MGwtEGFR cancer cells. I evaluated the uptake of anti-EGFR Au nanocages by the cells using two-photon confocal microscopy under different conditions (i.e. temperature, time of incubation, number of antibodies on the nanocage, and size of nanocage). The results further enhance the understanding of how Au nanostructures interact with cells as well as provide insight on the optimal conditions for cellular uptake of the Au nanocages. In general, smaller nanocages ~35 nm, longer incubation time 24 h, and larger number of antibodies per nanocage resulted in an increased uptake of anti-EGFR nanocages. The qualitative PL results agreed well with the quantitative analysis of Au by ICP-MS. The two-photon PL from Au nanocages can be used to quickly screen for cancer cells, as well as evaluate their distribution in tissue for *ex vivo* and *in vivo* studies.

For the photothermal treatment of cancer cells, I quantified the photothermal effect of anti-EGFR Au nanocages on SK-BR-3 cells using flow cytometry. First, I determined that there were approximately 400 nanocages per cell using ICP-MS. Then I investigated the relationship between laser parameters and cellular damage. The cellular death increased linearly after a power threshold of 1.6 W/cm^2. Additionally, the cellular death increased as the time of exposure increased to 5 minutes, after the cellular death became steady. These result provide insights into how the photothermal response of Au nanocages can be optimized and controlled for the future *in vivo* treatment of cancer.

Lastly, I synthesized Au microplates using the hydroxyl groups in BSA as the reductant. Temperature, pH, and salt concentration all played important roles in unfolding the BSA molecule to expose the hydroxyl group. The optimal conditions for producing Au microplates were the following: 1) 55 ^{o}C when the BSA was irreversibly denatured, 2) acidic pH when the BSA was elongated, 3) in the TBS. BSA molecules were attached to the surface of the Au microplates likely through Au-thiolate bonds. These as-synthesized microplates can serve as substrates as confining cellular growth.

Bibliography

Abrams, M. J.; Murrer, B. A. *Science* **1993**, *261*, 725.

Aden, A. L.; Kerker, M. *J. Appl. Phys.* **1951**, *22*, 1242.

Aizpurua, J.; Garnett, W. B.; Lee, J. R.; Abajo, F. J. G. d.; Brian, K. K.; Mallouk, T. *Phys. Rev. B* **2005**, *71*, 235420.

Arndt-Jovin, D. J.; Jovin, T. M. *Methods Cell. Biol.* **1989**, *30*, 417.

Au, L.; Lu, X.; Xia, Y. *Adv. Mater.* **2008**, *20*, 2517.

Au, L.; Zheng, D.; Zhou, F.; Li, Z.-Y.; Li, X.; Xia, Y. *ACS Nano* **2008**, *2*, 1645.

Averitt, R. D.; Sarkar, D.; Halas, N. J. *Phys. Rev. Lett.* **1997**, *78*, 4217.

Averitt, R. D.; Westcott, S. L.; Halas, N. J. *J. Opt. Soc. Am. B* **1999**, *16*, 1824.

Bao, G.; Bao, X. R. *P. Natl. Acad. Sci. USA* **2005**, *102*, 9997.

Batzill, M.; Koel, B. E. *Surf. Sci.* **2004**, *553*, 50.

Baxter, R. M.; Gibbons, N. E. *Can. J. Microbiol.* **1956**, *2*, 599.

Beversluis, M. R.; Bouhelier, A.; Novotny, L. *Phys. Rev. B* **2003**, *68*, 115433.

Black, K. C.; Kirkpatrick, N. D.; Troutman, T. S.; Xu, L.; Vagner, J.; Gillies, R. J.; Barton, J.; Utzinger, U.; Romanowski, M. *Mol. Imaging* **2008**, *7*, 50.

Blatchford, C. G.; Campbell, J. R.; Creigton, J. A. *Surf. Sci.* **1992**, *120*, 435.

Bos, O. J. M.; Labro, J. F. A.; Fischer, M. J. E.; Witling, J.; Janssen, L. H. M. *J. Biol. Chem.* **1989**, *264*, 953.

Bouhelier, A.; Beversluis, M. R.; Novotny, L. *Appl. Phys. Lett.* **2003**, *83*, 5041.

Boyd, G. T.; Yu, Z. H.; Shen, Y. R. *Phys. Rev. B* **1986**, *33*, 7923.

Brown, J. R. *Fed. Proc.* **1975**, *34*, 591.

Burton, W. K.; Cabrera, N.; Frank, F. C. *Phil. Trans. R. Soc. Lond. A* **1951**, *243*, 299.

Burton, W. K.; Carbrera, N.; Frank, F. C. *Nature* **1949**, *163*, 398.

Campbell, C. T. *Science* **2004**, *306*, 234.

Cang, H.; Sun, T.; Li, Z.-Y.; Chen, J.; Wiley, B. J.; Xia, Y.; Li, X. *Opt. Lett.* **2005**, *30*, 3048.

Carter, D. C.; He, X. M.; Munson, S. H.; Twigg, P. D.; Gernert, K. M.; Broom, M. B.; Miller, T. Y. *Science* **1989**, *244*, 1195.

Carter, D. C.; Ho, J. X. In Advances in Protein Chemistry; Academic Press, 1994, p 153-203.

Chang, S.; Chao-Wen, S.; Chemg-Dah, C.; Wei-Cheng, L.; Wang, C. R. C. *Langmuir* **1999**, *15*, 701.

Charnay, C.; Lee, A.; Man, S. Q.; Moran, C. E.; Radloff, C.; Bradley, R. K.; Halas, N. J. *J. Phys. Chem. B* **2003**, *107*, 7327.

Chen, J.; McLellan, J. M.; Siekkinen, A.; Xiong, Y.; Li, Z.-Y.; Xia, Y. *J. Am. Chem. Soc.* **2006**, *128*, 14776.

Chen, J.; Saeki, F.; Wiley, B. J.; Cang, H.; Cobb, M. J.; Li, Z.-Y.; Au, L.; Zhang, H.; Kimmey, M. B.; Li, X.; Xia, Y. *Nano Lett.* **2005**, *5*, 473.

Chen, J.; Wang, D.; Xi, J.; Au, L.; Siekkinen, A.; Warsen, A.; Li, Z.-Y.; Zhang, H.; Xia, Y.; Li, X. *Nano Lett.* **2007**, *7*, 1318.

Chen, J.; Wiley, B.; Li, Z. Y.; Campbell, D.; Saeki, F.; Cang, H.; Au, L.; Lee, J.; Li, X.; Xia, Y. *Adv. Mater.* **2005**, *17*, 2255.

Chen, J.; Wiley, B. J.; McLellan, J.; Xiong, Y.; Li, Z.-Y.; Xia, Y. *Nano Lett.* **2005**, *5*, 2058.

Chen, J. Y.; Li, Z.-Y.; Au, L.; Hartland, G. V.; Li, X. D.; Marquez, M.; Xia, Y. *Chem. Soc. Rev.* **2006**, *35*, 1084.

Chen, Y.; Munechika, K.; Ginger, D. S. *Nano Lett.* **2007**, *7*, 690.

Chen, Y.; Munechika, K.; Ginger, D. S. *MRS Bull.* **2008**, *33*, 536.

Chen, Y.; Munechika, K.; Plante, I. J.-L.; Munro, A. M.; Skrabalak, S.; Xia, Y.; Ginger, D. S. *Appl. Phys. Lett.* **2008**, *93*, 053106.

Chithrani, B. D.; Chan, W. C. W. *Nano Lett.* **2007**, *7*, 1542.

Chithrani, B. D.; Ghazani, A. A.; Chan, W. C. W. *Nano Lett.* **2006**, *6*, 662.

Cho, E. C.; Xie, J.; Wurm, P. A.; Xia, Y. *Nano Lett.* **2009**, *9*, 1080.

Clark, A. H.; Saunderson, D. H. P.; Suggett, A. *Int. J. Pept. Protein Res.* **1981**, *17*, 353.

Cobley, C. M.; Campbell, D. J.; Xia, Y. *Adv. Mater.* **2008**, *20*, 748.

Delves, P. J.; Martin, S. J.; Burton, D. R.; Roitt, I. M. Roitt's Essential Immunology; Wiley-Blackwell: Malden, 2006.

Dick, K.; Dhanasekaran, T.; Zhang, Z.; Meisel, D. *J. Am. Chem. Soc.* **2002**, *124*, 2312.

Drachev, V. P.; Khaliullin, E. N.; Kim, W.; Alzoubi, F.; Rautian, S. G.; Safonov, V. P.; Armstrong, R. L.; Shalaev, V. M. *Phys. Rev. B* **2004**, *69*, 035318.

Draine, B. T.; Flatau, P. J. *J. Opt. Soc. Am. A* **1994**, *11*, 1491.

Eiblmaier, M.; Meyer, L. A.; Watson, M. A.; Fracasso, P. M.; Pike, L. J.; Anderson, C. J. *J. Nucl. Med.* **2008**, *49*, 1472.

Elghanian, R.; Storhoff, J. J.; Mucic, R. C.; Letsinger, R. L.; Mirkin, C. A. *Science* **1997**, *277*, 1078.

El-Sayed, M. A. *Acc. Chem. Res.* **2001**, *34*, 257.

Fan, H. J.; Knez, M.; Scholz, R.; Hesse, D.; Nielsch, K.; Zacharias, M.; Gosele, U. *Nano Lett.* **2007**, *7*, 993.

Faraday, M. *Philos. Trans. R. Soc. London* **1857**, *147*, 145.

Farrer, R. A.; Butterfield, F. L.; Chen, V. W.; Fourkas, J. T. *Nano Lett.* **2005**, *5*, 1139.

Fievet, F.; Lagier, J. P.; Figlarz, M. *MRS Bull.* **1989**, *14*, 29.

Foss, C. A.; Hornyak, G. L.; Stockert, J. A.; Martin, C. R. *J. Phys. Chem. B* **1994**, *98*, 2963.

Frankel, A. *Clin. Cancer Res.* **2002**, *8*, 1699.

Fuchs, R. *Phys. Rev. B* **1975**, *11*, 1732.

Gao, H.; Shi, W.; Freund, L. B. *P. Natl. Acad. Sci. USA* **2005**, *102*, 9469.

Germain, V.; Li, J.; Ingert, D.; Wang, Z. L.; Pileni, M. P. *J. Phys. Chem. B* **2003**, *107* 8717.

Grodzinski, P.; Silver, M.; Molnar, L. K. *Expert Rev. Mol. Diagn.* **2006**, *6*, 307.

Haes, A. J.; Haynes, C. L.; McFarland, A. D.; Schatz, G. C.; Van Duyne, R. P.; Zhou, S. *MRS Bull.* **2005**, *30*, 368.

Harrington, W.F.; Johnson, P.; Ottewill, R. H. *Biochem. J.* **1956**, *62*, 569.

He, B.; Ha, Y.; Liu, H.; Wang, K.; Liew, K. Y. *J. Colloid Interf. Sci.* **2007**, *308*, 105.

Hirayama, K.; Akashi, S.; Furuya, M.; Fukuhara, K. I. *Biochem. Biophys. Res. Comm.* **1990**, *173*, 639.

Hirsch, L. R.; Gobin, A. M.; Lowery, A. R.; Tam, F.; Drezek, R. A.; Halas, N. J.; West, J. L. *Ann. Biomed. Eng.* **2006**, *34*, 15.

Hirsch, L. R.; Stafford, R. J.; Bankson, J. A.; Sershen, S. R.; Rivera, B.; Price, R. E.; Hazle, J. D.; Halas, N. J.; West, J. L. *Proc. Natl. Acad. Sci. U.S.A.* **2003**, *23*, 13549.

Holmes, P. K.; Halvarson, H. O. *J. Bacteriol.* **1965**, *90*, 312.

http://ase.tufts.edu/biomedical/research/Fantini/researchAreas/NearInfraredSpectroscopy.pdf.

http://geology.com/minerals/gold/uses-of-gold.shtml.

http://www.cdc.gov/nchs/fastats/lcod.htm.

http://www.pubmed.gov. Protein Search: CAA76847, P. D. B., National Center for Biotechnology Information, Bethesda, MD 20894. .

Hu, M.; Chen, J.; Li, Z. Y.; Au, L.; Hartland, G. V.; Li, X.; Marquez, M.; Xia, Y. *Chem. Soc. Rev.* **2006**, *35*, 1084.

Huang, X.; El-Sayed, I. H.; Qian, W.; El-Sayed, M. A. *J. Am. Chem. Soc.* **2006**, *128*, 2115.

Hurwitz, E.; Stancovski, I.; Sela, M.; Yarden, Y. *Proc. Natl. Acad. Sci. U.S.A.* **1995**, *92*, 3353.

Imura, K.; Nagahara, T.; Okamoto, H. *J. Am. Chem. Soc.* **2004**, *126*, 12730.

Jain, P. K.; Huang, X.; El-Sayed, I. H.; El-Sayed, M. A. *Acc. Chem. Res.* **2008**, *41*, 1578.

Jiang, W.; KimBetty, Y. S.; Rutka, J. T.; Chan, W. C. W. *Nat. Nano.* **2008**, *3*, 145.

Jin, R.; Cao, Y.; Mirkin, C. A.; Kelly, K. L.; Schatz, G. C.; Zheng, J. G. *Science* **2001**, *294,* 1901.

Kan, C.; Zhu, X.; Wang, G. *J.Phys. Chem. B* **2006**, *110*, 4651.

Katchalski, E.; Benjamin, G. S.; Gross, V. *J. Am. Chem. Soc.* **1957**, *79*, 4096.

Kelly, K. L.; Coronado, E.; Zhao, L. L.; Schatz, G. C. *J. Phys. Chem. B* **2003**, *107*, 668.

Khan, M. Y. *Biochem. J.* **1986**, *236*, 307.

Kim, D.; Park, J.; An, K.; Yang, N.-K.; Park, J.-G.; T., H. *J. Am. Chem. Soc.* **2007**, *129*, 5812.

Kim, S. W.; Kim, M.; Lee, W. Y.; Hyeon, T. *J. Am. Chem. Soc.* **2002**, *124*, 7642.

Kottmann, J. P.; Martin, O. J. F.; Smith, D. R.; Schultz, S. *Phys. Rev. B* **2001**, *64*, 235402.

Kreibig, U.; Vollmer, M. Optical Properties of Metal Clusters; Springer: New York, 1995.

Kreibig, U. G., L. *Surf. Sci.* **1987**, *156*, 678.

Krishnan, G.; Altekar, W. *Biochemistry* **2002**, *32*, 791.

Lanyi, J. K. *Bacteriol. Rev.* **1974**, *38*, 272.

Li, X.; Li, Y.; Tan, Y.; Yang, C.; Li, Y. *J. Phys. Chem. B* **2004**, *108*, 5192.

Liao, H. W. N., C.L.; Hafner, J.H. *Nanomed.* **2006**, *1*, 201.

Lim, B.; Camargo, P. H. C.; Xia, Y. *Langmuir* **2008**, *24*, 10437.

Lin, V. J. C.; Koenig, J. L. *Biopolymers* **1976**, *15*, 203.

Link, S.; El-Sayed, M. A. *J. Phys. Chem. B* **1999**, *103*, 8410.

Liu, B.; Xie, J.; Lee, J. Y.; Ting, Y. P.; Chen, J. P. *J. Phys. Chem. B* **2005**, *109*, 15256.

Liu, J. L., Y. *J. Am. Chem. Soc.* **2003**, *125*, 6642.

LizMarsan, L. M.; Giersig, M.; Mulvaney, P. *Langmuir* **1996**, *12*, 4329.

Lofton, C.; Sigmund, W. *Adv. Funct. Mater.* **2005**, *15*, 1197.

Loo, C.; Lin, A.; Hirsch, L.; Lee, M. H.; Barton, J.; Halas, N.; West, J.; Drezek, R. *Technol. Cancer Res. Treat.* **2004**, *3*, 33.

Loo, C.; Lowery, A.; Halas, N.; West, J.; Drezek, R. *Nano Lett.* **2005**, *5*, 709.

Love, J. C.; Estroff, L. A.; Kriebel, J. K.; Nuzzo, R. G.; Whitesides, G. M. *Chem. Rev.* **2005**, *105*, 1103.

Lu, X.; Au, L.; McLellan, J.; Li, Z.-Y.; Marquez, M.; Xia, Y. *Nano Lett.* **2007**, *7*, 1764.

Lu, X.; Chen, J.; Skrabalak, S. E.; Xia, Y. *Proc. IMechE Part N: J. Nanoengineering and Nanosystems* **2007**, *221*.

McGillivray, R. T. A.; Chung, D. W.; Davie, E. W. *Eur. J. Biochem.* **1979**, *98*, 477.

McLellan, J. M.; Li, Z.-Y.; Siekkinen, A. R.; Xia, Y. *Nano Lett.* **2007**, *7*, 1013.

McLellan, J. M.; Siekkinen, A.; Chen, J.; Xia, Y. *Chem. Phys. Lett.* **2006**, *247*, 122.

Mie, G. *Ann. Phys.* **1908**, *25*, 377.

Millstone, J. E.; Park, S.; Shuford, K. L.; Qin, L.; Schatz, G. C.; Mirkin, C. A. *J. Am. Chem. Soc.* **2005**, *127*, 5312.

Mohamed, M. B.; Volkov, V.; Link, S.; El-Sayed, M. A. *Chem. Phys. Lett.* **2000**, *317*, 517.

Mooradian, A. *Phys. Rev. Lett.* **1969**, *22*, 185.

Munechika, K.; Smith, J. M.; Chen, Y.; Ginger, D. S. *J. Phys. Chem. C* **2007**, *111*, 18906.

Murayama, K.; Tomida, M. *Biochem.* **2004**, *43*, 11526.

Murphy, C. J.; Jana, N. R. *Adv. Mater.* **2002**, *14*, 80.

Murphy, C. J.; Sau, T. K.; Gole, A. M.; Orendorff, C. J.; Gao, J.; Gou, L.; Hunyadi, S. E.; Li, T. *J. Phys. Chem. B* **2005**, *109*, 13857.

Nagahara, L. A.; Ferrari, M.; Grodzinshi, P. *MRS Bull.* **2009**, *34*, 406.

Nagesha, D.; Laevsky, G. S.; Lampton, P.; Banyal, R.; Warner, C.; DiMarzio, C.; Sridhar, S. *Int. J. Nanomedicine* **2007**, *2*, 813.

Nagy, P.; Jenei, A.; Kirsch, A. K.; Szollosi, J.; Damjanovich, S. *J. Cell Sci.* **1999**, *112*, 1733.

Neeves, A. E.; Birnboim, M. H. *J. Opt. Soc. Am. B* **1989**, *6*, 787.

Noguez, C. *J. Phys. Chem. C* **2007**, *111*, 3806.

Novak, J. P.; Feldheim, D. L. *J. Am. Chem. Soc.* **2000**, *122*, 3979.

O' Neal, D. P.; Hirsch, L. R.; Halas, N. J.; Payne, J. D.; West, J. L. *Cancer Lett.* **2004**, *209*, 171.

Oberg, K. A.; Uversky, V. N. *Protein Peptide Lett* **2001**, *8*, 297.

Odom, T. W.; Pileni, M.-P. *Acc. Chem. Res.* **2008**, *41*, 1565.

Oldenberg, S. J.; Averitt, R. D.; Westcott, S. L.; Halas, N. J. *Chem. Phys. Lett.* **1998**, *28*, 243.

Oldenburg, S. J.; Jackson, J. B.; Westcott, S. L.; Halas, N. J. *Appl. Phys. Lett.* **1999**, *75*, 2897.

Osaki, F.; Kanamori, T.; Sando, S.; Sera, T.; Aoyama, Y. *J. Am. Chem. Soc.* **2004**, *126*, 6520.

Pastan, I.; Willingham, M. C. Endocytosis; Plenum Press: New York, 1985.

Patterson, J. E.; Geller, D. M. *Biochem. Biophys. Res. Comm.* **1977**, *74*, 1220.

Peyser, L. A.; Lee, T.-H.; Dickson, R. M. *J. Phys. Chem. B* **2002**, *106*, 7725.

Pissuwan, D.; Valenzuela, S. M.; Cortie, M. B. *Trends Biotechnol.* **2006**, *24*, 62.

Poole, S.; West, S. I.; Fry, J. C. *Food Hydrocolloids* **1987**, *1*, 301.

Portney, N. G.; Ozkan, M. *Anal. Bioanal. Chem.* **2006**, *384*, 620.

Qian, L.; Yang, X. *Colloids Surf. A* **2005**, *260*, 79.

Quinten, M.; Kreibig, U. *Surf. Sci.* **1986**, *172*, 557.

Reed, R. G.; Putnam, F. W.; Peters, T. J. *Biochem. J.* **1980**, *191*, 867.

Reynolds, E. S. *J. Cell Biol.* **1963**, *16*, 208.

Roosen, A. R.; Carter, W. C. *Physica A* **1998**, *261*, 232.

Ruegg, M.; Moor, U.; Blanc, B. *J. Dairy Res.* **1977**, *44*, 509.

Rüegg, U. T.; Rudinger, J.; Hirs, C. H. W.; Serge, N. T. In Methods in Enzymology; Academic Press, 1977, p 111-116.

Ruoslahti, E. *Scand. J. Immunol.* **1976**, *5*, 3.

Sadler, P. J.; Tucker, A. *Eur. J. Biochem.* **1993**, *212*, 811.

Sarkar, D.; Halas, N. J. *Phys. Rev. E* **1997**, *56*, 1102.

Seo, D.; Yoo, C. I.; Park, J. C.; Park, S. M.; Ryu, S.; Song, H. *Angew. Chem. Int. Ed.* **2008**, *47*, 763.

Shankar, S. S.; Rai, A.; Ankamwar, B.; Singh, A.; Ahmad, A.; Sastry, M. *Nat. Mater.* **2004**, *3*, 482.

Shaw III, C. F. *Chem. Rev.* **1999**, *99*, 2589.

Sherry, L. J.; Chang, S. H.; Schatz, G. C.; Van Duyne, R. P.; Wiley, B. J.; Xia, Y. *Nano Lett.* **2005**, *5*, 2034.

Shi, H.; Zhang, L.; Cai, W. *J. Appl. Phys.* **2000**, *87*, 1572.

Siekkinen, A. R.; McLellan, J. M.; Chen, J.; Xia, Y. *Chem. Phys. Lett.* **2006**, *432*, 491.

Sieradzki, K. *J. Electrochem. Soc.* **1993**, *140*, 2868.

Singh, A. V.; Bandgar, B. M.; Kasture, M.; Prasad, B. L. V.; Sastry, M. *J. Mater. Chem.* **2005**, *15*, 5115.

Singh, A. V.; Patil, R.; Kasture, M. B.; Gade, W. N.; Prasad, B. L. V. *Colloid Surface B* **2009**, *69*, 239.

Skrabalak, S.; Chen, J.; Au, L.; Lu, X.; Li, X.; Xia, Y. *Adv. Mater.* **2007**, *19*, 3177.

Skrabalak, S. E.; Au, L.; Li, X.; Xia, Y. *Nat. Protoc.* **2007**, *2*, 2182.

Skrabalak, S. E.; Chen, J.; Sun, Y.; Lu, X.; Au, L.; Cobley, C. M.; Xia, Y. *Acc. Chem. Res.* **2008**, *41*, 1587.

Skrabalak, S. E.; Wiley, B. J.; Kim, M.; Formo, E. V.; Xia, Y. *Nano Letters* **2008**, *8*, 2077.

Smith, G. M. *J. Am. Chem. Soc.* **2002**, *44*, 1796.

Sokolov, K.; Follen, M.; Aaron, J.; Pavlova, I.; Malpica, A.; Lotan, R.; Richards-Kortum, R. *Cancer Res.* **2003**, *63*, 1999.

Song, K. H.; Kim, C.; Cobley, C. M.; Xia, Y.; Wang, L. V. *Nano Lett.* **2009**, *9*, 183.

Su, T. J.; Lu; Thomas, R. K.; Cui, Z. F.; Penfold, J. *J. Phys. Chem. B* **1998**, *102*, 8100.

Suito, E.; Uyeda, N. *Bull. Inst. Chem. Res.* **1965**, *42*, 511.

Sun, Y.; Mayer, B.; Xia, Y. *Nano Lett.* **2002**, *2*, 481.

Sun, Y.; Mayers, B.; Herricks, T.; Xia, Y. *Nano Lett.* **2003**, *3*, 955.

Sun, Y.; Mayers, B.; Xia, Y. *Adv. Mater.* **2003**, *15*, 641.

Sun, Y.; Mayers, B.; Xia, Y. *Nano Lett.* **2003**, *3*, 675.

Sun, Y.; Xia, Y. *Anal. Chem.* **2002**, *74*, 5297.

Sun, Y.; Xia, Y. *Science* **2002**, *298*, 2176.

Sun, Y.; Xia, Y. *Nano Lett.* **2003**, *3*, 1569.

Sun, Y.; Xia, Y. *J. Am. Chem. Soc.* **2004**, *126*, 3892.

Talley, C. E.; Jackson, J. B.; Oubre, C.; Grady, N. K.; Hollars, C. W.; Lane, S. M.; Huser, T. R.; Nordlander, P.; Halas, N. J. *Nano Lett.* **2005**, *5*, 1569.

Tao, A.; Sinsermsuksakul, P.; Yang, P. *Angew. Chem. Int. Ed.* **2006**, *45*, 4597.

Templeton, A. C.; Wuefling, W. P.; Murray, R. W. *Acc. Chem. Res.* **2000**, *33*, 27.

Teperik, T. V.; Popov, V. V.; Abajo, F. J. G. d. *Phys. Rev. B* **2004**, *69*, 155402.

Van der Zande, B.; Bhmer, M. R.; Fokkink, L. G. J.; Schonenberger, C. *J. Phys. Chem. B* **1997**, *101*, 852.

Ventra, M. D.; Evoy, S.; Heflin, J. R. Introduction to Nanoscale Science and Technology; Kluwer Academic Publishers: Boston, 2004.

Wang, H.; Huff, T. B.; Zweifel, D. A.; He, W.; Low, P. S.; Wei, A.; Cheng, J.-X. *P. Natl. Acad. Sci. USA* **2005**, *102*, 15752.

Wang, Z. L. *J. Phys. Chem. B* **2000**, *104*, 1153.

West, J. L.; Halas, N. J. *Annu. Rev. Biomed. Eng.* **2003**, *5*, 285.

Wetzel, R.; Becker, M.; Behlke, J.; Billwitz, H.; Bohm, S.; Ebert, B.; Hamann, H.; Krumbiegel, J.; Lassmann, G. *Eur. J. Biochem.* **1980**, *104*, 469.

Wilcoxon, J. P.; Martin, J. E.; Parsapour, F.; Wiedenman, B.; Kelley, D. F. *J. Chem. Phys.* **1998**, *108*, 9137.

Wiley, B.; Herricks, T.; Sun, Y.; Xia, Y. *Nano Lett.* **2004**, *4*, 1733.

Wiley, B.; Sun, Y.; Xia, Y. *Acc. Chem. Res.* **2007**, *40*, 1067.

Wiley, B. J.; Chen, Y.; McLellan, J. M.; Xiong, Y.; Li, Z.-Y.; Ginger, D. S.; Xia, Y. *Nano Lett.* **2007**, *7*, 1032.

Wiley, B. J.; Im, S. H.; Li, Z.-Y.; McLellan, J. M.; Siekkinen, A.; Xia, Y. *J. Phys. Chem. B* **2006**, *110*, 15666.

Wiley, B. J.; Sun, Y.; Chen, J.; Cang, H.; Li, Z.-Y.; Li, X.; Xia, Y. *MRS Bull.* **2005**, *30*, 356.

Wiley, B. J.; Sun, Y.; Mayers, B.; Xia, Y. *Chem. Eur. J.* **2005**, *11*, 454.

Xia, Y.; Halas, N. J. *MRS Bull.* **2005**, *30*, 338.

Xia, Y.; Xiong, Y.; Lim, B.; Skrabalak, S. E. *Angew. Chem. Int. Edit.* **2009**, *48*, 60.

Xia, Y.; Yang, P.; Sun, Y.; Wu, Y.; Mayers, B.; Gates, B.; Yin, Y.; Kim, F.; Yan, H. *Adv. Mater.* **2003**, *15*, 353.

Xie, J.; Lee, J. Y.; Wang; Ting, Y. P. *J. Phys. Chem. C* **2007**, *111*, 16858.

Xie, J.; Lee, Jim Y.; Wang, D. I. C.; Ting, Y. P. *Small* **2007**, *3*, 672.

Xiong, Y.; McLellan, J. M.; Chen, J.; Yin, Y.; Li, Z.-Y.; Xia, Y. *J. Am. Chem. Soc.* **2005**, *127*, 17118.

Xiong, Y.; Washio, I.; Chen, J.; Cai, H.; Li, Z.-Y.; Xia, Y. *Langmuir* **2006**, *22*, 8563.

Xiong, Y.; Wiley, B. J.; Chen, J.; Li, Z.-Y.; Yin, Y.; Xia, Y. *Angew. Chem. Int. Ed.* **2005**, *44*, 7913.

Xue, C.; Metraux, G. S.; Millstone, J. E.; Mirkin, C. A. *J. Am. Chem. Soc.* **2008**, *130*, 8337.

Yang, J.; Lee, J. Y.; Too, H. P. *J. Phys. Chem. B* **2005**, *109*, 19208.

Yang, X.; Skrabalak, S. E.; Li, Z.-Y.; Xia, Y.; Wang, L. V. *Nano Lett.* **2007**, *7*, 3798.

Yelin, D.; Oron, D.; Thiberge, S.; Moses, E.; Silberberg, Y. *Opt. Express* **2003**, *11*, 1385.

Yin, Y.; Erdonmez, C.; Aloni, S.; Alivisatos, A. P. *J. Am. Chem. Soc.* **2006**, *128*, 12671.

Yin, Y.; Erdonmez, C.; Cabot, A.; Hughes, S.; Alivisatos, A. P. *Adv. Funct. Mater.* **2006**, *16*, 1389.

Yin, Y.; Rioux, R.; Erdonmez, C.; Hughes, S.; Somorjai, G.; Alivisatos, A. P. *Science* **2004**, *304*, 711.

Yu, Y. Y.; Chang, S. S.; Lee, C. L.; Wang, C. R. C. *J. Phys. Chem. B* **1997**, *101*, 6661.

Zhang, M.; Desai, T.; Ferrari, M. *Biomater.* **1998**, *19*, 953.

Zhang, S.; Li, J.; Lykotrafitis, G.; Bao, G.; Suresh, S. *Adv. Mater.* **2009**, *21*, 419.

Zimmerman, R. J.; Kanal, K. M.; Sanders, J.; Cameron, I. L.; Fullerton, G. D. *J. Biochem. Biophys. Meth.* **1995**, *30*, 113.